ORGANIZATION OF COLLOIDS AND POLYMERS WITH NONIONIC SURFACTANT ASSEMBLIES

Thesis Submitted to AcSIR For the Award of
the Degree of
DOCTOR OF PHILOSOPHY
in Physical Sciences

By
Edakkal Venugopal
Reg. No. 10PP11J26132

Under the Guidance of
Dr. Suresh K. Bhat

CSIR–National Chemical Laboratory, Pune

2015

CERTIFICATE

This is to certify that the work incorporated in this Ph.D. thesis entitled **'ORGANIZATION OF COLLOIDS AND POLYMERS WITH NONIONIC SURFACTANT ASSEMBLIES'** submitted by **Mr. Edakkal Venugopal** to Academy of Scientific and Innovative Research (AcSIR) in fulfillment of the requirements for the award of the Degree of **Doctor of Philosophy** in Physical Sciences, embodies original research work under my supervision/guidance. I further certify that this work has not been submitted to any other University or Institution in part or full for the award of any degree or diploma. Research material obtained from other sources has been duly acknowledged in the thesis. Any text, illustration, table etc., used in the thesis from other sources, have been duly cited and acknowledged.

Edakkal Venugopal
Reg. No. 10PP11J26132

Dr. Suresh K. Bhat
(Research Guide)

Acknowledgements

It is a pleasure to thank those who made this thesis possible. The thesis is incomplete without acknowledging the effort and help they have provided me. To begin with, I would like to extend my gratitude to my supervisor **Dr. Suresh K. Bhat** for guiding and supporting me throughout my research. It was with his help, I survived the distress situations during my tenure. I learned how to handle difficult situations in life from him. It is really motivating to see the way he communicates with instruments.

I express my deepest appreciation to **Dr. Guruswamy Kumaraswamy**who has been my mentor for a major part of this thesis and he provided a strong platform that helped me to improve and finish this work. His classes, courses, and weekly meetings were a great help for me to learn the in-depth details about the research and analysis. His presence in the weekly group meetings helped me to develop a strong presentation skill. **Dr. Guruswamy** has inspired me throughout the course with the method of his teaching as well as choosing a research problem inspired me throughout the course. His support and absolute criticism made an immense effect in my Ph.D. work.

Next, I would like to thank my Doctoral Advisory Committee members **Dr. P. R. Rajamohanan** (NCL, Pune), **Dr. Sarika Bhattacharya** (NCL, Pune) for their critical comments and suggestions. I am very grateful to **Prof. Raffaele Mezzenga** (ETH, Zürich) for the work on monoglycerides and the SAXS analysis of the liquid crystals. I also thank **Dr. Neetu Singh** (IIT Delhi), for the collaboration on cell studies, **Prof. Jayesh Bellare** (IIT Bombay), **Prof. Ishi Talmon** (Israel Institute of Technology) for Cryo-TEM experiments. I would like to appreciate the efforts taken by **Dr. Vinod K. Aswal** and **Dr. Debasis Sen** (both from BARC, Trombay) in carrying out neutron scattering experiments. I am very grateful towards **Dr. Asish Lele** (NCL Pune) for his

support and help during my thesis work. And I would also like thank **Mr. Stephan Hanschin** (ETH Zürich) for help in microscopy experiments, **Dr. Idit Amar Yuli** (ETH Zürich) and **Dr. Nissim Garti** (Hebrew University of Jerusalem) for suggestions in data analysis. I also thank **Dr. Sharvil Patil** (Poona College of Pharmacy) with whom I have collaborated and he helped me in my work with many valuable suggestions.

I am indebted to many of my friends and seniors for their constant motivation and support especially, **Dr. Kamendra P. Sharma** who helped to design the thesis plan and **Dr. Samruddhi Kamble** for doing the reactions and experiments in wet lab. I thank my colleagues Girish, Jijo, Alam Muhammed, Reneta Nergini, Venkat, Tina George, Luhluh, Jishnuprasad, Sabarish, Kiran, Fayis, Anju, Leena George, Manoj Sharma, Pooja Kayasth, Soumyajyoti Chatterjee, Sudhakar, Prashant Patil, Dhanalakshmi, Amruta Kulkarni, Sharadwatapan and all my labmates for the cooperation and help I have received. I also thank Dr. Chirag Kalelkar (IIT Kharagpur) for his help in learning MATLAB coding and LaTeX. A special thanks to my hostel friends Eldho, Alson, Suresh, Rajesh, Sumantra Bhattacharya, Indravadhan, Aneesh and Shoy for their encouragement. I sincerely acknowledge the financial aid from CSIR (New Delhi), NCL (Pune), and Swiss embassy in India. I also thank the former and present directors Dr. S. Sivaram, Dr. Sourav Pal and Dr. Vijayamohanan.

I owe my deepest gratitude to my mother and late grand mother from the bottom of my heart whose love, blessings, patience and understanding gave me the courage to pursue Ph.D. Also I express thanks to my wife Gayathry for her support and love and all my family members for their support and love.

Edakkal Venugopal

Dedicated to amma and ammamma(late)...

This page is intentionally left blank.

Abstract

Nonionic surfactants form liquid crystalline mesophases when mixed with polar solvents such as water. These mesophases are stabilized by a balance of competing interactions present in the system. Guest components modify these interactions and, therefore, influence the phase behavior of the system. Further, incorporation within surfactant assemblies also modifies the phase behavior of guest components. By tuning these interactions, different liquid crystalline phases can be accessed, that exhibit different surfactant organization and, therefore different rheological and transport properties. This ability to tune properties is valuable for various applications including drug delivery. Specifically, liquid crystalline phases formed by nonionic monoglycerides are found to be biocompatible and have potential for use in drug delivery systems. Sub micron-sized particles with internal liquid crystalline cubic struture formed by the monoglycerides allow simultaneous loading of hydrophobic and hydrophilic molecules. We demonstrate that monoglyceride particles can be coated with polyelectrolytes using electrostatic assembly in order to use them for charge specific targeting. Surfactant also associate with polyelectrolytes in solution and, modify their behaviour. The interactions of the polyelectrolytes with the surfactant assemblies are also studied. Four major aspects of the interactions of nonionic surfactants with colloids and polymers are studied in this thesis.

In the first part, we have investigated the microstructure and phase behavior of monoglyceride-based lyotropic liquid crystals in the presence of hydrophilic silica colloidal particles of size comparable to or slightly exceeding the repeat units of the different liquid crystalline phases. Using small angle X-ray scattering (SAXS) and differential scanning calorimetry (DSC), we compare the structural properties of the neat mesophases with those of the systems containing silica colloidal particles. It is found that the colloidal particles always macrophase separate in inverse bicontinuous cubic phases of gyroid ($Ia3d$)

and double diamond ($Pn3m$) symmetries. SAXS data for the inverse columnar hexagonal phase (H_{II}) and lamellar phase (L_α) suggest that a low volume fraction of the nanoparticles can be accommodated within the mesophases, but that at concentrations above a given threshold, the particles macrophase separate in these systems. The behavior is interpreted in terms of the enthalpic and entropic interactions of the nanoparticles with the lamellar and hexagonal phases, and we propose that, in the low concentration limit, nanoparticles act as point defects within the mesophases and, upon further increase in concentration, initiate nucleation of nanoparticles clusters, leading to macroscopic phase separation.

The cubic phases of monoolein is dispersed into submicron particles with internal cubic phase symmetry by means of high energy homogenization. These particles called "cubosomes" are stabilized using a triblock copolymer Pluronic F127. We demonstrate surface modification of cubosomes through adsorption of a single layer of cationic poly-ϵ-lysine. These cubosomes are simultaneously loaded with model hydrophobic and hydrophilic compounds (Naproxen sodium and Nile red, respectively). We report that there is no change in the internal symmetry of the cubosomes up to a threshold concentration of the guest components. Cubosomes are characterized by dynamic light scattering (DLS), SAXS, confocal microscopy, and cryo-TEM. Both poly-ϵ-lysine coated and uncoated cubosomes show remarkable stability in serum solution, are nontoxic and, are capable of charge specific targeting.

We show that the size of silica nanoparticles influences the nature of their aggregation in an aqueous solution of a relatively hydrophobic nonionic surfactant, $C_{12}E_4$. We present results for dispersions of silica nanoparticles with sizes varying from 8 to 26nm, in a 75 : 25 $C_{12}E_4$/water system, that forms a lamellar (L_α) phase at room temperature. Addition of silica particles does not affect the formation of the L_α phase. Nanoparticles smaller than

about 11nm aggregate irreversibly in the $C_{12}E_4$/water system. However, nanoparticles larger than about 15nm aggregate in the L_α phase, but are dispersed at temperatures above the L_α order-disorder temperature. Thus, in contrast to the smaller particles, silica nanoparticles larger than about 15nm in size exhibit reversible aggregation with change in temperature. These results are rationalized by the size-dependent wrapping of nanoparticles by surfactant bilayers. Larger particles, above 15nm in size, are sterically stabilized by the formation of an adsorbed surfactant bilayer. The cost of bilayer bending inhibits adsorption onto the highly curved surfaces of smaller particles, and these 'bare' particles aggregate irreversibly.

An alternating copolymer of maleic anhydride and vinyl methyl ether (PMAVME), disperses in water to form a turbid solution. We report that complexation of PMAVME with nonionic surfactant $C_{12}E_9$ drastically reduces the dispersion turbidity. Such complexes find applications in personal care formulations for targeted delivery of hydrophobic active compounds. PMAVME is predominantly hydrophobic and forms a turbid solution in water because of the formation of large aggregates that scatter visible light. Complexation with $C_{12}E_9$ results in the formation of micellar structures along the hydrophobic backbone of PMAVME, thus masking the intramolecular hydrophobic interactions. PMAVME:$C_{12}E_9$ $1:1$ complexes in water show multiple relaxations in dynamic light scattering. We demonstrate that these complexes undergo a liquid–liquid phase separation at a concentration of 5%. While the local micellar aggregate structure does not change significantly as a function of dispersion concentration, large concentration fluctuations are observed above the liquid–liquid phase separation resulting in a significant increase in the forward scattering of visible radiation.

This page is intentionally left blank.

Contents

List of Figures

Figure 2.4 The lattice parameter obtained from the peak positions of the bicontinuous cubic phase $Ia3d$ as a function of silica concentration.

Figure 2.5 The SAXS pattern of $Pn3m$ (lipid 65%− water 35% at 30°C) for different colloidal silica concentrations. The structure factor peak arising at $q = 0.0699\text{Å}^{-1}$ indicates neighboring nanoparticles correlations. Starting from 1.5% of silica concentration, a new peak appears as highlighted by the black arrows, indicating the coexistence of $Pn3m$ and $Ia3d$ phases.

Figure 2.6 The lattice parameter of the $Pn3m$ phase as a function of silica concentration.

Figure 2.7 The variation of $Ia3d$ H_II order order transition temperature as a function of silica concentration.

Figure 2.8 SAXS profiles of the inverse hexagonal phase H_II (lipid 75%− water 25% at 75°C) with different nanoparticle concentrations. The peak positions shift with particle concentrations. There is a structure factor peak developing upon increasing concentration at a q value of 0.0745Å^{-1}.

Figure 2.9 A close-up of the first Bragg peak of the SAXS pattern of the hexagonal phase. We can see that the first Bragg reflection initially shifts to lower q values up to a threshold concentration and then inverts the tendency moving toward higher q values. The dotted arrow indicates the path of the shift on the Bragg reflection.

Figure 2.10 The lattice parameter obtained from the position of the Bragg peaks of the hexagonal phase plotted against the colloidal silica concentration.

Figure 2.11 The SAXS profiles of lamellar phase L_α (lipid 90%–water 10%) as a function of nanoparticles concentration. A structure factor corresponding to the

This page is intentionally left blank.

List of Tables

CHAPTER 1

INTRODUCTION

CHAPTER 2

PHASE BEHAVIOUR OF LIPID-BASED LYOTOPIC LIQUID CRYSTALS IN PRESENCE OF COLLOIDAL NANOPARTICLES

CHAPTER 3

TARGETING AND DELIVERY OF HYDROPHOBIC COMPOUNDS USING NANOPARTICLES OF MONOGLYCERIDE CUBIC PHASE

CHAPTER 4

NANOPARTICLE SIZE CONTROLS AGGREGATION IN LAMELLAR NONIONIC SURFACTANT MESOPHASE

CHAPTER 5

STRUCTURE AND DYNAMICS OF CONCENTRATED POLYELECTROLYTE SOLUTIONS IN PRESENCE OF NONIONIC SURFACTANTS

CHAPTER 6

CONCLUSIONS AND FUTURE WORK

Chapter 1

Introduction and Literature

Contents

1.1 Introduction

When inclusions, such as colloidal particles or polymers, are dispersed in a surfactant matrix, inter-inclusion interactions are modified.[1–6] The assembly of guest moieties in such systems is mediated by the matrix surfactants. In turn, organization of the matrix surfactant is also found to be influenced by the presence of the guest moieties in the system.[7–10] The assembly and phase behaviour of colloids in a surfactant matrix is a problem of fundamental interest. Such assemblies are present in biological systems, foods and cosmetic products. The structure and properties of assemblies of colloids and polymers in surfactant matrices are discussed in this thesis. In this Chapter, we first discuss different surfactant assemblies, mainly focusing on nonionic surfactants. We are interested in nonionic surfactants, since they are insensitive to the effect of ionic strength and pH. We explore the length scales of such assemblies and their energetics. The parameters governing phase change and thermodynamics of self-assembly are briefly discussed after that. The effect of incorporation of guest components and their effect on phase behaviour is discussed. We then introduce the assembly of polyelectrolytes in a surfactant matrix and describe their structure and their dynamics. Finally, we conclude the chapter with a discussion on the motivation and outline of this thesis.

1.2 Surfactants and Self-assembly

1.2.1 Surfactants

Surfactants (contraction of the term surface-active agent) have a tendency to adsorb at the air-water interface and thereby reduce the surface tension of water.[11,12] In general, water is used as the solvent and therefore surfactants are amphiphiles. Surfactants consists of two parts, one of which is highly soluble in water while the other is apolar that are covalently linked. Thus, in a mixture of polar and non-polar solvents, surfactants

are localized at the two-fluid interface and reduce the interfacial energy of the system. Accumulation of surfactants at the interface reduces interfacial energy because the free energy of a surfactant molecule localized at the interface is lower than that solubilized in the bulk. This finds applications in many situations where a decrease in surface tension is required.

Surfactants are generally classified into the following categories based on the surfactant head group type:

- *Anionic and cationic* : Here, the surfactant has a charged headgroup that dissociates in water and releases a counter-ion.
- *Non-ionic* : That has a highly polar uncharged moiety as the headgroup.
- *Zwitterionic* : Where the headgroup comprises both a positive and a negatively charged group, that are covalently linked.

New materials having enhanced aggregation properties and interactions have recently emerged. Molecules such as catanionics (equimolar mixture of cationic and anionic surfactants), bolaforms (two charged headgroups connected by a long linear polymethylene chain), gemini surfactants (two identical surfactants connected by a spacer) and polymeric surfactants (polymer with surface active properties) posses enhanced aggregation properties because of their structure.[13–15] Surfactants can be either natural or synthetic in origin. Natural surfactants[16] include glycerol based surfactants that are widely used as emulsifiers in various food products and phospholipids that are an integral part of the cell membrane. Among synthetic surfactants, anionics find the most applications as detergents, soaps, and in personal care products, because of their low manufacturing cost. Where detergents and emulsifiers are required to be used at lower temperatures, nonionics are used because of their strong affinity for water arising from dipole-dipole interactions. The advantage of nonionic surfactant is that they can be tailored for use in a variety of

applications by varying the length of hydrophobic and hydrophilic groups. Further, nonionics are inert to changes in solution conditions such as pH or ionic strength. Examples of nonionic surfactants include polyoxyethylene ethers and monoglycerides, surfactant systems that are explored in this thesis.

1.2.2 Self-assembly

Self-assembly of amphiphiles happens as result of competition between two opposing forces where, one tends to decrease and the other tends to increase the interfacial area a, per molecule exposed to the aqueous phase. The former is the hydrophobic attraction due to the interfacial tension at the hydrocarbon-water interface and the latter is the repulsion of the hydrophilic head groups in self-assembled structures. These two opposing forces lead to an optimal headgroup area for which the interaction energy per lipid molecule is a minimum. This simplified geometric view of micellization can be expressed in terms of a dimensionless number known as the 'critical packing parameter' (CPP), that characterizes the self-assembly. Specifically, the type of self-assembled structure formed varies with the value of the CPP$= v/(al)$, where v is the volume occupied by the hydrophobic tail, l is the length of the hydrophobic tail and a is the head-group surface area.

Spherical micelles are formed when the optimal head group area, a_0, is sufficiently large or the hydrocarbon volume v sufficiently small in order to keep the radius of the micelle R below the critical length l_c (Figure 1.1). Thus, we have CPP$< 1/3$ for spherical micellar structures. Spherical micelles are commonly formed by ionic surfactants since the headgroup charge results in a large effective area in these systems. In the presence of salt, the headgroup area significantly reduces due to charge screening and thus, the CPP falls, such that $1/3 <$ CPP $< 1/2$. In this case, the surfactants pack into cylindrical (rod-like) micelles. Lipids that possess a small headgroup area and that have a CPP

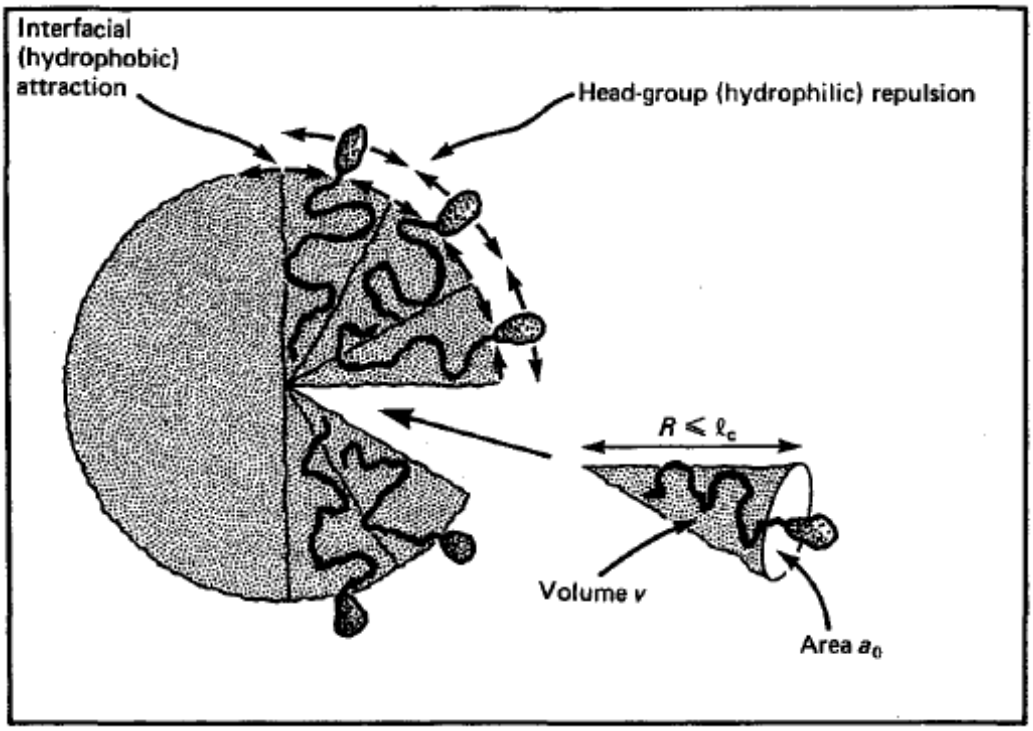

Figure 1.1: A typical micelle with a hydrocarbon in fluid state at the interiors (Figure adapted from Israelachvili[11] with prior permission).

close to 1 form bilayers. Using geometric considerations, one can see that when the outer lipids pack into truncated cones, bilayers can curve to form vesicles. Thus, lipids can self-assemble to form a particular aggregate structures depending on the value of the CPP.

At high concentrations, surfactants can organize to form liquid crystalline (LC) phases. There are different types of LC phases possible in a surfactant-water system. The critical packing parameter provides a convenient measure for determining the type of liquid crystalline phase formed in a system.[18] Although many LC phases are possible, there are three major LC phases that one encounters viz. lamellar, cubic and hexagonal. The LC structure formed is determined by the nature of the surfactant used, as well as concentration, ionic strength, pH, temperature etc.

The lyotropic lamellar phase is a frequently encountered LC phase when surfactant

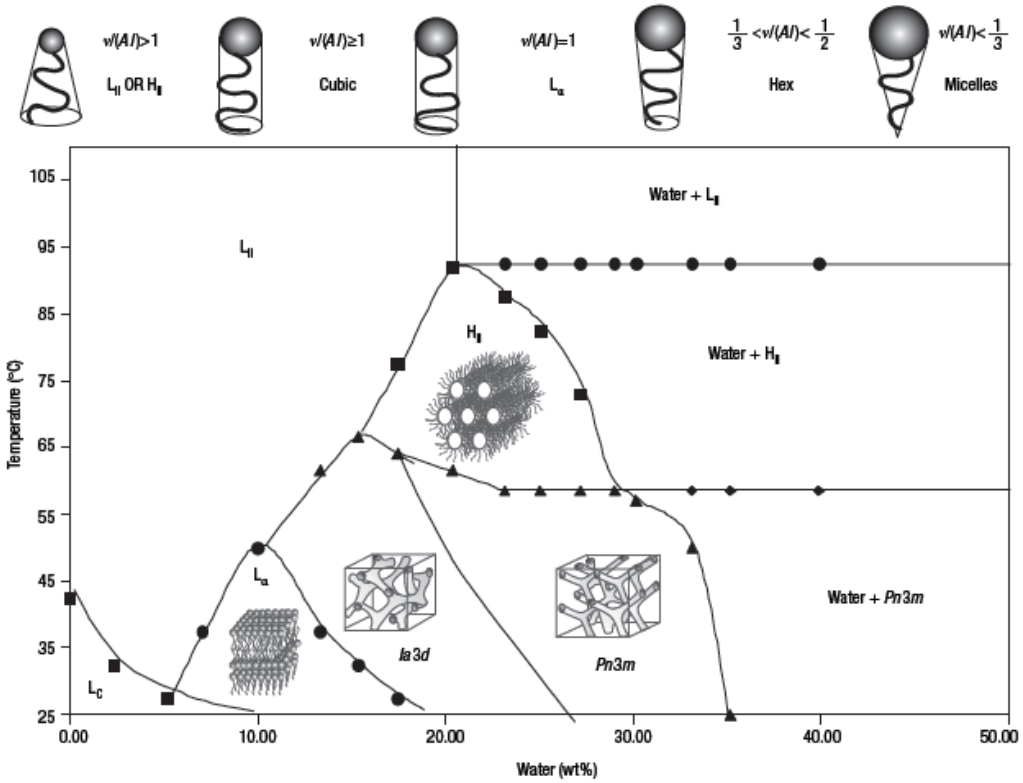

Figure 1.2: Phase diagram of the Dimodan U/J as obtained by showing the different structure formed with different values of CPP. "Reprinted with permission from (Mezzenga and Michel[17])"

molecules are dissolved in polar solvents like water at certain specific concentrations and temperatures. These phases are regularly stacked planar surfactant membranes separated by a solvent. Each membrane is a bilayer of surfactant, typically 20Å thick. A bilayer is characterized by its mean and Gaussian curvatures denoted by H and K, respectively. These are given by

$$H = \frac{c_1 + c_2}{2} \tag{1.1}$$

and

$$K = c_1 c_2 \tag{1.2}$$

where c_1 and c_2 are the principal curvatures. The mean curvature H changes with bending and the Gaussian curvature K changes with stretching the bilayer. Depending on

the value of the curvatures, different phases can form.[19,20] Spherical micelles and inverse micelles have positive Gaussian curvature K where the surface forms are elliptic.[19] When one of the principal curvatures is zero, the Gaussian curvature is zero. Here, lamellar or hexagonal phases form and the surfaces are parabolic. Hyperbolic surfaces are formed when principal curvatures have opposite sign giving a saddle structure. Minimal surfaces are formed for principal curvatures of equal value and opposite sign, viz. mean curvature is zero. Schwarz P-surface, Schwarz D-surface and Gyroid are examples of minimal surfaces that are extended to infinity giving a porous structure.

1.2.3 Thermodynamics of Self-Assembly

Self-assembled molecular structures such as micelles, microemulsions, bilayers, vesicles and biological membranes are formed driven by weak interactions such as van der Waal's, hydrogen-bonding, hydrophobic or screened electrostatic interactions. Thus, a change in the solution conditions results in a change in the interaction between the structures and would result in a modification of shape and size of the self-assembled structures.

The free energy of a microemulsion is related to the surface tension of the oil-water interface area as

$$\Delta G_f = \gamma \Delta A - T\Delta S \tag{1.3}$$

where ΔG_f is the free energy of microemulsion, γ is the surface tension of the oil-water interface, ΔA is the change in interfacial area on microemulsification, ΔS is the change in entropy of the system, and T is the temperature. For spontaneous microemulsification, large reductions in surface tension are observed with favourable entropy change to produce a negative free energy of formation. Equilibrium thermodynamics demands that the chemical potential of molecules in different aggregates in solution is the same. Thus,

$$\mu = \mu_1^0 + kT \log X_1 = \mu_2^0 + \frac{1}{2} kT \log \frac{1}{2} X_2 = \mu_3^0 + \frac{1}{3} kT \log \frac{1}{3} X_3 = \ldots$$

or

$$\mu = \mu_N = \mu_N^0 + \frac{kT}{N} \log \left(\frac{X_N}{N} \right) = \text{a constant, } N = 1, 2, 3, \ldots \tag{1.4}$$

where μ_N is the mean chemical potential of a molecule in an aggregate of aggregation number N, μ_N^0 is the mean interaction energy per molecule for an aggregate of aggregation number N, and X_N is the concentration of molecules in aggregates of aggregation number N. N takes values $1, 2, 3, \ldots$ for monomers, dimers, trimers etc. in solution. We can write the above equation (Eq 1.4) as

$$X_N = N \left(X_1 \exp \left[\frac{\mu_1^0 - \mu_N^0}{kT} \right] \right)^N \tag{1.5}$$

Large stable aggregates form when $\mu_N^0 < \mu_1^0$ for some value of N.

The competition between hydrophobic attraction between the molecules at the water interface and, the hydrophilic, steric or ionic repulsion between the headgroups, governs the self-assembly of amphiphiles. The attractive interaction is proportional to a positive interfacial free energy per unit area which, typically has a value between 20mJm^{-1} and 50mJm^{-1}. The repulsive contributions are found to be approximately proportional to the surface area occupied per head group, a. So the total interfacial free energy per molecule in an aggregate is written as:

$$\mu_N^0 = \text{Bulk term} + \text{Surface term} + \text{Curvature term} + \text{Packing term}$$

or

$$\mu_N^0 = \mu_N^B + \mu_N^S + \mu_N^C + \text{Packing term} \tag{1.6}$$

The bulk term gives the hydrophobic free energy for removing a hydrocarbon tail from water to within the micellar interior, that is approximated as a bulk oil-phase. Those

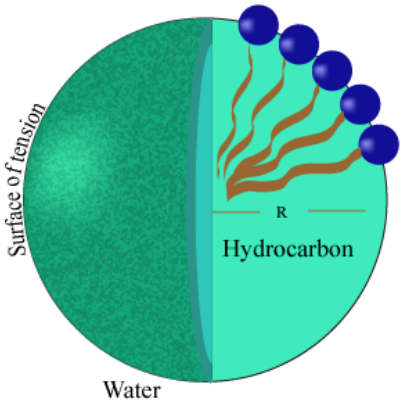

Figure 1.3: Schematics of a model micelle of radius R

tails that are still in contact with water are represented by a surface energy term $\gamma_i a$, where a is the area per surfactant molecule, and γ_i is the interfacial tension.

There is a repulsive interaction that arises from steric repulsion, hydration, electrostatic and other forces. Since the other forces are not completely quantified and, the electrostatic force $\propto 1/a$, the total surface contribution is written as

$$\mu_N^S = \gamma_i \left(a + \frac{a_0^2}{a} \right) \tag{1.7}$$

Expression 1.7 has a minima ($2\gamma_i a_0$) for an optimal value of a_0. Thus, the interaction energy between the lipids is a minimum for a particular value of head group area a_0 at which the aggregate structures form. Further, it is possible to replace the surface term $\gamma_i a_0^2/a$ by $a(1+\frac{D}{R})$ for a curved surface, in order to accommodate curvature effects, where R is the mean radius of curvature (Figure 1.3) and D is the Debye length. The 'packing term' arises since we model the interior of the micelle as fluid-like characterized by the bulk density of the fluid. Thus we impose a condition that $R < l_c$, where l_c is the critical tail length.

The aforementioned models are sufficient to explain the observed phase behaviour in the self-assembled structures. However, the parameters in these models require detailed

knowledge of the system under investigation and a good understanding of the approximations applied.

1.3 Guest Inclusions in Self-assembled Structures

1.3.1 Lyotropic Lamellar Phase

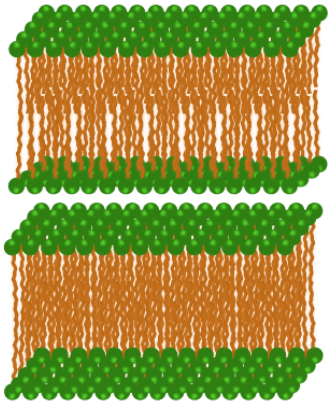

Figure 1.4: Schematic cartoon of a lamellar phase.

Bilayers are formed when the lipid/surfactant has a CPP value near 1; i.e., lipids having a small head group or bulk apolar chain self-assemble into bilayers. Thus, lipid having two tails is likely to form bilayers. The bilayer is considered as the basic building block of several other ordered phases, such as lamellar, bicontinuous cubic, vesicles etc. Lamellar phases are observed to give a SAXS pattern with peak positions in the ratio $1 : 2 : 3 : 4 \ldots$. Cationic dialkyl dimethyl quarternary ammonium surfactants and aerosol OT are some common examples of bilayer forming surfactants at room temperature. Nonionic surfactants such as $C_{12}E_3$, $C_{12}E_4$, $C_{12}E_5$, $C_{12}E_6$ and monoglycerides also form a lamellar phase at specific concentrations in water under ambient conditions.

Self-assembled structures, particularly lamellar and hexagonal phases, are known to host guest components, thus providing a platform for the self assembly. In recent years,

there has been a considerable interest in studying lamellar phase containing nanoparticles due to their potential applications in material science and as a model system for many biological processes. An example is the phospholipid bilayer, a most important part of the living cells, which partitions neighbouring compartments and governs transport processes. The transport includes molecules and particles of size ranging from angstroms to microns. The transport of particles through these membranes depends on the size of the particles: subnanometer particles penetrate the membranes while larger particles are enveloped by the membranes. An analogue of such biological systems are bilayer vesicles with colloidal inclusions which mimics the transport of particles through the membranes.[21]

The Helfrich interactions which stabilizes the lamellar phase are found to get modified with the inclusion of the guest components such as colloids and polymers. Attractive van der Waal's interactions result in a collapse of the bilayer structure in the absence of repulsive interactions. The repulsive contribution comes from the steric force given by bilayer undulations.[22–26] These interactions can be experimentally determined by X-ray scattering.[26] Theoretical models put forward by Helfrich[22] relate the undulations in the bilayer system to the smectic curvature modulus $K = \kappa/d$ and smectic compression modulus $\overline{B}$. He explains the stability of the lamellar phase as arising from a competition between elastic energy of the membrane and the thermal energy (which sets the amplitude of the fluctuations).

Depending on the type of guest components used, the system can have different properties. It was found that neutral polymers causes an attractive inter-lamellar attraction leading to destabilization of the lamellar phase.[7,27] When one dopes colloidal particles in the lamellar phase, the Helfrich interaction is mediated by the particles. The first attempt towards lamellar-nanoparticle composites were reported by Fabre et al.[28] when they prepared 'ferrosmectics' by incorporating magnetic nanoparticles in lyotropic lamellar phases. Dabadiet et al.[29] showed that the lyotropic lamellar phase is modified to

introduce additional features of magnetic response by incorporating magnetic nanoparticles of 10nm size. A swollen lamellar phase can accommodate particles up to a certain critical concentration without affecting the phase behaviour. Salamat and Kaler[30], Imai et al.[31] showed that the phase behaviour of $C_{12}E_5-C_6E_0-H_2O$ system is modified upon the addition of charged colloids of size smaller than the inter-bilayer spacings. The study also proposed a thermodynamic model for the phase transition. Most of the studies mainly concentrate on the inclusion of hydrophobic particles in the lamellar phase to study their effect on the bilayer stability.

Recently Imai et al.[7] showed that it is possible to modify the interactions that stabilize these phases by introducing guest components in the system.[9,10,31–35] Vandoolaeghe et al.[36] observed a strong interaction between liquid crystalline nanoparticles and multilamellar vesicles leading to a structural change in the internal symmetry of the nanoparticles. They proved that the steric hindrance of the colloidal particles restricts the undulations of the bilayer membranes. It was found by Ponsinet and Fabre[35] that both the bending modulus K and the compression modulus $\overline{B}$ change drastically in the case of a ferrosmectic when compared to a conventional lyotropic phase. They proposed a theoretical model for this. Recently Suganuma et al.[9] has shown that the lamellar phase transforms to micelles, when colloidal particles of concentration beyond a critical value, are added to the lyotropic lamellar phase. An attempt to probe the structure of the colloidal particles trapped in the surfactant mesophases was first made by Terentjev[37] when he theoretically proposed the evolution of a new type of defect gel formed by particles located in the defects of a Smectic-A liquid crystal. Later Alexeev et al.[1] showed that the ordered lamellar mesophase excludes particles by creating large defect boundaries when the particle size is larger than the inter-bilayer spacings.

The transport of nanoparticles through a biological membrane is a very important problem in biology and in physics.[21,38–40] For example, when viruses enter or leave a

cell, this transport is mediated by the virus particle getting wrapped by the cell bilayer in many instances. The bilayer elastic energies play a major role in such processes. Deserno[21], Deserno and Gelbart[38] have presented a theoretical frame work for such transport that accounts for variations in colloidal size, bilayer tension, etc. The curvature elastic energy per unit area is given by[41–44]

$$g_c = \frac{1}{2}k_c(c_1 + c_2 - c_0)^2 + \overline{k}_c c_1 c_2 \tag{1.8}$$

where c_1 and c_2 are the principal curvatures, c_0 is the spontaneous curvature, k_c is the bending rigidity, and $\overline{k}_c$ is the elastic modulus and the Gaussian curvature is c_1c_2. The bending elastic modulus is normally found to be of the order of $10k_BT$. Thus, it is possible for a large particle to get coated by a bilayer without a significant change in bilayer bending energy.[38]

The visual observation of liquid crystals through a polarized optical microscope reveals a wide variety of visual patterns due to the defect structure in the liquid crystalline phase.[45–48] Normally defects appear when a liquid crystalline phase is quenched from the isotropic phase.[49] Previous reports have developed a phenomenological model for the defect dynamics of a Smectic-C liquid crystal formed by quenching from a Smectic-A structure. Particles doped in a lamellar phase modify interactions stabilizing the host matrix and partition into the defects and stabilize the defect network against coarsening.[50] Basappa et al.[51] demonstrated that the oily streak networks formed by the lyotropic lamellar phase can also be stabilized against oscillatory shear by doping colloidal particles in it. It is known that there is a phase change associated with shear in the case of lamellar phase,[52] and reports show that the phase lose its stability following a phase separation when the shear rate is above a critical value. Shear is consider to perturb the ordering of liquid crystals. Depending on the order found in the phases, the effects of shear may vary. In the case of a phase with short range order, shear melting may

be observed. This phenomenon is useful in many applications where the defect structure is required to be stabilized, such as colloidal patterning and templating. Most of the reported work focuses on the effect of nanoparticles of size smaller than the bilayer spacings where the colloids are confined between the swollen bilayers. A detailed understanding of the effect of colloidal size and concentration on organization of nanoparticles in a surfactant matrix is still not available.

Within the surfactant mesophases,[1,53,54] interactions between guest components is also modified. Terentjev[37] suggested that colloidal particles doped in a smectic phase act as point defects in the phase, which mutually attract. Several studies on this regard have been performed on the interactions and phase behaviour of colloids and polymers in surfactant mesophases.[30,55–58] Koehler and Kaler[56] showed that negatively charged colloids undergo phase separation in nonionic surfactant solutions. Using latex particles in a hyperswollen lamellar phase, Yamamoto and Tanaka[59] showed that the smectic order can be controlled by modulating particle motion using an external field. Depending on the type of guest component added, it is localized in the hydrophilic or hydrophobic part of the bilayer. In recent years, there has been considerable interest in studying lamellar phases containing nanoparticles due to their potential applications in material science and as model systems for many biological processes. Kimura et al.[39] investigated the dynamics of colloidal nanoparticles in a swollen lyotropic lamellar phase using ac electrophoretic light scattering. Recently Ruiz-Herrero et al.[60] have studied the transport of a spherical nanoparticle through a lipid bilayer and showed that the nanoparticle get wrapped by the bilayers. These findings have direct significance for drug delivery using nanoparticles loaded with drugs[21,38,61] and, in processes such as endocytosis. Hydrophobic components partition into the alkyl chains of the bilayers. This property is potentially useful in delivering hydrophobic drugs in delivery systems.[62–65] Researchers have also investigated lamellar phases containing particles with different size, shape and

surface properties.[1,39,66–70] For example, Grillo et al.[67] have established a state diagram of the lyotropic lamellar phase with plate like laponite nanoparticles. They found that the laponite particles can be inserted between the bilayers when the thickness of the bilayer is comparable to that of the laponites. Still, the effect of particle size on the phase behaviour of lamellar phase is not fully understood. Similarly, the study of colloidal phase behaviour as a function of colloidal size within the host surfactant matrix is still in its infancy.

1.3.2 Cubic Phases

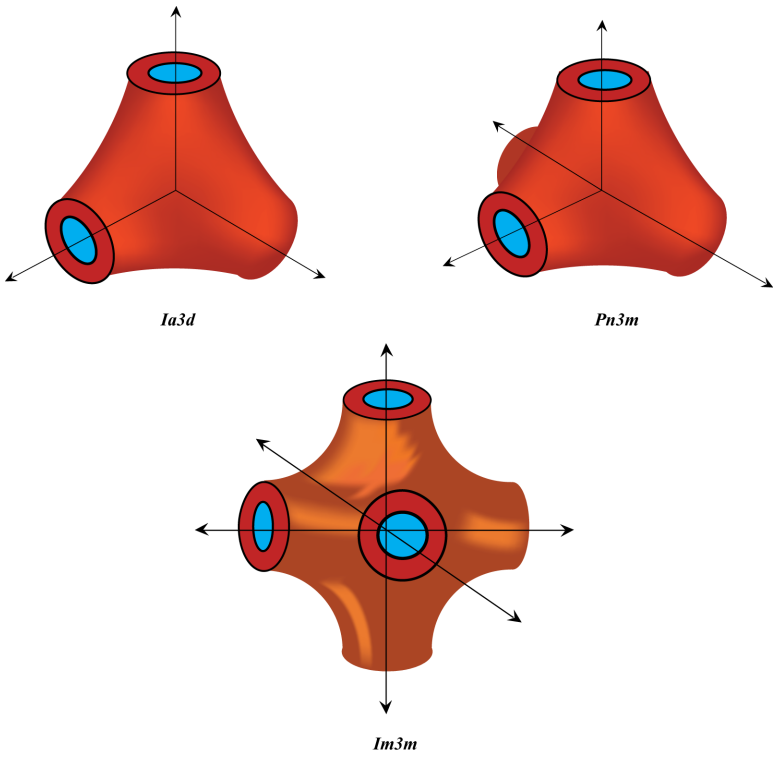

Figure 1.5: Three commonly found cubic phases in the case of monoglyceride-water system.

Bicontinuous cubic phases are organized into triply periodic minimal surfaces.[71,72] Cubic phases are formed as an intermediate between the lamellar and the hexagonal

phases.[73–75] Phase identification is done using X-ray scattering. Cubic phases formed have been identified with $Pm3n$, $Pn3m$, $Fd3m$, $Im3m$ and $Ia3d$ symmetry. Since common cubic phases are optically isotropic, they appear dark in polarized optical microscopy. Cubic phases $Pn3m$, $Ia3d$ and $Im3m$ are formed when the bilayers are draped onto a gyroid, F and P minimal surfaces respectively. These structures have been determined[76–79] and it has been found that they consist of two distinct water channels separated by the minimal surface.[80–82] In the $Ia3d$ phase, the water channels meet at 3-way junctions at 120°, while for $Pn3m$, the water channels meet at 4-way junctions at a tetrahedral angle of 109.5°. For the $Im3m$ phase, the water channels meet at angle of 90° in a 6-way junction. In the diffraction patterns obtained from the X-ray scattering curves, the reciprocal spacings of the Bragg peaks are given by

$$S_{hkl} = \frac{\sqrt{h^2 + k^2 + l^2}}{a} \tag{1.9}$$

where h, k, l are the Miller indices of the X-ray peaks and a is the lattice parameter. The $Pn3m$ phase is identified by the peaks at q positions in the ratio $\sqrt{2} : \sqrt{3} : \sqrt{4} : \sqrt{6} : \sqrt{8} : \sqrt{9} : \sqrt{10} : \sqrt{11} \ldots$ while the $Ia3d$ phase has Bragg peaks at q positions in the ratio $\sqrt{6} : \sqrt{8} : \sqrt{14} : \sqrt{16} : \sqrt{20} : \sqrt{22} : \sqrt{24} : \sqrt{26} \ldots$. The cubic phase has attracted special interest in biophysical and biomedical fields. The cubic phase is used in the field of protein crystallization[83–89] and controlled drug delivery.[90–95] Other bicontinuous phases, such as the sponge phase are also seen in many systems. The sponge phase has a 3-D lipid bilayer surrounded by two different water channels, but does not form a periodically ordered structure.

Monoglycerides have attracted much interest due to the many industrial applications of these lipids.[62,65,75,93,96–99] Monoolein, is a biodegradable, food grade lipid that has potential for use in pharmaceutical applications as a drug delivery vehicle[79] and there are currently 2200 registered US patents that relate to monoolein. Monoolein forms

different liquid crystalline phases when mixed with water and among these the cubic phase have particular importance. Larsson[74] identified two cubic phases observed in the case of monoolein-water system using X-ray scattering data.

Potential uses of monoolein in various applications demands the determination of the phase diagram in the presence of guest components. In many cases, the phase boundaries of the cubic phase shift depending on the concentration of the guest component used[8] Thus a complete determination of the phase diagram is required for designing an appropriate composition for a specific application. The effect of hydrophilic polymers on the phase diagram of the cubic phase has been reported previously by Mezzenga et al.[8]. The effect of the size and concentration of the added colloidal nanoparticles on the phase boundaries of the bicontinuous lipid-water cubic phase has not been elucidated. This area has implications for membrane biophysics, as many proteins behave like colloidal particles. Only few reports exist on the effects of colloidal particles on the LC phase behaviour.[9,30]

Dispersed particles of monoglycerides that retain their internal cubic phase symmetry are called cubosomes.[100–106] Cubosomes are prepared by dispersing the bicontinuous cubic phase in water by high energy homogenization. The so-formed cubic phase nanoparticles are unstable and are prone to aggregation. The stabilization of the nanoparticles is done using triblock copolymer PEO-PPO-PEO known as Pluronic F127.[107] Pluronic F127 is found to stabilize the nanoparticles without altering the internal structure of the nanoparticle (Figure 1.6).

Cubosome formulations allow simultaneous loading of hydrophobic and hydrophilic molecules, since the internal structure of the cubosome has amphiphilic character.[102,108] Many of the available drugs for pharmaceutical applications are insoluble in water. Hence improved mechanisms for drug delivery is currently an area of extensive research. Some of the emerging methods employ liposomes, where a hydrophobic drug can be delivered.

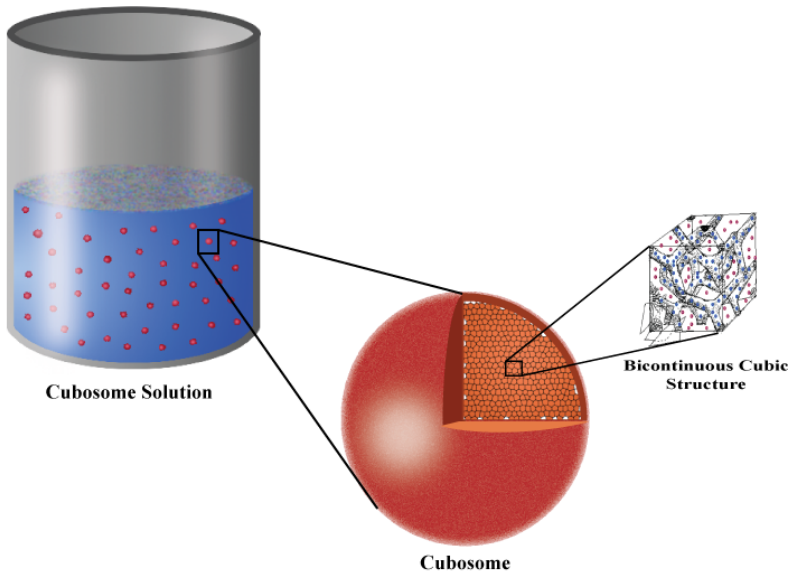

Figure 1.6: Cartoon representing a cubosome with $Pn3m$ internal symmetry.

The conventional drug delivery using liposomes suffers many disadvantage in terms of its loading capacity and the stability in biological fluids. Liquid crystalline phases formed by the monoglyceride-water systems can be tuned with a high payload for the sustained release of drugs over a prolonged time period.[62] Lipophilic and hydrophobic molecules can be solubilized or entrapped within the cubic phase.[109,110] Cubosomes have a higher loading capacity, and higher surface area per unit volume and higher mechanical and structural rigidity relative to liposomes.[98] Murgia et al.[98] have reported the application of cubosomes doped with two fluorescent probes in theranostic applications. One of the problems encountered in this formulation is the burst release of drugs. A potential solution to this problem has been recently provided by Driever et al.[111] who demonstrated the use of cubosomes coated with multiple layers of polyelectrolytes for retarded release of drugs. This method also has the advantage of introducing charge in the system. However, the process of creating multiple layers on cubosome surface is a complicated process involving many process parameters. Thus, a simpler method that retains all the

properties of cubosomes and that is capable of charge specific targeting is desirable.

1.4 Polyelectrolyte-Surfactant Systems

Cubosomes can be coated with polyelectrolytes in order to build barrier layers and to create a desired surface charge. Clearly, polyelectrolyte coated cubosomes need to be stable under physiological conditions. Polyelectrolytes can also form complexes with surfactants that can find use in controlled release applications. For such applications, a detailed knowledge of polyelectrolyte phase behaviour with external components should be known. Polyelectrolytes are prone to aggregation and phase separation on change of ionic strength, pH, etc. In biological systems, the interaction of the polyelectrolytes with biological membranes and other lipids is also important, as it is often observed in various pharmaceutical applications. The ability of polyelectrolytes to bind with surfactants is exploited in denaturation of proteins. The main challenge in developing such systems is to achieve an understanding of the solution behaviour of polyelectrolytes.

Polyelectrolyte solution properties are different from those of the colloids in some respects, yet they have some similarities.[112,113] Polyelectrolytes have many ionizable groups along the chain and dissociate into polyions in solution.[114,115] Due to the presence of the electrostatic interactions between the charges on the chain, the properties of polyelectrolytes are different from that of neutral polymers in solution.[114,116–119] Electrostatic interactions play a major role in the final structure of the polyelectrolyte in solution.[120] Thus, addition of electrolytes changes the ionic strength and drastically changes the properties of the polyelectrolytes in solution.[121–125] The structure and properties of polyelectrolytes depend on the solution ionic strength. At low salt-concentrations, the long range charge-charge repulsion results in an extended conformation for the polyelectrolyte chain. At high salt concentration, electrostatic interactions are screened and thus the polyelectrolyte adopts a random coil conformation.

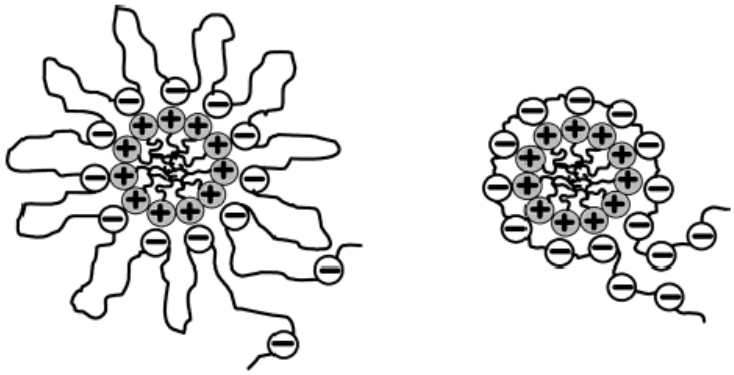

Figure 1.7: Schematic illustration of the interaction of a surfactant micelle with oppositely charged polyelectrolytes of different neutralization extents. "Reprinted with permission from (Plucktaveesak et al.[126]). ©(2003) American Chemical Society."

Polyelectrolyte conformations in solution also depend on the nature and amount of added surfactant.[126–130] The binding of the ionic surfactants of opposite on the polyelectrolyte has been extensively studied[126] (Figure 1.7). Precipitation is normally observed for complexes containing polyelectrolytes and oppositely charged surfactants.[131] Guillemet and Piculell[132] have shown that a liquid-liquid phase separation occurs near charge normalization when, oppositely charged surfactant is added to salt-free polyelectrolyte solutions. Also, the viscosity of such systems is found to decrease upon the addition of oppositely charged surfactant.[126] The structure and dynamics of polyelectrolytes are explained on the basis of an equilibrium association between the polyelectrolyte and the surfactant.[128] The association of surfactants with polyelectrolyte is widely used in health care products such as shampoos which normally contains a cationic polyelectrolyte and an anionic surfactant in excess. Thus a deeper understanding of polyelectrolyte-surfactant systems could lead to novel formulations in personal care products.

The structure of the complexes, when a nonionic surfactant is added to an aqueous solution of hydrophobically modified polyelectrolyte, was examined in detail by Deo and Somasundaram[133]. They found that the surfactant is incorporated within hydropho-

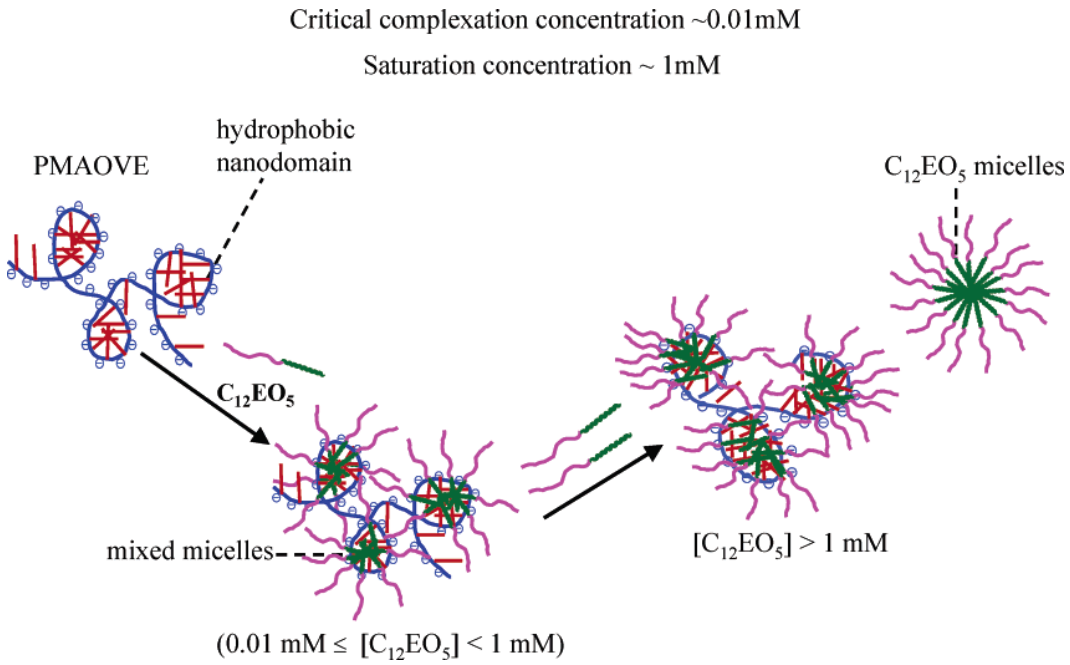

Figure 1.8: Typical structure formed by a hydrophobically modified polyelectrolyte (HMP)-nonionic surfactant complex. "Reprinted with permission from (Deo and Somasundaram[133]). ©(2003) American Chemical Society."

bic domains formed in the solution. Normally, a hydrophilic polyelectrolyte associates only with oppositely charged surfactant. Hydrophobic modification of the hydrophilic polyelectrolytes enables them to associate with nonionic surfactants and surfactants of the same charge.[128] While these studies are carried out at low polyelectrolyte/surfactant concentrations, these are not relevant to commercial formulations. An understanding of structures in concentrated polyelectrolyte/surfactant system is lacking.

1.5 Motivation and Objective of the Present Thesis

Surfactant-colloid and surfactant-polyelectrolyte system are often encountered in food, cosmetic and pharmaceutical products as described in section 1.2.1. Therefore it is important to understand the complete phase behaviour of such systems, to optimize the structure for specific applications. For example, colloid stabilized defect networks are

useful in photonic applications and cosmetics. Thus, the phase behaviour of the liquid crystalline phases should be completely determined in presence of the guest component as a function of size and concentration of the guest components.

Most of the reported studies are based on the hydrophobic nanoparticles doped within the LC matrices. A systematic study of the effect of concentration of hydrophilic colloids when doped within different liquid crystalline phases is not yet clearly understood. Previously our group has established that colloidal nanoparticles above a threshold size always phase separate to the domain boundaries of the hexagonal mesophase formed by the nonionic surfactant $C_{12}E_9$.[4] The effect of addition of colloidal nanoparticles to other liquid crystalline phases has not yet been studied in detail, particularly for monoglyceride based liquid crystalline phases. This is a model system in designing many pharmaceutical applications. Even though it exhibits a rich phase diagram, when mixed with water, the incorporation of hydrophilic nanoparticles in the LC phase formed by monoglycerides is yet to be investigated. We examine monolinolein liquid crystalline phases and study the effect of silica colloidal nanoparticles on its phase behaviour.

Monoglyceride cubic phase can be dispersed into nanoparticle called cubosomes having cubic phase internal symmetry. Cubic phase nanoparticles can be surface modified to endow them with additional functionality. We investigate the stability of such multifunctional cubosomes under physiological conditions.

The lamellar phase is an ideal model for biological membranes observed in Nature. The interaction between biological membranes and nanoparticles is relevant to many applications involving nanoparticles. A systematic study of the interaction and resultant structure of the nanoparticle and membrane as a function of size and concentration of the nanoparticles is explored. Finally, we investigate nonionic surfactant-polyelectrolyte complexes that have applications in health care and oral care applications.

In summary, this thesis investigates several aspects of nonionic surfactant-colloidal

interactions and the structure and dynamics of polyelectrolyte-surfactant complexes in the light of some possible practical applications.

1.6 Organization of Thesis

The relevant background literature on surfactant-colloid-polyelectrolyte structure is discussed in the present chapter. In the subsequent chapters, we explore a variety of experimental systems, starting with an examination of colloid phase behaviour in lyotropic liquid crystalline phases. The phase behaviour of colloidal nanoparticles of size comparable to the lattice spacing of the matrix liquid crystalline phase of 'monolinolein' is described in Chapter 2. We use small angle X-ray scattering (SAXS) and polarized optical microscopy (POM) as the main tools of investigation. In Chapter 3, applications of nanoparticles of the cubic phase formed by monoglyceride monoolein is described and some possible applications are demonstrated.

The interaction of the colloidal silica nanoparticles with membranes as a function of colloidal size and concentration is investigated using the lamellar phase of nonionic surfactant $C_{12}E_4$ in Chapter 4. In Chapter 5, the structure and dynamics of the polyelectrolyte solutions in presence of the nonionic surfactant $C_{12}E_9$ is investigated in detail.

The major outcomes of the present investigations and the possible practical applications including future work is presented in Chapter 6.

References

[1] Alexeev, V. L.; Ilekti, P.; Persello, J.; Lambard, J.; Gulik, T.; Cabane, B. *Langmuir* **1996**, *12*, 2392–2401.

[2] Sharma, K. P.; Kumaraswamy, G.; Ly, I.; Mondain-Monval, O.; Sharma, K. P.; Kumaraswamy, G.; Ly, I.; Mondain-monval, O. *J. Phys. Chem. B* **2009**, *113*, 3423–30.

[3] Kumaraswamy, G.; Sharma, K. P. *Adv. Planar Lipid Bilayers Liposomes*; Academic Press, 2013; Vol. 18; p 181.

[4] Kamendra P. Sharma, Organization of Nanoparticles and Polymers in Hexagonal Liquid Crystalline Phases of CnEm/Water Systems. Ph.D. thesis, National Chemical Laboratory, Pune, 2011.

[5] Sharma, K. P.; Gupta, S. S.; Kumaraswamy, G.; Ganai, A. K. *Chem. Mater.* **2011**, *23*, 1448–1455.

[6] Sharma, K. P.; Aswal, V. K.; Kumaraswamy, G. *J. Phys. Chem. B* **2010**, *114*, 10986–10994.

[7] Imai, M.; Mawatari, R.; Nakaya, K.; Komura, S. *Eur. Phys. J. E. Soft Matter* **2004**, *13*, 391–400.

[8] Mezzenga, R.; Grigorov, M.; Zhang, Z.; Servais, C.; Sagalowicz, L.; Romoscanu, A. I.; Khanna, V.; Meyer, C. *Langmuir* **2005**, 6165–6169.

[9] Suganuma, Y.; Urakami, N.; Mawatari, R.; Komura, S.; Nakaya-Yaegashi, K.; Imai, M. *J. Chem. Phys.* **2008**, *129*, 134903.

[10] Suganuma, Y.; Imai, M.; Nakaya, K. *J. Appl. Crystallogr.* **2007**, *40*, 303–306.

[11] Israelachvili, J. N. *Intermolecular and Surface Forces*, 3rd ed.; Elsevier Inc.: San Diego, 2011; pp 1–674.

[12] Evans, D. F.; Wennerstrom, H. *The Colloidal Domain*, 2nd ed.; Wiley-VCH: New York, 1999; pp 1–632.

[13] Zana, R. *Langmuir* **1996**, *12*, 1208–1211.

[14] Bleys, G.; Joos, P. *J. Phys. Chem.* **1985**, *89*, 1027–1032.

[15] Menger, F. M.; Littau, C. a. *J. Am. Chem. Soc.* **1993**, *115*, 10083–10090.

[16] Holmberg, K. *Curr. Opin. Colloid Interface Sci.* **2001**, *6*, 148–159.

[17] Mezzenga, R.; Michel, M. *Nat. Mater.* **2005**, *4*, 729–740.

[18] Hyde, S. T. *Prog. Colloid Polym. Sci.* **1990**, *82*, 236–242.

[19] Hyde, S. T. *Colloq. Phys.* **1990**, *C7*, 209–228.

[20] Seddon, J. M.; Templer, R. H. *Handb. Biol. Phys.*; 1995; Vol. 1; pp 97–160.

[21] Deserno, M. *Phys. Rev. E* **2004**, 031903.

[22] Helfrich, W. *Z. Naturforsch* **1973**, *28c*, 693–703.

[23] Castro-Roman, F.; Porte, G.; Ligoure, C. *Phys. Rev. Lett.* **1999**, *82*, 109–112.

[24] Lipowsky, R.; Leibler, S. *Phys. Rev. Lett.* **1986**, *56*, 2541–2544.

[25] Fru, T.; Fritz, G.; Freiberger, N.; Glatter, O.; Frühwirth, T.; Fritz, G.; Freiberger, N.; Glatter, O. *J. Appl. Crystallogr.* **2004**, *37*, 703–710.

[26] Petrache, H. I.; Gouliaev, N.; Tristram-Nagle, S.; Zhang, R.; Suter, R. M.; Nagle, J. F. *Phys. Rev. E* **1998**, *57*, 7014–7024.

[27] Masui, T.; Imai, M.; Nakaya, K.; Taniguchi, T. *J. Chem. Phys.* **2006**, *124*, 074904.

[28] Fabre, P.; Casagrande, C.; Veyssie, M. *Phys. Rev. Lett.* **1990**,

[29] Dabadiet, J. C.; Fabret, P.; Veyssict, M.; Cabuili, V.; Massart, R. *J. Phys. Condens. Matter* **1990**, *2*, 291–294.

[30] Salamat, G.; Kaler, E. E. W. *Langmuir* **1999**, *15*, 5414–5421.

[31] Imai, M.; Suganuma, Y.; Nakaya, K.; Komura, S. *J. Phys. Condens. Matter* **2005**, *17*, S2929–S2935.

[32] Imai, M.; Nakaya, K.; Kato, T. *Eur. Phys. J. E* **2001**, *5*, 391–402.

[33] Imai, M.; Yoshida, I.; Iwaki, T.; Nakaya, K. *J. Chem. Phys.* **2005**, *122*, 044906.

[34] Imai, M.; Kawaguchi, A.; Saeki, A.; Nakaya, K.; Kato, T.; Ito, K.; Amemiya, Y. *Phys. Rev. E* **2000**, *62*, 6865–6874.

[35] Ponsinet, V.; Fabre, P. *J. Phys. II Fr.* **1996**, *6*, 955–960.

[36] Vandoolaeghe, P.; Barauskas, J.; Johnsson, M.; Tiberg, F.; Nylander, T. *Langmuir* **2009**, *25*, 3999–4008.

[37] Terentjev, E. M. *Sov. Phys. Crystallogr.* **1988**,

[38] Deserno, M.; Gelbart, W. M. *J. Phys. Chem. B* **2002**, *106*, 5543–5552.

[39] Kimura, Y.; Mori, T.; Yamamoto, A.; Mizuno, D. *J. Phys. Condens. Matter* **2005**, *17*, S2937–S2942.

[40] Santangelo, C. D.; Kamien, R. D. *Proc. R. Soc. A Math. Phys. Eng. Sci.* **2005**, *461*, 2911–2921.

[41] Mitchell, D. J.; Ninham, B. W. *Langmuir* **1989**, *5*, 1121–1123.

[42] Winterhalter, M.; Helfrich, W. *J. Phys. Chem.* **1988**, *92*, 6865–6867.

[43] Evans, E.; Needham, D. *J. Phys. Chem.* **1987**, *91*, 4219–4228.

[44] Duwe, H. P.; Kaes, J.; Sackmann, E. *J. Phys. Fr.* **1990**, *51*, 945–961.

[45] Saupe, A. *J. Colloid Interface Sci.* **1977**, *58*, 549–558.

[46] Brinkman, W. F.; Cladis, P. E. *Phys. Today* **1982**,

[47] Sethna, J. P.; Kleman, M. *Phys. Rev. A* **1982**, *26*, 3037–3040.

[48] Dierking, I. *Textures of Liquid Crystals*, 1st ed.; Wiley-VCH Verlag GmbH & Co. KGaA: Viernheim, 2003; pp 1–218.

[49] Pargellis, A. N.; Finn, P.; Goodby, J. W.; Panizza, P.; Yurke, B.; Cladis, P. E. *Phys. Rev. A* **1992**, *46*, 7765–7776.

[50] Zapotocky, M.; Ramos, L.; Poulin, P.; Lubensky, T. C.; Weitz, D. A. *Science (80-.).* **1999**, *283*, 209–212.

[51] Basappa, G.; Kumaran, V.; Nott, P. R.; Ramaswamy, S.; Naik, V. M.; Rout, D. *Eur. Phys. J. E* **1999**, *12*, 269–276.

[52] Ramaswamy, S. *Phys. Rev. Lett.* **1992**, *69*, 112–115.

[53] Antonietti, M.; Conrad, J.; Hunemann, A. *Macromolelcules* **1994**, *27*, 6007–6011.

[54] Arrault, J.; Poon, W.; Cates, M. *Phys. Rev. E* **1999**, *59*, 3242–3252.

[55] Cluzeau, P.; Poulin, P.; Joly, G.; Nguyen, H. *Phys. Rev. E* **2001**, *63*, 1–4.

[56] Koehler, R. D.; Kaler, E. W. *Langmuir* **1997**, *13*, 2463–2470.

[57] Jayalakshmi, Y.; Kaler, E. *Phys. Rev. Lett.* **1997**, *78*, 1379–1382.

[58] Ramos, L.; Fabre, P.; Dubois, E. *J. Phys. Chem.* **1996**, *100*, 4533–4537.

[59] Yamamoto, J. U. N.; Tanaka, H. *Nat. Mater.* **2005**, *4*, 75–80.

[60] Ruiz-Herrero, T.; Velasco, E.; Hagan, M. F. *J. Phys. Chem. B* **2012**, *116*, 9595–9603.

[61] Bahrami, A. H. *Soft Matter* **2013**, *9*, 8642–8646.

[62] Ganem-quintanar, A.; Quintanar, D.; Buri, P. *Drug Dev. Ind. Pharm.* **2000**, *26*, 809–820.

[63] Sagalowicz, L.; Leser, M. E.; Watzke, H. J.; Michel, M. *Trends Food Sci. Technol.* **2006**, *17*, 204–214.

[64] Rios-Doria, J.; Carie, A.; Costich, T.; Burke, B.; Skaff, H.; Panicucci, R.; Sill, K. *J. Drug Deliv.* **2012**, *2012*, 951741.

[65] Negrini, R.; Mezzenga, R. *Langmuir* **2011**, *27*, 5296–5303.

[66] He, L.; Zhang, L.; Liang, H. *J. Phys. Chem.* **2008**, *112*, 4194–4203.

[67] Grillo, I.; Levitz, P.; Zemb, T. *Langmuir* **2000**, *16*, 4830–4839.

[68] Constantin, D.; Davidson, P. *ChemPhysChem* **2014**, *15*, 1270–1282.

[69] Sarkar, B.; Ayandele, E.; Venugopal, V.; Alexandridis, P. *Macromol. Chem. Phys.* **2013**, *214*, 2716–2724.

[70] Beneut, K.; Constantin, D.; Davidson, P.; Dessombz, A.; Chanéac, C. *Langmuir* **2008**, *24*, 8205–8209.

[71] Tate, M. W.; Eikenberry, E. F.; Turner, D. C.; Shyamsunder, E.; Gruner, S. M. *Chem. Phys. Lipids* **1991**, *57*, 147–164.

[72] Larsson, K. r.; Tiberg, F. *Curr. Opin. Colloid Interface Sci.* **2005**, *9*, 365–369.

[73] Friberg, S. *Naturwissenschaften* **1977**, *64*, 612–618.

[74] Larsson, K. *Nature* **1983**, *304*, 664.

[75] Qiu, H.; Caffrey, M. *Biomaterials* **2000**, *21*, 223–234.

[76] Luzzati, V.; Tardieu, A.; Gulik-Krzywicki, T. *Nature* **1968**, *217*, 1028–1030.

[77] Luzzati, V.; Tardieu, A.; Gulik-Krzywicki, T.; Rivas, E.; Reiss-Husson, F. *Nature* **1968**, *220*, 485–488.

[78] Lindblom, G.; Larsson, K.; Johansson, L.; Fontell, K. *J. Am. Chem. Soc.* **1979**, *101*, 5465–5470.

[79] Larsson, K.; Fontell, K.; Krog, N. *Chem. Phys. Lipids* **1980**, *27*, 321–328.

[80] Turner, D. C. D. C.; Wang, Z.-G.; Gruner, S. M.; Mannock, D. A.; McElhaney, R. N. *J. Phys. II Fr.* **1992**, *2*, 2039–2063.

[81] Rappolt, M.; Gregorio, G. M. D.; Almgren, M.; Amenitsch, H.; Pabst, G.; Laggner, P.; Mariani, P. *Europhys. Lett.* **2006**, *75*, 267–273.

[82] Marrink, S.-j.; Tieleman, D. P. *J. Am. Chem. Soc.* **2001**, *123*, 12383–12391.

[83] Ericsson, B.; Larsson, K.; Fontell, K. *Biochim. Biophys. Acta* **1983**, *729*, 23–7.

[84] Landau, E. M.; Rosenbusch, J. P. *Proc. Natl. Acad. Sci.* **1996**, *93*, 14532–14535.

[85] Caffrey, M. *Curr. Opin. Struct. Biol.* **2000**, *10*, 486–497.

[86] Caffrey, M. *J. Struct. Biol.* **2003**, *142*, 108–132.

[87] Misquitta, Y.; Caffrey, M. *Biophys. J.* **2003**, *85*, 3084–96.

[88] Cherezov, V.; Clogston, J.; Papiz, M. Z.; Caffrey, M. *J. Mol. Biol.* **2006**, *357*, 1605–18.

[89] Caffrey, M.; Cherezov, V. *Nat. Protoc.* **2009**, *4*, 706–731.

[90] Engström, S.; Nordén, T. P.; Nyquist, H.; Norden, T. P.; Engstrom, S. *Eur. J. Pharm. Sci.* **1999**, *8*, 243–54.

[91] Shah, J. C.; Sadhale, Y.; Chilukuri, D. M. *Adv. Drug Deliv. Rev.* **2001**, *47*, 229–50.

[92] Sallam, A.-S.; Khalil, E.; Ibrahim, H.; Freij, I. *Eur. J. Pharm. Biopharm.* **2002**, *53*, 343–52.

[93] Bender, J.; Ericson, M. B.; Merclin, N.; Iani, V.; Rosén, A.; Engström, S.; Moan, J. *J. Control. release* **2005**, *106*, 350–60.

[94] Fong, W.-K.; Hanley, T.; Boyd, B. J. *J. Control. Release* **2009**, *135*, 218–26.

[95] Guo, C.; Wang, J.; Cao, F.; Lee, R. J.; Zhai, G. *Drug Discov. Today* **2010**, *15*, 1032–40.

[96] Kulkarni, C. V.; Wachter, W.; Iglesias-salto, G.; Engelskirchen, S.; Ahualli, S. *Phys. Chem. Chem. Phys.* **2011**, *13*, 3004–3021.

[97] Mezzenga, R.; Meyer, C.; Servais, C.; Romoscanu, A. I.; Sagalowicz, L.; Hayward, R. C. *Langmuir* **2005**, *21*, 3322–3333.

[98] Murgia, S.; Bonacchi, S.; Falchi, A. M.; Lampis, S.; Lippolis, V.; Meli, V.; Monduzzi, M.; Prodi, L.; Schmidt, J.; Talmon, Y.; Caltagirone, C. *Langmuir* **2013**, *29*, 6673–6679.

[99] Spicer, P. T. *Cubosome Formation via Dilution Kinetic Effects and Consumer Product Implications*; 2003; pp 1–14.

[100] Gustafsson, J.; Ljusberg-wahren, H.; Almgren, M.; Larsson, K. *Langmuir* **1996**, *12*, 1994–1996.

[101] Spicer, P. T.; Hayden, K. L.; Chester, W.; Lynch, M. L.; Ofori-boateng, A.; Burns, J. L. *Langmuir* **2001**, *17*, 5748–5756.

[102] Spicer, P. T. *Curr. Opin. Colloid Interface Sci.* **2005**, *10*, 274–279.

[103] Barauskas, J.; Johnsson, M.; Joabsson, F.; Tiberg, F. *Langmuir* **2005**, *21*, 2569–2577.

[104] Drummond, C. J.; Fong, C. *Curr. Opin. Colloid Interface Sci.* **2000**, *4*, 449–456.

[105] Angelov, B.; Angelova, A.; Papahadjopoulos-Sternberg, B.; Lesieur, S.; Sadoc, J.-F.; Ollivon, M.; Couvreur, P. *J. Am. Chem. Soc.* **2006**, *128*, 5813–5817.

[106] Landh, T.; Larsson, K. Particles, method of preparing said particles and uses thereof. 1996.

[107] Landh, T. *J. Phys. Chem.* **1994**, *98*, 8453–8467.

[108] Nguyen, T.-H.; Hanley, T.; Porter, C. J. H.; Boyd, B. J. *J. Control. release* **2011**, *153*, 180–6.

[109] Amar-Yuli, I.; Wachtel, E.; Shalev, D. *J. Phys. Chem. B* **2008**, *112*, 3971–3982.

[110] Amar-Yuli, I.; Aserin, A.; Garti, N. *J. Phys. Chem. B* **2008**, *112*, 10171–10180.

[111] Driever, C. D.; Mulet, X.; Waddington, L. J.; Thissen, H.; Caruso, F.; Drummond, C. J. *Langmuir* **2013**,

[112] Kosmas, M. K.; Freed, K. F. *J. Chem. Phys.* **1978**, *69*, 3647.

[113] Rubinstein, M.; Colby, R. H. *Polymer Physics*; Oxford University Press, 2005; pp 1–548.

[114] Oosawa, F. *Polyelectrolytes*; Marcel Dekker: New York, 1971; pp 1–168.

[115] de Gennes, P.-G. *Scaling concepts in polymer physics*; Cornell University Press: Ithaca, 1979; pp 1–325.

[116] Noda, I.; Tsuge, T.; Nagasawa, M. *J. Phys. Chem.* **1968**, *137*, 710–719.

[117] de Gennes, P.-G. *Macromolecules* **1976**, *9*, 587–593.

[118] Odijk, T. *Macromolecules* **1979**, *12*, 688–693.

[119] Dobrynin, A. V.; Colby, R. H.; Rubinstein, M. *Macromolecules* **1996**, *28*, 1859–1871.

[120] Hauthal, H. G. *Surfactant polymer interactions, rheology and microemulsions, formulations, sustainability, forum for innovations*; 2011; Vol. 48; pp 87–99.

[121] Varoqui, R.; Strauss, U. P. *J. Phys. Chem.* **1968**, *72*, 2507–2511.

[122] Schultz, A. W.; Strauss, U. P. *J. Phys. Chem.* **1970**, *76*, 1767–1771.

[123] Bianchi, E.; Ciferri, A.; Parodi, R.; Rampone, R.; Tealdi, A. *J. Phys. Chem.* **1970**, *74*, 1050–1056.

[124] Dubin, P. L.; Strauss, U. P. *J. Phys. Chem.* **1970**, *74*, 2842–2847.

[125] Kam, Z.; Borochov, N.; Eisenberg, H. *Biopolymers* **1981**, *20*, 2671–90.

[126] Plucktaveesak, N.; Konop, A. J.; Colby, R. H. *J. Phys. Chem. B* **2003**, *107*, 8166–8171.

[127] Magid, L. *J. Phys. Chem. B* **1998**, *5647*, 4064–4074.

[128] Iliopoulos, I. *Curr. Opin. Colloid Interface Sci.* **1998**, *3*, 493–498.

[129] Hoffmann, I.; Heunemann, P.; PreÌvost, S.; Prévost, S.; Schweins, R.; Wagner, N. J.; Gradzielski, M. *Langmuir* **2011**, *27*, 4386–4396.

[130] Ricka, J.; Meewes, M.; Nyffenegger, R.; Binkert, T. *Phys. Rev. Lett.* **1990**, *65*, 657–660.

[131] Santos, O.; Johnson, E. S.; Nylander, T.; Panandiker, R. K.; Sivik, M. R.; Piculell, L. *Langmuir* **2010**, *26*, 9357–9367.

[132] Guillemet, F.; Piculell, L. *J. Phys. Chem.* **1995**, *99*, 9201–9209.

[133] Deo, P.; Somasundaram, P. *Langmuir* **2005**, *21*, 3950–3956.

Chapter 2

Phase Behavior of Lipid Based Lyotropic Liquid Crystals in Presence of Colloidal Nanoparticles

Contents

2.1 Introduction

Amphiphilic molecules mixed with selective solvents, such as water, form self-assembled structures among which lamellar, hexagonal and bicontinuous cubic phases are the most well-known.[1–3] In particular there has been a considerable interest in the properties and phase behavior of self-assembled mesophases formed by lipids and water because of their applications in food, cosmetics, pharmaceutical products and encapsulation systems.[4–7] For example, the liquid crystalline structures based on monoglycerides have attracted major interest in different pharmaceutical applications due to their excellent bio-compatible properties.[8] These lipid-water systems form prevalently inverted types of lyotropic liquid crystalline structures in which water domains are confined within a lipid matrix and adopt geometries of one-, two- or three-dimensional symmetries depending on whether hexagonal, lamellar, or cubic structures are formed as a function of water content, temperature, and length and degree of unsaturation of the hydrophobic chain.[3] The topology of these mesophases has been explained by both geometrical concepts such as triply periodic minimal surfaces (TPMS) or the critical packing parameter[3] or more recently by statistical physics approaches.[9,10] Furthermore it has been proved that the interactions which stabilize any of the two domains forming the mesophases, can be further tuned by adding colloidal nanoparticles partitioning in any of the domains.[11,12] It is well known that particles self-assemble when they are dispersed in an ordered matrix due to the entropic contributions originating by the mixing of the matrix and the particles.[13] The effect of guest components on the lyotropic lamellar phase has been investigated in detail by several groups[14–27] and Loudet et al. in their pioneering work showed colloidal ordering by the phase separation in liquid crystals.[28,29] The finally self-assembled system results from a balancing mechanism between entropic and energetic interactions. By doping a nanostructured matrix with colloidal nanoparticles of comparable size, additional interactions arising from the geometrical restrictions imposed by the ordered material

matrix may trigger structural changes in the hosting media itself. Non-ionic surfactant-colloid mixtures have been studied by several research groups.[19,30] In the hexagonal phase formed by the non-ionic surfactant $C_{12}E_9$ and water, hydrophilic colloidal nanoparticles have been shown to reversibly aggregate at the domain boundaries of the hexagonal phase.[31] Nanoparticles stabilizing a network of cholesteric mesophase have also been reported previously.[32,33] It was found that the colloids preferably assemble at the nodes and provide better stability against oscillatory shear.[33] Host-guest coupling in lyotropic liquid crystals in which the guest species is not an isotropic nanoparticle has also been considered by a number of authors.[34,35] The incorporation of biomolecules in the bicontinuous cubic phases and their potential applications been investigated in detail.[36–40] When polymer chains are added to lamellar lyotropic liquid crystals for example, a reduction of smectic compressibility has been reported.[41,42] In his earlier work, Terentjev proposed a theoretical model for the structure of smectic phases in presence of impurities, leading to condensation of defects which mutually attract and create nuclei for a new mesophase.[43] In inverted bicontinuous liquid crystals in presence of hydrophilic polymers, size-exclusion concepts and reduction of the free energy associated with polymer molecular configurations have also been invoked to rationalize order-order transitions.[44] Finally recent work has also discussed the encapsulation of highly anisotropic nanoparticles constituted of protein amyloid fibrils within lyotropic liquid crystals and the resulting templating effect in the orientations of both fibrils and mesophases.[45]

Although surfactant-colloid nanoparticle blends have been studied in detail, our understanding of the effects of particle size, concentration, surface functionality etc. on the hosting mesophase structure and properties is still in its infancy.

In the present work, we systematically investigate the microstructure and phase behavior of the lyotropic liquid crystalline phases formed by a monoglyceride (monolinolein) water system upon the addition of (silica) hydrophilic colloidal nanoparticles whose size

slightly exceeds the typical dimensions of water channels/layers. We combine various analytical techniques such as small angle X-ray scattering (SAXS), polarized optical microscopy (POM), freeze-fracture electron microscopy and differential scanning calorimetry (DSC) to extract structural information and elucidate phase behavior of the lipid-water-nanoparticles mixtures. We consider the behavior of the mixtures at different positions of the phase diagram so to screen different mesophase symmetries and we discuss the experimental findings in terms of the energetic and entropic contributions governing the system.

2.2 Experimental Section and Methods

2.2.1 Materials and Sample Preparation

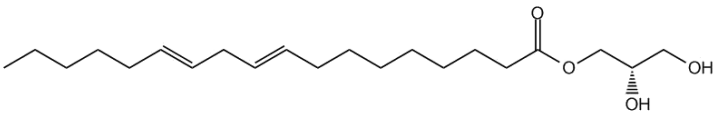

Figure 2.1: Molecular structure of monolinolein

DimodanU/J was a generous gift from Danisco (Brabrand,Denmark) and was used as received. This commercial-grade form of monolinolein contains more than 98$wt\%$ monoglyceride. The hydrocarbon tail consists predominantly of C18 chains (91%), distributed as follows: C18 : 2 (61.9%), C18 : 1 (24.9%), and C18 : 0 (4.2%) (where : 2, : 1, and : 0 refer to the number of unsaturations); additional lipids are C16 : 0 chains (7.4%) and a residual amount of diglycerides (1.6%). The mixing of saturated and unsaturated chains lowers the melting temperature of the L_c phase, yielding a larger region of the bicontinuous cubic structures in the phase diagram. The same single batch was used for all the measurements of the present work. The colloidal nanoparticles, Ludox® FM,

were received from Sigma Aldrich as electrostatically stabilized dispersions and were used without further modifications. The average diameter of the particle is found to be 5nm from TEM and 8nm using SAXS and dynamic light scattering (DLS) and has already been extensively characterized in previous literature.[31] All the experiments in this work are performed using the same batch of the Dimodan U/J and Ludox® nanoparticles.

The samples for the phase diagram of the monoglyceride-water mixture were prepared by following the protocol reported previously.[46] The monoglyceride and water in the required amounts and ratio were poured into a Pyrex tube with sealing cap and mixed by cyclic heating and vortexing until the sample became homogeneous. The tube was then cooled down, opened and a capillary was inserted, after which the same procedure was repeated again to allow centrifugation-assisted penetration of the sample within the capillary. Then the tubes were cooled again and the capillaries were extracted and rapidly sealed by epoxy resin. The monoglyceride liquid crystals with additional nanoparticles were prepared using the same protocol with the only difference that a suitable concentration of nanoparticles in the water dispersion was used instead of the pure water. By following this procedure we have chosen to maintain the monoglyceride-water ratio constant, allowing immediate identification of the mesophase in the pristine lipid- water phase diagram.

2.2.2 Small Angle X-ray Scattering

Small-angle X-ray scattering (SAXS) was used to establish the phase diagram to extract different structural information and to unravel the effects of nanoparticle inclusions in various regions of the phase diagram. SAXS measurements were performed using a microfocused Rigaku, X-ray source of wavelength $\lambda = 1.54$Å operating at 45kV and 88mA. Diffracted X-rays signal was collected on a gas filled two-dimensional detector. The scattering vector q was calibrated using silver behenate. Samples were sandwiched

between two thin mica sheets and sealed by a O-ring, with a sample thickness of ca 1mm. Data were collected and azimuthally averaged to yield one-dimensional intensity versus scattering vector q.

The lattice parameter of the phase is calculated from the positions of the Bragg reflections for a crystal lattice plane having Miller indices (hkl).[47,48] The positions of the Bragg reflections q_{hkl} for a d-dimensional liquid crystalline phase having a lattice parameter a is tabulated in Table 2.1. The q value of the peak position is found and the

Table 2.1: Positions of the Reflections q_{hkl} for Different Lattice Types

lamallae $(d = 1)$	$q_h = 2\pi h/a$
hexagonal $(d = 2)$	$q_{hk} = 4\pi\sqrt{h^2 + hk + k^2}/(\sqrt{3}a)$
square $(d = 3)$	$q_{hk} = 2\pi\sqrt{h^2 + k^2}/a$
cubic $(d = 3)$	$q_{hkl} = 2\pi\sqrt{h^2 + k^2 + l^2}/a$
hexagonal $(d = 3)$	$q_{hkl} = 2\pi\sqrt{\frac{4}{3}(h^2 + hk + k^2) + \frac{3}{8}l^2}/a$

peak is indexed with the corresponding Miller indices to find the lattice parameter for the phase from the formulae given in Table 2.1. The lattice parameter obtained for each peak in the spectrum is averaged to obtain a mean value of a.

2.2.3 Polarized Optical Microscopy

A first, coarse evaluation of the phase diagram was performed using optical microscopy between cross polarizers. This allowed identifying different liquid crystalline phases and their order-order and order-disorder transition temperatures. The samples were sandwiched between two glass slides and the experiments were carried out at different temperatures using a temperature-controlled stage connected to a ZEISS axio microscope. The images were acquired on a CCD camera. SAXS was employed at a second stage to further refine transitions and identification of the different mesophases.

2.2.4 Differential Scanning Calorimetry

Differential scanning calorimetry was carried out to resolve first order transition peaks corresponding to bound and free water in the hydrophilic domains of the inverted lyotropic liquid crystalline phases. Since the melting temperatures of the bound and free water are typically different, this technique can give insight into the thermodynamics of the liquid crystalline phase transitions. The experiments were performed on a Thermal Advantage DSC from TA Instruments. The samples were loaded in aluminum capsules contained in a steel sample pan of known mass and thermal conductivity. The experiments were carried out with an empty sample pan as the reference. Samples were allowed to equilibrate for 24h before the experiment and were then scanned for a temperature range starting from 40°C to 60°C with a scanning rate of 10°C/ min in a heat/cool/heat cycle.

2.3 Results and Discussion

2.3.1 Temperature-Composition Phase Diagram

The phase diagram of lipid-water system obtained using SAXS and POM is shown in Figure 2.2 and is verified according to Gibbs phase rule. We used SAXS to resolve the boundary between two regions where two phases coexist. The regions where liquid crystalline phases coexist with excess water are identified by observing the onset plateau of the lattice parameter with water concentration. Note that the phase diagram obtained here is slightly different from that published earlier.[2,46] This is due to the possible variations in the formulation of the Dimodan U/J grade, which can change slightly from batch to batch in the composition of minority components. The major changes observed with respect to previous reports are the boundaries separating the cubic and the inverse hexagonal phases where the order-order transition temperature is higher ($70-75$°C) than

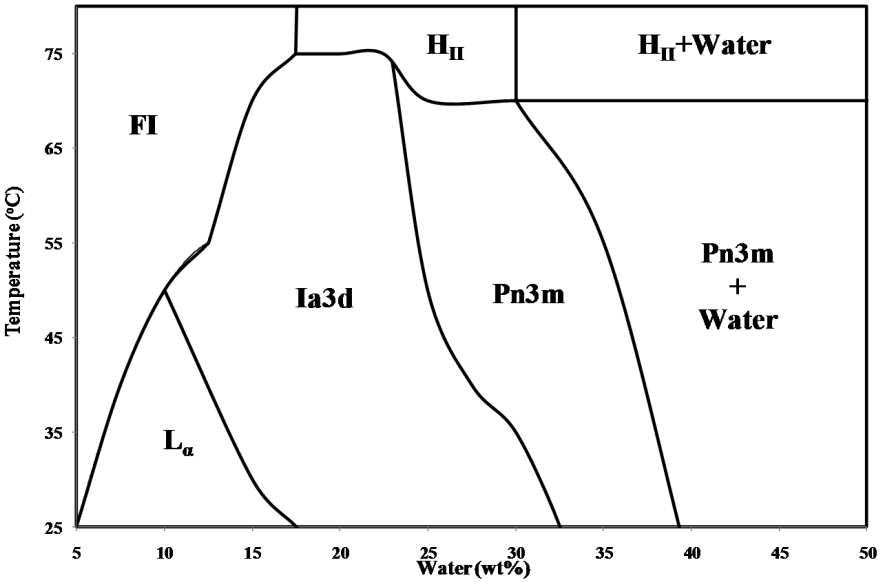

Figure 2.2: Phase diagram of the Dimodan U/J (monolinolein) water system obtained from polarized optical microscopy and SAXS. The lines separating the $Ia3d$ and $Pn3m$ were obtained from SAXS.

previous literature and the cubic phase appears in a larger window in the phase diagram.

The pure L_α phase exists approximately between 5% and 17.5% water at 25°C and is found to have a triangular-like shape. At 45°C the lamellar phase melts into the isotropic fluid phase for 10% (w/w) water. Bicontinuous cubic phases are observed at higher water contents and they are identified as gyroid ($Ia3d$) and double diamond ($Pn3m$). The $Ia3d$ spans a large area between 17.5% and 32.5% (w/w) of water at 25°C. $Ia3d$ and H_{II} coexist at 73°C and 20% water. Both $Pn3m$ and H_{II} have a large region of coexistence with excess water at higher water concentration as shown in the phase diagram. The boundary between the $Pn3m$ and $Pn3m$+water is identified by the evaluation of the lattice parameter, which increases with concentration of water in the bulk $Pn3m$, levels off to a maximum value and plateaus in the $Pn3m$+water. Similar analysis is also followed for the H_{II} phase to resolve the onset of the region of coexistence with water. The H_{II} phase melts into the isotropic fluid (FI) phase at 95°C as per the reported phase

diagram[46] but in the present work we have limited the experimental temperature window only up to 80°C.

2.3.2 Bicontinuous Cubic Phase in Presence of Silica Nanoparticles

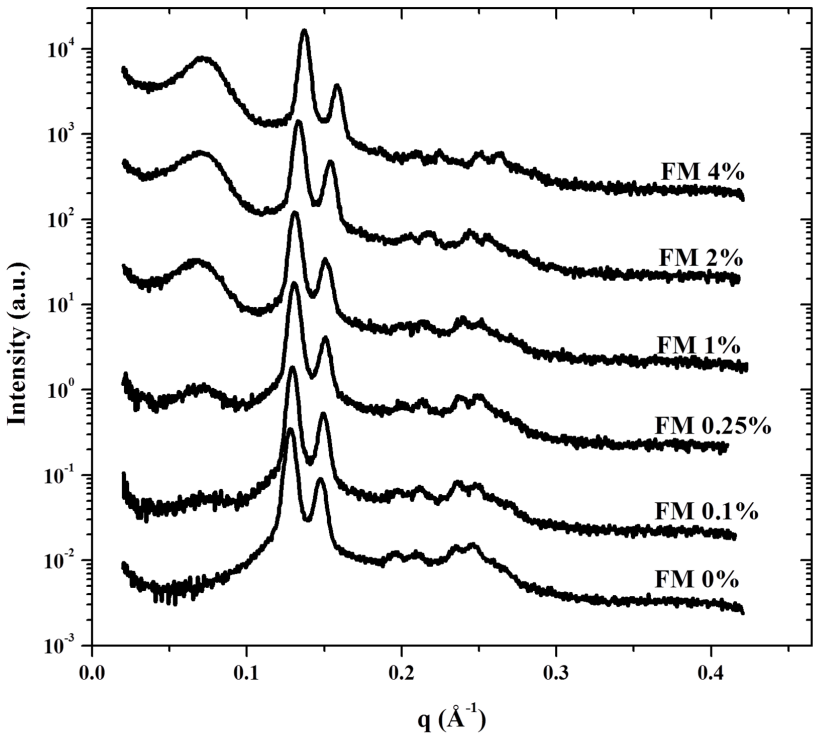

Figure 2.3: SAXS patterns for the bicontinuous cubic phase $Ia3d$ (lipid 75%−water 25%) at 30°C for colloidal silica concentration of $0\%, 0.1\%, 0.25\%, 1\%, 2\%$ and 4%. The $Ia3d$ phase is identified by indexing the peaks at $\sqrt{6}$, $\sqrt{8}$, $\sqrt{14}$, $\sqrt{16}$, $\sqrt{20}$, $\sqrt{22}$ and $\sqrt{24}$. The structure factor peak arising at $q = 0.06989\text{Å}^{-1}$ indicates neighboring nanoparticles correlations.

The cubic phase consists of a lipidic bilayer following periodic minimal surfaces which separates two water channel networks.[49] As shown in the phase diagram (Fig-

ure 2.2), there are two types of bicontinuous cubic phases, gyroid ($Ia3d$) and double diamond ($Pn3m$). The bicontinuous cubic phase $Ia3d$ is identified by the peak positions at Bragg values $\sqrt{6}$, $\sqrt{8}$, $\sqrt{14}$, $\sqrt{16}$, $\sqrt{20}$, $\sqrt{22}$ and $\sqrt{24}$ which are indexed as $hkl = (211), (220), (321), (400), (420), (332)$ and (422). The $Pn3m$ phase is having a Bragg reflection series of $\sqrt{2}$, $\sqrt{3}$, $\sqrt{4}$, $\sqrt{6}$, $\sqrt{8}$, $\sqrt{9}$ and $\sqrt{10}$ which can be indexed as $hkl = (110), (111), (200), (211), (220), (221$ and $300)$ and (310). The lattice parameter is calculated from the SAXS. We employ the method of triply periodic minimal surfaces (TPMS)[50,51] to extract the radius of the water channels.[46] From the lipid-water phase diagram, we choose composition as 25%(w/w) water and 30°C for $Ia3d$ and 35%(w/w) water and 30°C for $Pn3m$. In all the experiments we maintain the surfactant-water ratio constant for each phase, i.e. $75:25$ for $Ia3d$ and $65:35$ for $Pn3m$.

For lower concentrations of particles (0.1%(w/w)) the Braggs peak shifts higher q, indicating a decrease in the lattice parameter as shown in Figure 2.3. The lattice parameter calculated from the SAXS pattern (as described in the experimental section) as a function of particle concentration is plotted in Figure 2.4. From the figure it is clear that there is a sharp drop in lattice parameter at low particle concentrations and then lattice parameter decreases continuously with particle concentration. At the same time, a structure factor peak at a q value 0.0699Å^{-1} can be observed corresponding to a length scale of 9nm, nearly identical to the typical correlation distance expected for closely interacting nanoparticles. The intensity of structure factor increases with particle concentration, whereas the position of the particle structure factor peak does not shift with particle concentration. The systematic decrease in lattice parameter strongly suggests that the nanoparticles cannot be accommodated within the water channels and macrophase separate within the $Ia3d$ mesophase.

The scenario can be interpreted as follows. When the colloidal nanoparticles are embedded within the mesophase, the mismatch between the particles diameter (8nm) and

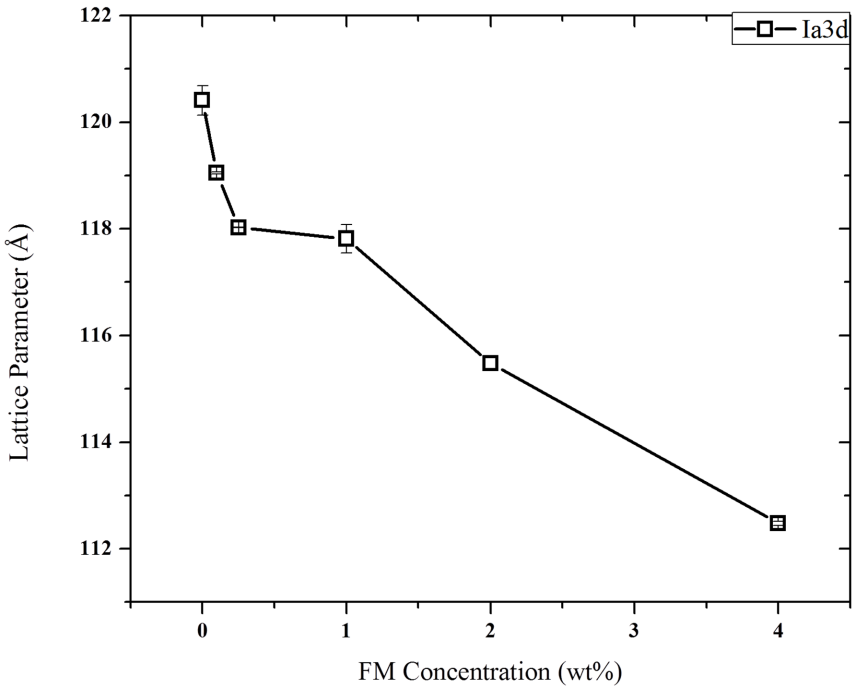

Figure 2.4: The lattice parameter obtained from the peak positions of the bicontinuous cubic phase $Ia3d$ as a function of silica concentration.

the water channel diameter (3nm for $Ia3d$ and 3.8nm for $Pn3m$) prevents the particles from being incorporated within the water channels leading to macrophase separation. The decrease in lattice parameter likely results from the dehydration of the bound water from the polar lipid heads, which is needed to rehydrate the clusters of macrophase separated hydrophilic nanoparticles. This results in a sharp drop in lattice parameter at low particle concentrations. This mechanism then bears direct analogies with the dehydration of cubic phases observed during the in-meso crystallization of proteins, in which the protein crystals–the analogues of the macrophase separating nanoparticles clusters–have been shown to act as "water pumps" dehydrating the water channels of the cubic phases.[52]

We consider now the case of the double diamond bicontinuous cubic phase space group

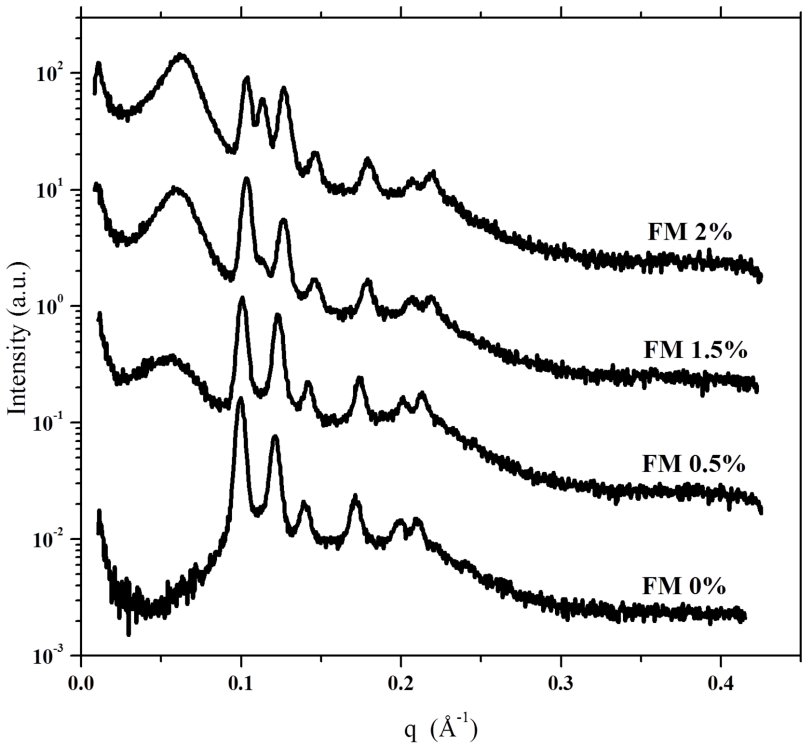

Figure 2.5: The SAXS pattern of $Pn3m$ (lipid 65%− water 35% at 30°C) for different colloidal silica concentrations. The structure factor peak arising at $q = 0.0699$Å^{-1} indicates neighboring nanoparticles correlations. Starting from 1.5% of silica concentration, a new peak appears as highlighted by the black arrows, indicating the coexistence of $Pn3m$ and $Ia3d$ phases.

$Pn3m$. Figure 2.5 shows the SAXS profile for the $Pn3m$ phase with the addition of colloidal particles. For the mesophase without the particles (lipid water), the first peak of the $Pn3m$ appears at a q value of 0.099Å^{-1} corresponding to a lattice parameter of 89.8Å. The peak shifts to 0.1Å^{-1} upon the addition of 0.5%(w/w) nanoparticles giving a lattice parameter value of 88.1Å. Similarly the second Bragg peak, which for the pure $Pn3m$ phase positioned at 0.121Å^{-1}, shifts to 0.123Å^{-1} on the addition of 0.5% nanoparticles. On increasing the loading of colloidal particles into the mesophase, the peaks shift further to higher q values while a low q broad peak corresponding to nanoparticles–nanoparticles

correlation appears. The lattice parameter calculated from the SAXS curve is plotted as function of colloidal concentration in Figure 2.6 showing a decrease in the lattice parameter as the colloidal concentration increases. At a nanoparticle loading of $\phi = 1.5\%(w/w)$, we can see the emergence of a new peak at a q value of 0.113Å^{-1} between the first and second peak of $Pn3m$ and this becomes dominant for $\phi = 2\%(w/w)$. This peak can be attributed to the first peak of a $Ia3d$ inverted bicontinuous cubic phase coexisting with the $Pn3m$, and is a result of partial dehydration of the water channels by the macrophase separating clusters of nanoparticles. These findings accord with literature reports of the appearance of an $Ia3d$ phase when lysozyme proteins are crystallized in-meso from a bulk $Pn3m$, and once more, this supports a direct analogy between the thermodynamics of the aggregating hydrophilic nanoparticles and the in-meso crystallizing protein clusters.[36,52]

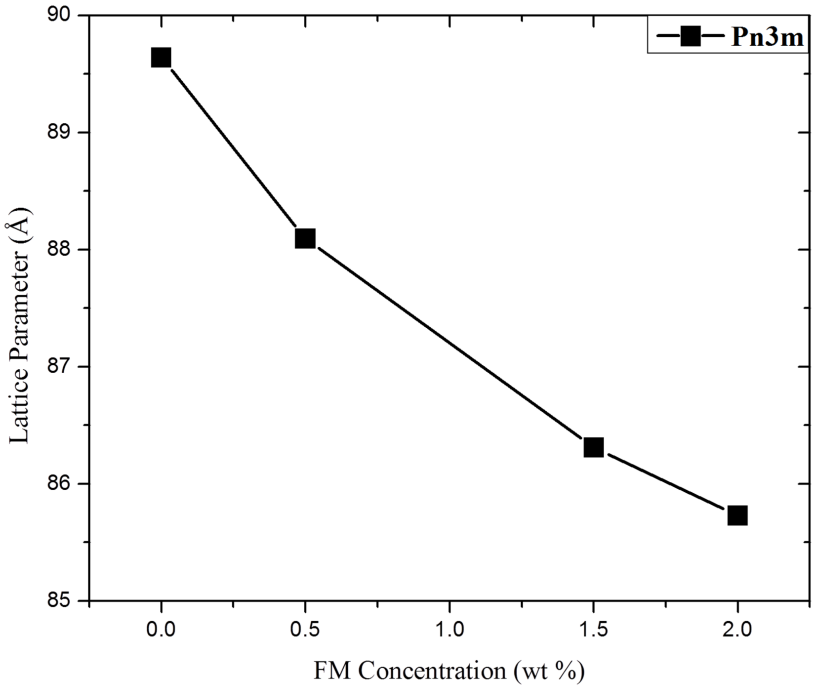

Figure 2.6: The lattice parameter of the $Pn3m$ phase as a function of silica concentration.

The effect of nanoparticle concentration on the order-order transition temperature for

the phase $Ia3d$ is shown in Figure 2.7. The $Ia3d$–H_{II} order–order transition temperature decreases as the particle concentration ϕ increases in a rather remarkable way, with a drop as high as 20°C when the colloid concentration reaches $3\%(w/w)$, leading to a final transition temperature of 50°C. This shift is again consistent with the observed dehydration of the monoglyceride polar heads caused by the aggregating macro–separating clusters of nanoparticles, which results in a systematic decrease of the packing parameter and a stabilization of inverted mesophases with enhanced curvature such as the reverse hexagonal. But unlike the lattice parameter, the transition temperature does not show a sharp decrease in value at very low nanoparticle concentrations.

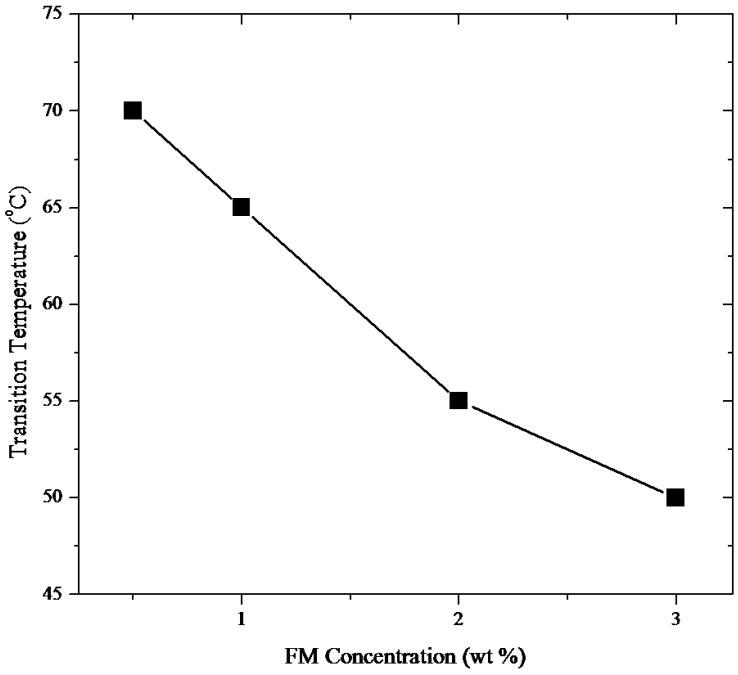

Figure 2.7: The variation of $Ia3d$ H_{II} order order transition temperature as a function of silica concentration.

2.3.3 Inverse Hexagonal Phase H_{II} in Presence of Silica Nanoparticles

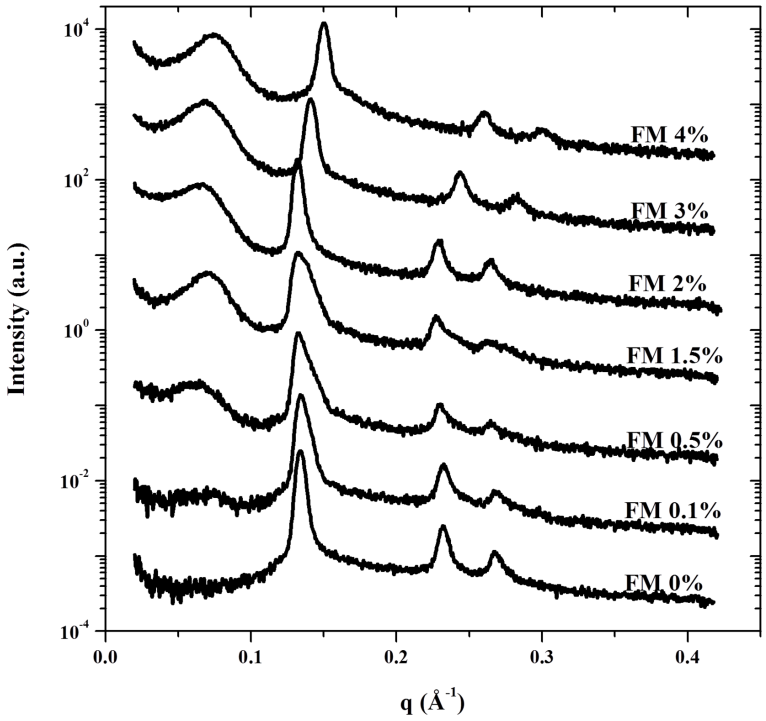

Figure 2.8: SAXS profiles of the inverse hexagonal phase H_{II} (lipid 75%− water 25% at 75°C) with different nanoparticle concentrations. The peak positions shift with particle concentrations. There is a structure factor peak developing upon increasing concentration at a q value of 0.0745Å^{-1}.

This section describes the structural properties of the inverse hexagonal mesophase upon the addition of silica nanoparticles. The lipid-water system forms inverse hexagonal phase at higher temperatures as shown in the phase diagram. The cubic phase $Ia3d$ coexists with the inverse hexagonal phase H_{II} at 70°C. The composition selected for the study is a lipid:water system in the ratio of 75 : 25 at a temperature of 75°C. At these conditions, the SAXS profile shows three peaks at q positions in the ratio of $\sqrt{1} : \sqrt{3} : \sqrt{4}$,

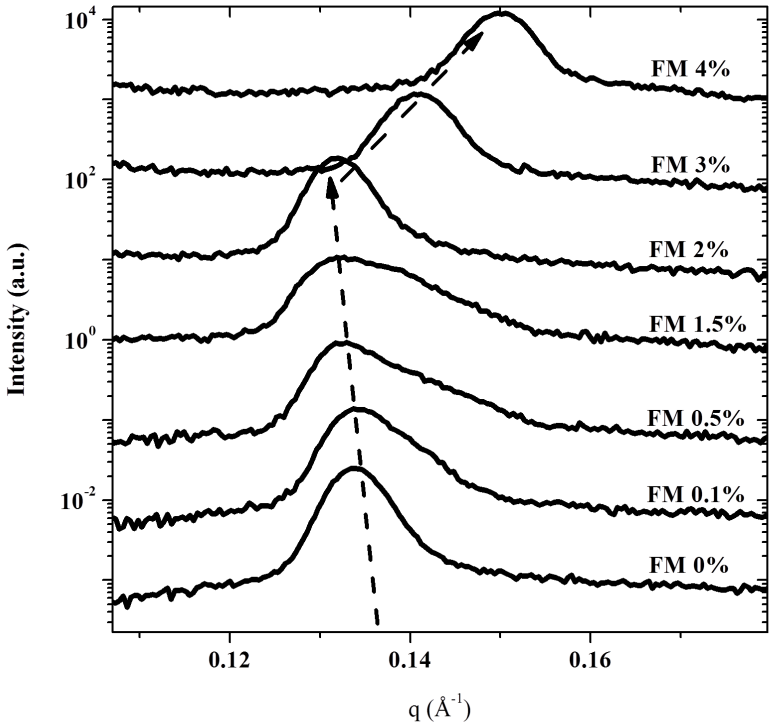

Figure 2.9: A close-up of the first Bragg peak of the SAXS pattern of the hexagonal phase. We can see that the first Bragg reflection initially shifts to lower q values up to a threshold concentration and then inverts the tendency moving toward higher q values. The dotted arrow indicates the path of the shift on the Bragg reflection.

showing a single H_{II} phase (Figure 2.8). The H_{II} phase maintains the same symmetry after the nanoparticles are incorporated. This is evident from the SAXS profile as shown in Figure 2.8, where the q values of the peaks maintains the same ratio, although some structural changes are evidenced by the broadening of all the peaks starting from loading of 0.5% nanoparticles. The evolution on the position of peaks, however, follows a non-trivial trend in this case, as shown by a close look at the primary Bragg peak of the H_{II} phase versus nanoparticles concentration (Figure 2.9). We can see that the first Bragg reflection initially shifts to lower values of q up to a colloidal concentration of 2%, and then it shifts to higher q values for higher colloidal concentration. The q value for the

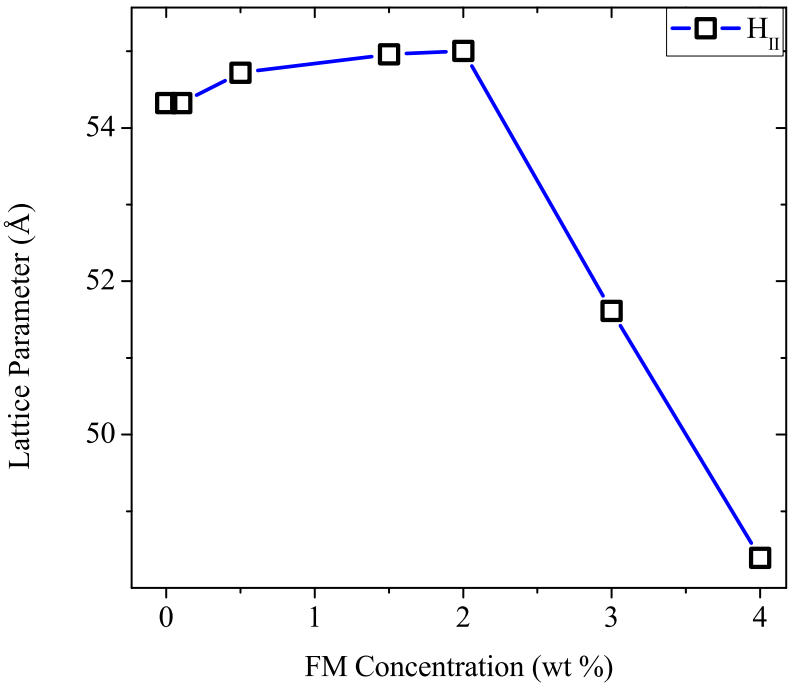

Figure 2.10: The lattice parameter obtained from the position of the Bragg peaks of the hexagonal phase plotted against the colloidal silica concentration.

first Bragg peak of the neat H_{II} phase is 0.134Å^{-1} giving a lattice parameter of 54.3Å. When a colloidal nanoparticle concentration of $\phi = 0.5\%(w/w)$ is added, the q value of the primary peak shifts to 0.133Å^{-1} ($a = 54.7$Å). As the concentration of the colloids increases, the lattice parameter increases further and reaches a maximum at $\phi = 2\%(w/w)$ with a value of 55.0Å. Although these changes are small, they are systematic, above the uncertainty of the SAXS (± 0.5Å) and reproducible (in triplicate measurements). Further addition of colloids into the mesophase, however causes the lattice parameter to decrease sharply. The lattice parameter evolution with silica concentration as a function of nanoparticles concentration is summarized in Figure 2.10. The SAXS profile in Figure 2.8 shows some additional features for the H_{II}-nanoparticles blends at lower q values. At $\phi = 0.1\%$, a new peak appear at $q = 0.0745\text{Å}^{-1}$, which become stronger as the

concentration of the silica particle increases. The d spacing for this peak corresponds again to the average particle size (8.4nm) indicating close–particle correlations.

Interpretation of the non–monotonic evolution of the lattice parameter for the inverse hexagonal phase will be attempted below.

2.3.4 Lyotropic Lamellar Phase L_α in Presence of Silica Nanoparticles

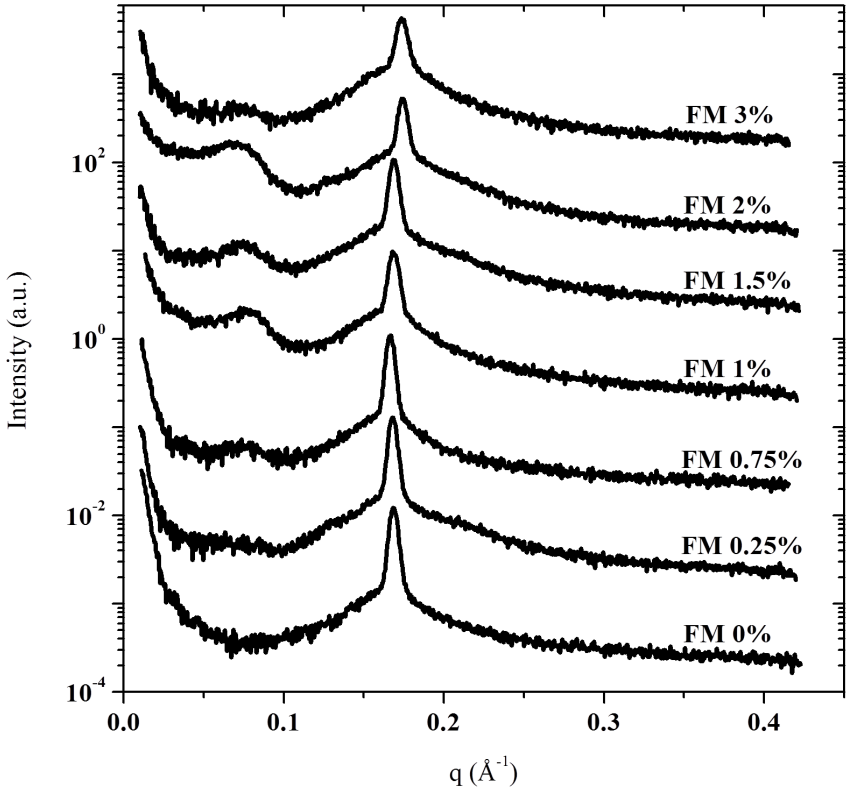

Figure 2.11: The SAXS profiles of lamellar phase L_α (lipid 90%–water 10%) as a function of nanoparticles concentration. A structure factor corresponding to the nanoparticle–nanoparticle correlations appears at $q = 0.06989\text{Å}^{-1}$ upon increasing concentration of nanoparticles.

Here we describe the effect of silica nanoparticles on the structural properties of the lyotropic lamellar phase formed by 10% water at 30°C. The SAXS profile for the lyotropic lamellar phase with nanoparticle inclusions is shown in Figure 2.11. The first Braggs peak in the system without silica particles appears at a q value of 0.168Å^{-1} giving a lattice parameter of 37.3Å. As the silica nanoparticles are added to the system in a concentration of $\phi = 0.25\%(w/w)$, the first Bragg reflection initially shifts to the lower q value 0.168Å^{-1} indicating the swelling of the mesophase. At $\phi = 0.75\%(w/w)$, the peak shifts further to a lower q value 0.166Å^{-1} giving a lattice parameter of 37.76Å. Further increase in concentration of silica particles beyond this causes an inversion of tendency and the peak shift towards higher q leading to a shrinking effect. A close-up on the position of the first Bragg reflection is given in Figure 2.12, while Figure 2.13 shows the change in lattice parameter with the silica nanoparticles concentration. The changes are minimal, but do not follow a monotonic trend. This behavior is thus similar to the one observed in the inverse hexagonal phase H_{II} but different from that of the bicontinuous cubic phases $Ia3d$ and $Pn3m$.

Interpretation of the non–monotonic evolution of the lattice parameter for the hexagonal and lamellar phase can be attempted based on the energy description of a bilayer membrane given by Helfrich.[1,53] This energy consists of two terms: a term accounting for the bending and the other for the compression of the bilayer interface with bending elastic constant K and elastic constant of compression $\overline{B}$, leading to the following energy density:

$$F = \frac{1}{2}K\left(\frac{1}{R_1} + \frac{1}{R_2}\right)^2 + \frac{1}{2}\overline{B}\left(\frac{\Delta d}{d}\right)^2 \tag{2.1}$$

where R_1 and R_2 are the curvatures of the membrane and d is the bilayer periodicity. The elastic constants can be calculated from the mean bending elastic modulus[22] κ by

$$\overline{B} = \frac{9\pi}{64}\frac{(k_B T)^2}{\kappa}\frac{d}{(d-\delta)^4} \tag{2.2}$$

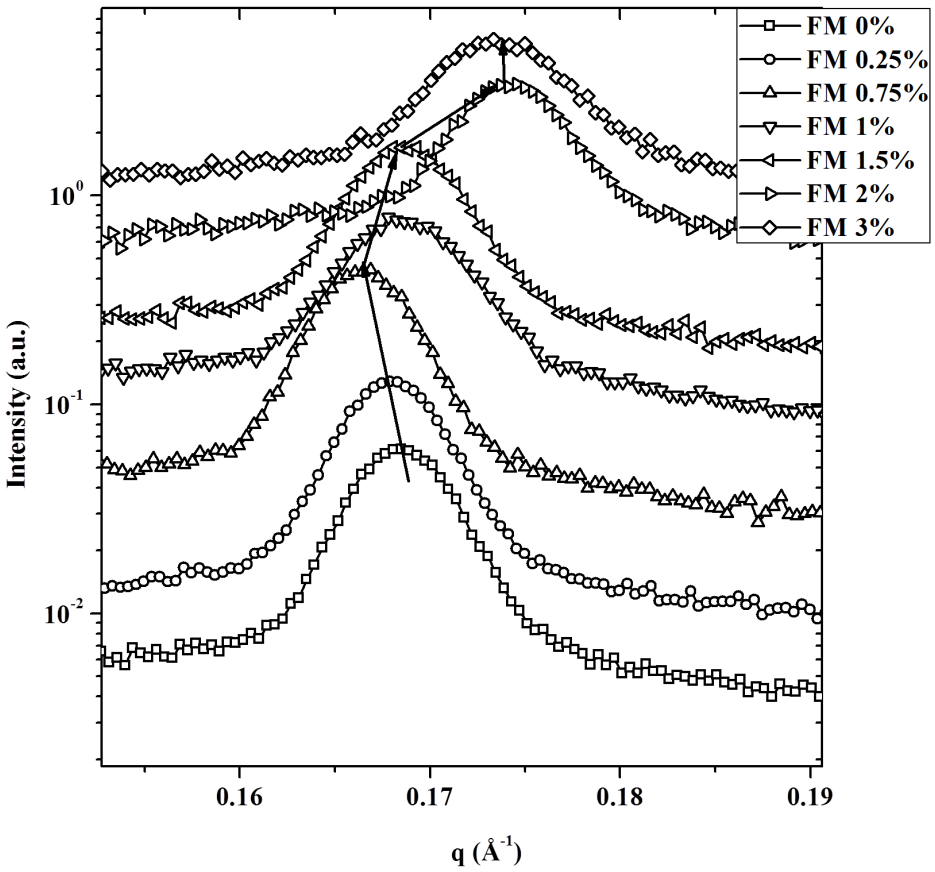

Figure 2.12: The first Bragg peak for the lamellar phase L_α as a function of nanoparticles concentrations at 0%, 0.25%, 0.75%, 1%, 1.5%, 2% and 3% nanoparticles.

and

$$K = \frac{\kappa}{d} \tag{2.3}$$

with δ being the membrane thickness. A quick calculation of the deformation energy associated with the penetration of a nanoparticle inside the hydrophilic domains of the lipid bilayers can be performed by integrating eqn 2.1 around the volume of a single particle and taking κ in the range of 1 to $10k_BT$. This reveals that the energy penalty for this migration is too high ($> 100k_BT$) to justify such a partitioning when the nanopar-

ticles greatly exceeds the water bilayer thickness as in the present case. It has however been shown previously that Helfrich theory fails to interpret correctly the features of nanoparticles–lyotropic systems, such as in the case of ferrosmectic materials.[20,22] The liquid crystalline phase get disturbed as nanoparticles are added to the system. The peak broadening is a measure of the degree of order. At low nanoparticle concentrations, the nanoparticles get confined within the water channels of the hexagonal phase and result in a disturbance of periodic order. The broadening increases with increase in nanoparticle loading up to a threshold concentration and after which, a macroscopic phase separation takes place thus sharpening the Bragg reflection peaks. We are then left over with this puzzling non–monotonic evolution of the lattice parameter for hexagonal and lamellar phases in presence of hydrophilic (large) nanoparticles. Terentjev proposed a theoretical model for the structure changes of the Smectics A lamellar phase based on the condensation of point defects.[43] In his model, it is proposed that the impurities creating point defects are mutually attractive and can act as nucleating agents for a new phase, for example a macrophase separating cluster of impurities. This explanation seems to support to some extent the findings observed in the present work for the lamellar (and hexagonal) phase, where to an initial regime corresponding to an increase in lattice parameter a second regime follows after which a macroscopic phase separation takes place. Alternatively, the role of nanoparticles in suppressing the bilayer fluctuations might also have a role. The second regime is revealed by the dehydration of the hydrophilic domains (e.g. corresponding decrease in lattice parameter) resulting from the "pumping out" effect of the hydrophilic macrophase separated clusters. The removal of water from the hydrophilic domains is generated by the re–equilibration of the water chemical potential of the water between the newly formed phase (clusters) and the water layers in the lamellar phase, and again is analogous to what observed during in–meso crystallization of proteins.[52]

That the presence of nanoparticles in the lamellar phase follows two completely differ-

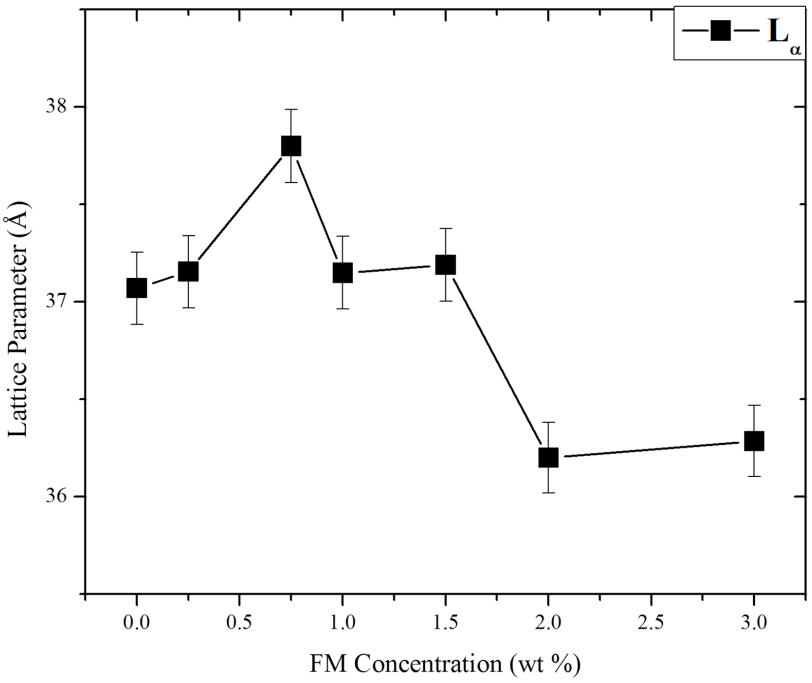

Figure 2.13: The lattice parameter of the lamellar phase L_α calculated from the position of the Bragg peak in SAXS plotted as a function of nanoparticles concentration.

ent structural trends depending on the concentration regime, is perhaps shown even more unambiguously by the changes in the order–disorder transition temperature (T_{ODT}) upon increase in colloidal nanoparticles concentration. Figure 2.14 shows a typical example of the evolution of the T_{ODT} at 10% w/w water for the mesophase L_α. In the swelling regime of the concentration, the T_{ODT} is enhanced by as much as 10°C, which witnesses a stabilization of the lamellar phases and demonstrates unambiguously an important structural role of the nanoparticles in this concentration regime. However, as soon as the nanoparticle concentration is above the threshold concentration for macrophase separation, the T_{ODT} declines rapidly, as a consequence of the loss of water stabilizing the lamellar mesophase.

Since the macrophase separation is accompanied by the removal of some water from

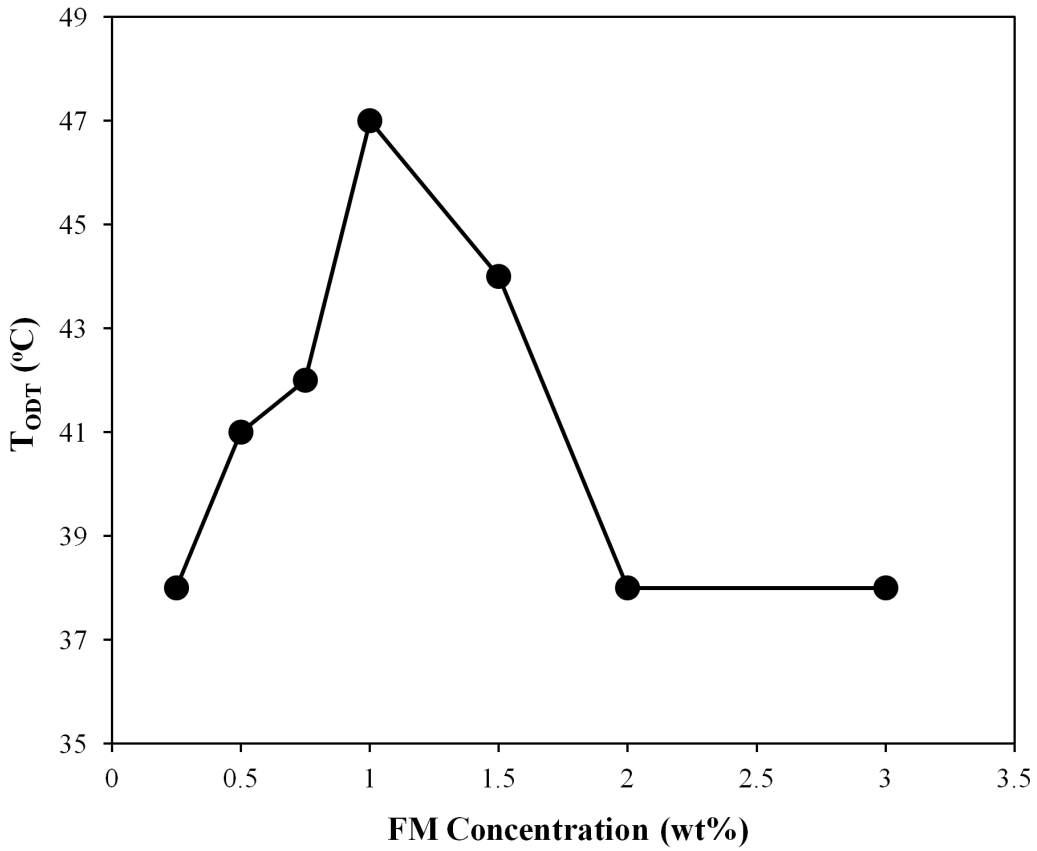

Figure 2.14: The order-disorder transition temperature (T_{ODT}) of the lamellar phase plotted as a function of the colloidal nanoparticles concentration.

the water channels as a consequence of the rehydration of the hydrophilic nanoparticles clusters, the surfactant molecules also exhibit an increased tendency to crystallize. This effect is evident from the differential scanning calorimetry thermograms shown in Figure 2.15. The mesophases are scanned for a temperature range from 40°C to 60°C at a rate of 10°C/min. The L_α phase with colloidal silica concentrations 0.75% (w/w) and 1.5% (w/w) is compared with that of the pure phase. For the neat lamellar mesophase, the peak corresponding to the melting of the lipid tails can be identified as the broad peak centered at ca 3°C. Upon the addition of silica nanoparticles, this peak gains progressively in intensity at 0.75% (w/w) and 1.5% (w/w), indicating an increased tendency to crystallize upon increased silica content.

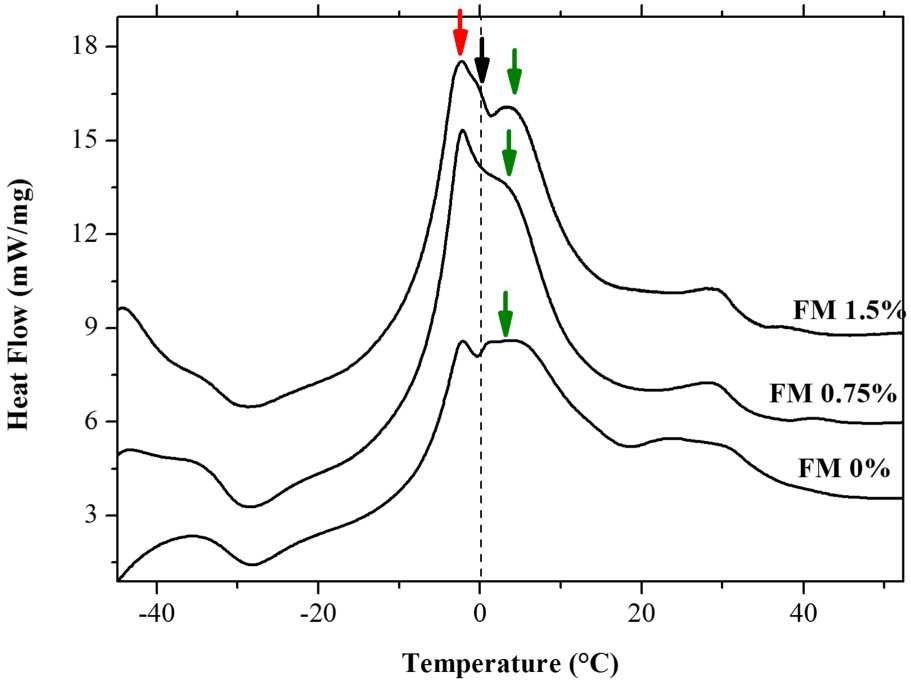

Figure 2.15: The DSC thermograms for the lamellar phase L_α in presence of different concentrations of the colloidal nanoparticles. The green arrow shows the peak corresponding to the melting of the tails of the surfactant. The red arrow shows the peak position of the melting of the hydrogen–bonded water in the sample. The dashed line at 0°C and the black arrow indicate the melting of free, unbound water.

More importantly, careful analysis on the transitions occurring at temperatures 0°C, allows distinguishing between the melting of the bound and free water. Indeed, a comparison between the peaks of the melting of water reveals considerable differences and two types of water present. The free water, the water which has the bulk water properties melts at 0°C while the interphasal water, which is the water bound to the hydrophilic heads of the lipids via hydrogen bonds, melts at subzero temperatures in the range $\sim -10°\text{C} < T < 0°\text{C}$, as described in the work of Garti and colleagues.[54] As seen from Figure 2.15, in the case of the lamellar phase, there is only one peak corresponding to water, e.g. a subzero peak centered at −2.5°C, indicating that all the water is bound by hydrogen bonding to the monoglyceride polar heads at these conditions. This is consis-

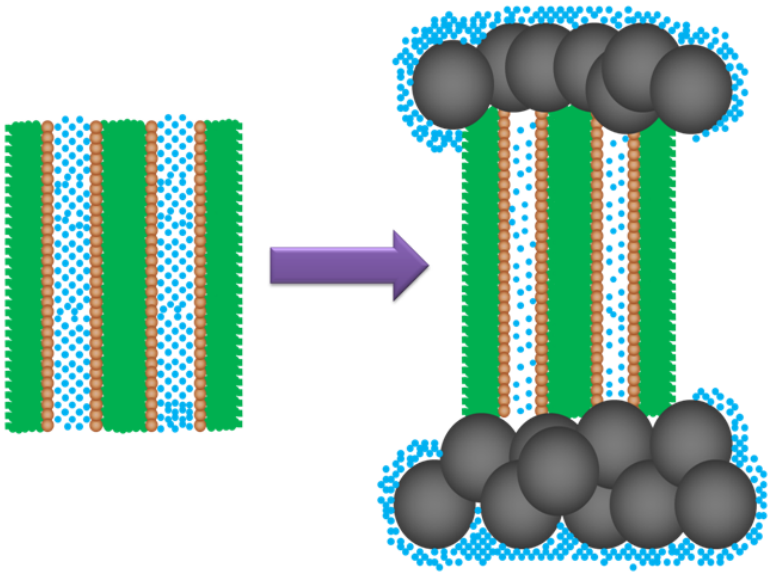

Figure 2.16: The schematic represent the pumping out mechanism of water with the phase separation of the colloidal particles. The green section indicates the hydrophobic tails of the lipids and the brown circles are the hydrophilic head part of the lipids. The blue dots indicates the water molecules which are concentrated near the head groups of the lipids. Big dark grey circles are nanoparticles, which are phase separated. The left side figure shows that the water molecules are mostly inside the liquid crystalline structures. As the nanoparticles get phase separated, some of the water molecules, which were initially at the lipid bilayers, migrate along with the nanoparticles thus reducing the water concentration between the lipid bilayers.

tent with theoretical predictions by Lee et al..[9] At 0.75% (w/w) silica, when there is no evidence yet of a macroscopic phase separation of the nanoparticles, the subzero peak centered at -2.5°C is still the only peak that corresponds to water, indicating that the great majority of water is still in the bound state. The situation is different when the particle loading is increased to 1.5% (w/w), where in addition to the interphasal water peak an additional shoulder peak appears at 0°C, indicating the presence of free water. At these conditions, macrophase separation of silica particles takes place and the free water corresponds to the water migrated from the hydrophilic layers (where it is prevalently h–bonded) to the hydrophilic nanoparticles clusters. Indeed, water is driven into these hydrophilic clusters to primarily reduce the electrostatic chemical potential of the charged silica nanoparticles, which should leave water prevalently in the free, unbound state. This

provides, once more, compelling experimental evidence that the physical interaction of hydrophilic nanoparticles with the lamellar phase follows two different physical behaviors depending on the concentration regime considered. While energy considerations based on Helfrich theory tend to rule out penetration of nanoparticles within the hydrophilic layers, lattice parameter, order disorder transition temperature and thermodynamic status of the bound/unbound water, all point towards a specific interaction mechanism of the nanoparticles with the membrane in the low concentration regime, whose exact nature remains to be determined. Also, we speculate the same behaviour of water is responsible for the anomalous behaviour of lattice parameter of the bicontinuous cubic phases.

At this stage, it also remains unclear and highly unexpected why the blending of nanoparticles in the bicontinuous cubic phases does not follow the same trends as in the hexagonal and lamellar phase, especially because in bicontinuous cubic phase, the mismatch between the water channels and the nanoparticles is smaller than in the case of the hexagonal and lamellar phase. It has to be hoped that future work will bring further insight into these intriguing experimental findings.

2.4 Conclusions

We have systematically investigated the effect of varying concentrations of colloidal nanoparticles of size slightly exceeding that of the water domains in different types of liquid crystalline phases. At high concentration, the colloidal silica nanoparticles are found to macrophase separate in the bicontinuous cubic phases of $Ia3d$ and $Pn3m$ simmetries, as indicated by a monotonous decrease of the lattice parameter as a function of the concentration of the nanoparticles. The systematic decrease of the lattice parameter upon increase in nanoparticles concentration is interpreted with the formation of hydrophilic clusters of nanoparticles, macrophase separating and de–hydrating the bound water of the bicontinuous water channels. The behavior was different in the case of hexagonal and

lamellar phases, in which the lattice parameter increased up to a maximum value, and once reached a critical threshold concentration, started again to decreases sharply. Further experimental observations on the interactions between nanoparticles and lamellar phase is provided by the analysis of order disorder transition temperature and free and interphasal water of the lamellar mesophase in presence of nanoparticles, as observed by SAXS and DSC, respectively. The order disorder transition temperature of the lamellar phase increases by 10°C with nanoparticles content and then rapidly decreases beyond a threshold concentration. DSC analysis suggests that, while in the absence of nanoparticles all the water present in the water present in the lamellar phase appears to be bound to the lipid polar heads via hydrogen bonding, as soon as the concentration of the nanoparticles beyond the macrophase separation threshold is reached, presence of free water becomes detectable, inferring migration of water from the lamellar layers to nanoparticles hydrophilic clusters. Although the calculated Helfrich free energy appears too high to justify penetration of nanoparticles within the hydrophilic layers, our experimental results infer a specific interaction mechanism of the nanoparticles with the membrane in the low concentration regime. The present findings provide further experimental analyses on the complex phase behavior of lyotropic liquid crystals in presence of nanoparticles and open new questions on the influence of mesophase symmetry on the partitioning and phase separation of the guest colloidal species.

References

[1] deGennes, P. G. *The Physics of Liquid Crystals*; Oxford University Press: Oxford, England, 1974.

[2] Mezzenga, R.; Schurtenberger, P.; Burbidge, A.; Michel, M. *Nat. Mater.* **2005**, *4*, 729–740.

[3] Israelachvili, J. N. *Intermolecular and Surface Forces*, 2nd ed.; Academic Press Limited: London, 1992.

[4] Ganem-Quintanar, A.; Quintanar-Guerrero, D.; Buri, P. *Drug Dev. Ind. Pharm.* **2000**, *26*, 809–820.

[5] Amar-Yuli, I.; Libster, D.; Aserin, A.; Garti, N. *Curr. Opin. Colloid Interface Sci.* **2009**, *14*, 21–32.

[6] Ubbink, J.; Burbidge, A.; Mezzenga, R. *Soft Matter* **2008**, *4*, 1569–1581.

[7] Sagalowicz, L.; Mezzenga, R.; Leser, M. E. *Curr. Opin. Colloid Interface Sci.* **2006**, *11*, 224–229.

[8] Garti, N.; Amar-Yuli, I.; Spernath, A.; Hoffman, R. E. *Phys. Chem. Chem. Phys.* **2004**, *6*, 2968–2976.

[9] Lee, W. B.; Mezzenga, R.; Fredrickson, G. H. *Phys. Rev. Lett.* **2007**, *99*, 187801.

[10] Lee, W. B.; Mezzenga, R.; Fredrickson, G. H. *J. Chem. Phys.* **2008**, *128*, 074504–.

[11] Vrij, A. *Pure Appl. Chem.* **1976**, *48*, 471–483.

[12] Asakura, S.; Oosawa, F. *J. Chem. Phys.* **1954**, *22*, 1255.

[13] Salamat, G.; Kaler, E. W. *Langmuir* **1999**, *15*, 5414–5421.

[14] Antonietti, M.; Conrad, J.; Thuenemann, A. *Macromolecules* **1994**, *27*, 6007–6011, doi: 10.1021/ma00099a011.

[15] Safinya, C. R.; Roux, D.; Smith, G. S.; Sinha, S. K.; Dimon, P.; Clark, N. A.; Bellocq, A. M. *Phys. Rev. Lett.* **1986**, *57*, 2718–2721.

[16] Ramos, L.; Fabre, P.; Dubois, E. *J. Phys. Chem.* **1996**, *100*, 4533–4537.

[17] Fabre, P.; Quilliet, C.; Veyssie, M.; Nallet, F.; Roux, D.; Cabuil, V.; Massart, R. *Europhys. Lett.* **1992**, *20*, 229–234.

[18] Suganuma, Y.; Imai, M.; Nakaya, K. *J. Appl. Cryst.* **2007**, *40*, s303–s306.

[19] Suganuma, Y.; Urakami, N.; Mawatari, R.; Komura, S.; Nakaya-Yaegashi, K.; Imai, M. *J. Chem. Phys.* **2008**, *129*, 134903–10.

[20] Ponsinet, V.; Fabre, P. *J. Phys. Chem.* **1996**, *100*, 5035 – 5038.

[21] Bouglet, G.; Ligoure, C.; Bellocq, A. M.; Dufourc, E.; Mosser, G. *Phys. Rev. E* **1998**, *57*, 834 – 842.

[22] Ponsinet, V.; Fabre, P. *J. Phys. II France* **1996**, *6*, 955 – 960.

[23] Fabre, P.; Casagrande, C.; Veyssie, M. *Phys. Rev. Lett.* **1990**, *64*, 539 – 542.

[24] Quilliet, C.; Fabre, P.; Cabuil, V. *J. Phys. Chem.* **1993**, *97*, 287–289, doi: 10.1021/j100104a004.

[25] Ponsinet, V.; et al., *Europhys. Lett.* **1995**, *30*, 277.

[26] Castro-Roman, F.; Porte, G.; Ligoure, C. *Phys. Rev. Lett.* **1999**, *82*, 109–112.

[27] Kimura, Y.; Mori, T.; Yamamotto, A.; Mizuno, D. *J. Phys.:Condens.Matter* **2005**, *17*, S2937–S2942.

[28] Loudet, J.-C.; Barois, P.; Paulin, P. *Nature* **2000**, *407*, 611–613.

[29] Loudet, J. C.; Barois, P.; Auroy, P.; Keller, P.; Richard, H.; Paulin, P. *Langmuir* **2004**, *20*, 11336–11347.

[30] Koehler, R. D.; Kaler, E. W. *Langmuir* **1997**, *13*, 2463–2470, doi: 10.1021/la960552o.

[31] Sharma, K. P.; Kumaraswamy, G.; Ly, I.; Mondain-Monval, O. *J. Phys. Chem. B* **2009**, *113*, 3423–3430.

[32] Zapotocky, M.; Ramos, L.; Poulin, P.; Lubensky, T. C.; Weitz, D. A. *Science* **1999**, *283*, 209–212.

[33] Basappa, G.; Suneel,; Kumaran, V.; Nott, P. R.; Ramaswamy, S.; Naik, V. M.; Rout, D. *Eur. Phys. J. B* **1999**, *12*, 269–276.

[34] Beneut, K.; Constantin, D.; Davidson, P.; Dessombz, A.; Chaneac, C. *Langmuir* **2008**, *24*, 8205–8209, doi: 10.1021/la800387a.

[35] Constantin, D.; Davidson, P.; Chaneac, C. *Langmuir* **2010**, *26*, 4586–4589, doi: 10.1021/la100045r.

[36] Angelov, B.; Angelova, A.; Papahadjopoulos-Sternberg, B.; Lesieur, S.; Sadoc, J.-F.; Ollivon, M.; Couvreur, P. *J. Am. Chem. Soc.* **2006**, *128*, 5813–5817, doi: 10.1021/ja060082c.

[37] Angelova, A.; Angelov, B.; Mutafchieva, R.; Lesieur, S.; Couvreur, P. *Acc. Chem. Res.* **2011**, *44*, 147–156, doi: 10.1021/ar100120v.

[38] Angelova, A.; Angelov, B.; Papahadjopoulos-Sternberg, B.; Bourgaux, C.; Couvreur, P. *J. Phys. Chem. B* **2005**, *109*, 3089–3093, doi: 10.1021/jp044216p.

[39] Angelova, A.; Angelov, B.; Papahadjopoulos-Sternberg, B.; Ollivon, M.; Bourgaux, C. *Langmuir* **2005**, *21*, 4138–4143, doi: 10.1021/la047745t.

[40] Angelova, A.; Ollivon, M.; Campitelli, A.; Bourgaux, C. *Langmuir* **2003**, *19*, 6928–6935, doi: 10.1021/la0345284.

[41] Ligoure, C.; Bouglet, G.; Porte, G.; Diat, O. *J. Phys. II France* **1997**, *7*, 473–491.

[42] Porcar, L.; Ligoure, C.; Marignan, J. *J. Phys. II France* **1997**, *7*, 493–501.

[43] Terentjev, E. M. *Sov. Phys. - Crystallography* **1986**, *33*, 637 – 640.

[44] Mezzenga, R.; Grigorov, M.; Zhang, Z.; Servais, C.; Sagalowicz, L.; Romoscanu, A. I.; Khanna, V.; Meyer, C. *Langmuir* **2005**, *21*, 6165–6169.

[45] Amar-Yuli, I.; Adamcik, J.; Lara, C.; Bolisetty, S.; Vallooran, J. J.; Mezzenga, R. *Soft Matter* **2011**, *7*, 3348–3357.

[46] Mezzenga, R.; Meyer, C.; Servais, C.; Romoscanu, A. I.; Sagalowicz, L.; Hayward, R. C. *Langmuir* **2005**, *21*, 3322–3333.

[47] Taylor, A.; Sinclair, H. *Proceedings of the Physical Society* **1945**, *57*, 126–136.

[48] Förster, S.; Timmann, A.; Konrad, M.; Schellbach, C.; Meyer, A.; Funari, S.; Mulvaney, P.; Knott, R. *J. Phys. Chem. B* **2005**, *109*, 1347–1360.

[49] Marrink, S. J.; Tieleman, D. P. *J. Am. Chem. Soc.* **2001**, *123*, 12383–12391.

[50] Scriven, L. E. *Nature* **1976**, *263*, 123–125.

[51] Luzzati, V.; Spegt, P. A. *Nature* **1967**, *215*, 701–704.

[52] Zabara, A.; Amar-Yuli, I.; Mezzenga, R. *Langmuir* **2011**, ASAP.

[53] Helfrich, W. *J. Phys. Condens. Matter* **1994**, *6*, A79–A92.

[54] Nissim Garti, S. E. I. T. . G. B., A. Aserin *J. Colloid Interface Sci.* **1996**, *178*, 60 – 68.

Chapter 3

Targeting and Delivery of Hydrophobic Compounds Using Nanoparticles of Monoglyceride Cubic Phase

Contents

3.1 Introduction

The property of surfactant to form self assembled structures in polar solvents such as water makes it as a desirable candidate for many applications.[1–5] Supramolecular assemblies formed by lipid self-assembly are organized into hydrophobic and hydrophilic regions into which desired molecules can be incorporated.[6–9] Self assembled structures formed by monoglycerides have recently attracted interest in several applications such as membrane protein crystallization and as drug delivery vehicles due to the inherent bio compatibility of such lipids.[1,10–14] Monoolein, one of the most common monoacylglycerols, is a potential candidate for pharmaceutical applications because of its availability in high purity and low cost.[15,16] Various liquid crystalline phases have investigated used for drug delivery applications. For example, the lamellar phase has been used as a precursor for forming the cubic phase in injectable vehicles.[17,18] The cubic phase is of particular importance, since it can coexist with excess water.[3,19] This makes it a promising candidate for applications such as crystallization of the membrane proteins.[20–25] The geometry of the cubic phase protects lipophilic molecules from water and hydrophilic molecules.[26] The lipophilic molecules are segregated to the interfacial regions of the mesophase, such that they are protected from exposure to radicals in solution that might reactive degradation.[27] Further, the cubic phase can be formulated into dispersions of smaller particles, termed cubosomes, that retain the internal symmetry of the parent liquid crystalline phase.[28–38] Similar to the parent cubic phase, cubosomes are capable of simultaneous loading with hydrophobic and hydrophilic compounds. Thus cubosomes find numerous applications in drug delivery, bio-imaging and charge directed targeting.[37,39,40]

A systematic approach towards developing cubosomes as drug delivery systems is still missing because of the absence of detailed in-vivo and in-vitro studies. Here we present a systematic way of making a formulation that is found to be very promising in the case of loading of hydrophobic and hydrophilic compounds. It is also possible to change the

surface charge of the nanoparticles by coating them with appropriate polyelectrolytes such as poly-ϵ-lysine (PϵL) to use for specific targeting.[41,42] In order to target the cubosomes based on the charge, it is necessary to prepare particles with different charges. The method of layer-by-layer (LbL) adsorption of polyelectrolytes onto charged surfaces is a potential technique for changing the surface properties of the nanoparticles.[41,43,44] In this method, the polyelectrolytes get assembled on the oppositely charged surfaces by Coulomb attraction and other interactions.[45–47] The technique offers advantage over the convensional cubosomes, still the preparation of multi-layered cubosomes are lengthy and time consuming process. Here we perform the preparation of a single layer of PϵL, their characterization and application on charge directed substrate adsorption. The LbL technique is useful for making ordered assembly of nanoparticles for biological functions and for making electronic devices. This chapter aims at investigating the properties of cubosomes that can be tuned for applications in drug delivery systems and photonics.

3.2 Experimental Section

Rylo MG 20 Pharma, a commercial grade emulsifier was received as a generous gift from Danisco (India) and is used as received. Pluronic F127 was obtained from BASF and poly-ϵ-lysine was obtained from Sigma chemicals. Information from the manufacturer indicates that Rylo MG 20 Pharma contains about 95% of monoglycerides mainly monoolein. Pyrene and Nile Red were obtained from Aldrich chemicals and are used as received. Naproxen sodium salt was provided by Lupin Chemicals Pune. Poly-ϵ-Lysine (M_w = 20000) was obtained from CMS Chemicals Ltd (UK).

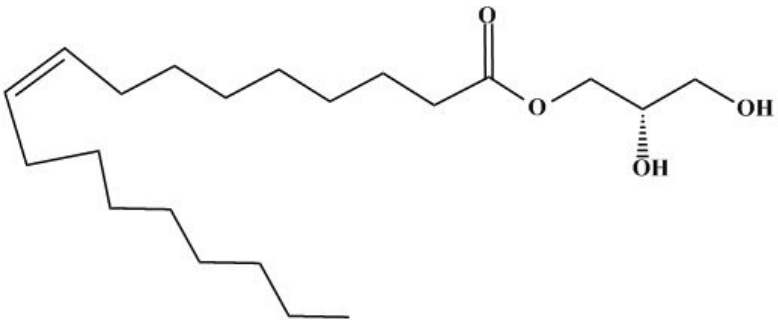

(a)

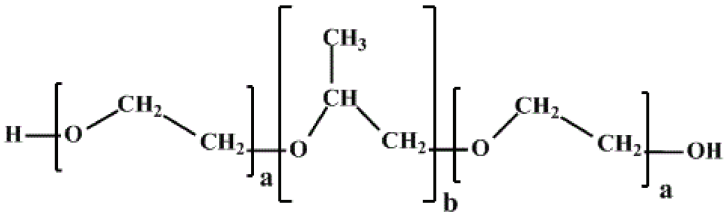

(b)

Figure 3.1: Molecular structure of (a) monoolein and (b) Pluronic F127.

3.2.1 Cubosome Preparation

Cubosomes were prepared using a modification of a reported protocol (Figure 3.2).[28,32,33] Briefly, F127 Pluronic was mixed well with the Rylo melt at 80°C to prepare a Rylo/F127 blend. The Rylo:F127 ratio was kept constant at 100 : 5 so as to minimize the formation of vesicles during the preparation of the cubosomes. This ratio was chosen such that the final composition is in the cubic phase region. The Rylo/F127 blend was added to deionized water and homogenized using an Ultraturrax T25 from IKA at 12000 rpm for 15min. The milky turbid dispersion thus formed was found to be stable for more than one month. This milky dispersion was characterized using SAXS and cryo-TEM and was observed to comprise primarily of cubosomes (that we denote

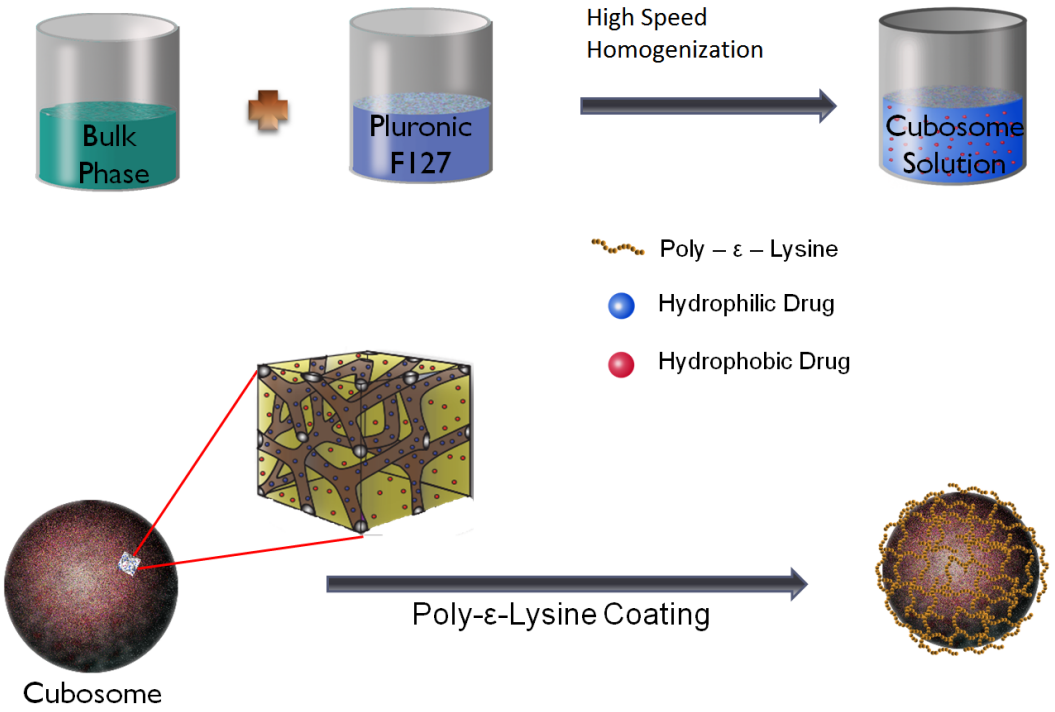

Figure 3.2: Schematics for preparing cubosomes

RF, for Rylo/F127). We tried high pressure homogenization using an Avestin B15 homogenizer, but even relatively mild conditions (air pressure of 60 psi) resulted in the formation of a significant number density of vesicles. Therefore, we did not use high pressure homogenization for particle size reduction in this work. Cubosomes loaded with a model hydrophobic compound (Nile Red) were prepared using the same protocol but starting with a mixture of the Rylo/F127 blend with a calculated amount of Nile Red. For loading Naproxen sodium, a hydrophilic nonsteroidal anti-inflammatory drug, into the cubosomes, the following method was used. Naproxen sodium aqueous solution was prepared in deionized water and added to molten Rylo in 40 : 60 ratio in order to form a $Pn3m$ cubic phase. To this $Pn3m$ cubic phase was added an F127 solution in deionized water, such that the Rylo/ F127 ratio was 100 : 5. This mixture was homogenized using the IKA Ultraturrax T25 to obtain cubosome dispersion. For simultaneous loading of Naproxen sodium and Nile Red, a blend of Rylo and Nile Red was prepared. Naproxen

solution in deionized water was added to the molten blend of Rylo/Nile Red in the ratio of 40 : 60 to get a $Pn3m$ cubic phase. The $Pn3m$ phase was then homogenized in F127 solution in deionized water, such that the Rylo/F127 ratio is 100 : 5.

The coating of cubosomes with poly-ϵ lysine, the technique of layer-by-layer (LbL) assembly is followed.[43] In this technique, the polyelectrolyte layers are adsorbed on an oppositely charged surface by means of electrostatic binding. Even though, we have not done any measurement to verify only one layer is coated on the cubosome, the previous reports[42,46] on this technique ensures that it is very unlikely to form multiple layers if the coating density of the polyelectrolytes are selected carefully. The average size of the cubosomes is obtained using dynamic light scattering (DLS). We estimate the number density of cubosomes in solution from the DLS average size and the amount of Rylo added to water. This gives us the surface area of the cubosomes in solution. The amount of PϵL is selected in such a way that it has a coverage of 0.5mg/m^2. Then, we add the calculated amount of PϵL solution, dropwise, to the cubosome dispersion under continuous vortexing. Particular care has been taken to add the PϵL solution slowly such that the cubosomes are not phase separated. The so obtained solution has a polymer coating density of 0.5mg/m^2 (designated $RF_{P\epsilon L}$). The solution is kept for 2 days for aging and the coating of the cubosomes are confirmed by ζ potential measurement. The reports of Driever et al. shows a single layer of PϵL get coated on the surface as measured by Quartz Crystal Microbalance (QCM) using this procedure.

3.2.2 Dynamic Light Scattering (DLS)

Dynamic light scattering is used for the determination of the size and ζ potential of the cubosome samples. The DLS experiments were done on BIC 90 Plus Particle size analyzer from Brookhavens Instruments Corporation, USA. A He-Ne laser ($\lambda = 632.8$nm) is used and the detector is kept at a fixed angle of 90°. The data is analyzed using the

in-built software in the system to obtain the particle size distribution. The ζ potential is measured using the ζ potential analyzer attachment in the same instrument. The sample for both DLS and ζ potential is prepared after diluting the cubosome solution to avoid multiple scattering and doing ultrasonication for about 20min. DLS and ζ potential for the coated cubosomes were done without sonicating the samples as sonication causes the layer of PϵL coating to get removed.

3.2.3 Confocal Microscopy

Confocal microscopy is done using LSM 710 laser scanning microscope from Carl Zeiss, Germany. The samples were taken in a cavity slide and the slides are sealed before recording the images. The cubosomes are stained with Nile Red dye, which has an absorption wavelength of 519.1nm. We use Argon laser line of wavelength 514nm for exciting the dye and the image has been acquired using the ZEN 2009 software from Carl Zeiss.

3.2.4 Small Angle X-ray Scattering (SAXS)

The SAXS experiments are done on a Bruker Nanostar with rotating anode and pinhole geometry. The instrument uses Cu-K_α radiation of wavelength 1.54Å and a sample to detector length of 105cm. The anode operates at a potential difference of 45kV and a current of 100mA. The samples are taken in a 2mm quartz capillary having a wall thickness of 10µm. The scattering from glassy carbon film is taken as the reference. A Peltier unit is used for temperature control of the sample holder. The data is collected on a HISTAR gas filled multi-wire detector and the 2D data is circularly averaged to get a 1D curve. The detector is calibrated using the scattering from silver behenate ($AgC_{22}H_{43}O_2$). The samples are scanned long enough to get at least two million counts and the data are normalized with the transmission coefficient of the sample and the scan

time. The different liquid crystalline phases are identified using the relative positions of the SAXS Bragg peaks. Double diamond cubic phase having an internal symmetry of $Pn3m$ is identified using the SAXS Bragg peaks appearing at q values in $\sqrt{2} : \sqrt{3} : \sqrt{4} : \sqrt{6} : \sqrt{8} : \sqrt{9} : \sqrt{10} : \sqrt{11} \ldots$. Similarly other cubic phases can also be identified by their characteristic peak positions.

3.2.5 Cryo-TEM

The cryo-TEM experiments were done at Indian Institute of Bombay. Samples were prepared for Cryo-TEM by the frozen hydrated vitrified technique[48] using a Vitrobot Mark IV semiautomated sample preparation system. About 3µl of liquid sample was taken on a lacey fomvar carbon coated 200 mesh copper grid kept in an environmental chamber at a temperature 22°C and humidity 85%. The sample was made into a thin film by blotting once for one second with a blot force setting of one, and then plunged into liquid ethane at its freezing point. The resultant vitrified grid was transferred under liquid nitrogen to a Gatan model 655 cryo holder with a cryo-transfer system, and then cryo-transferred into the TEM goniometer while maintaining the cold chain throughout. Imaging was done in a JEOL 2100 HRTEM operating at 200keV while maintaining the sample holder at about -172.6°C as measured by a Gatan Smartset model 900 cold stage controller.

3.2.6 Stability Test

In order to check the stability of the cubosome samples in simulated biological fluids, the size of cubosomes in Bovine Serum Albumin (BSA) is measured as a function of time, using dynamic light scattering (DLS). Both the coated and uncoated cubosomes were mixed with 1.4% and 10% of BSA and the effective particle size is measured as a function of time. The sampling is done at different times and all the concentrations

prepared for the DLS experiments are kept constant. The experiment is done at a fixed angle of 90° and the scattering counts are also taken for the verification of the results. The experiments are done in triplicate and the error bars are found to be reasonably small. Similar experiments are performed with DPBS buffer.

3.2.7 Adsorption on a Substrate

We adsorb cubosomes on treated glass cover slip that are used as model substrates. The substrate is prepared using the procedure given below. The glass slide is etched with piranha solution to remove any organic impurities present and to make it negatively charged. The so obtained glass slide is partly dipped in a solution of high molecular weight polyethyleneimine (PEI, $Mw = 700000$g/mol) of concentration 1mg/ml, containing 10mM NaCl. This induces positive charge on the portion of the cover slip that is dipped in the polymer solution. We use cubic phase particles containing Nile Red dye so that confocal microscopy can be used to characterize cubosome adsorption on the coverslip. The coated coverslip is dipped in the cubosome solution in order to investigate the particle adsorption.

3.3 Results and Discussion

The Rylo MG consists of distilled monoglycerides made from sun flower oil. This industrial product contains about 95% of monoglycerides and some higher components. We determined the phase diagram of Rylo and found that our data is consistent with the reported phase behaviour for glycerol monooleate.[15] The double diamond cubic phase (identified by the space group $Pn3m$) is of specific interest to this work because of its ability to coexist with water at higher water concentrations. Thus, $Pn3m$ phase particles can be dispersed in an aqueous phase, that can be simultaneously loaded with

hydrophobic and hydrophilic molecules.[7,49,50] Even though the exact details about the melting transitions of these phases in presence of additive components are not clearly investigated, our observations show that the hydrophilic additives changes the LC phase formed and thus the melting transitions (data not shown). A complete investigation in this aspect is beyond the scope of the thesis and we restrict ourselves in a region well away from the phase boundaries. These nanoparticles are stabilized using a block copolymer, Pluronic F127 in order to prevent them from aggregation. The cubic phases can be used for different applications by making them into dispersions in water.[32,33]

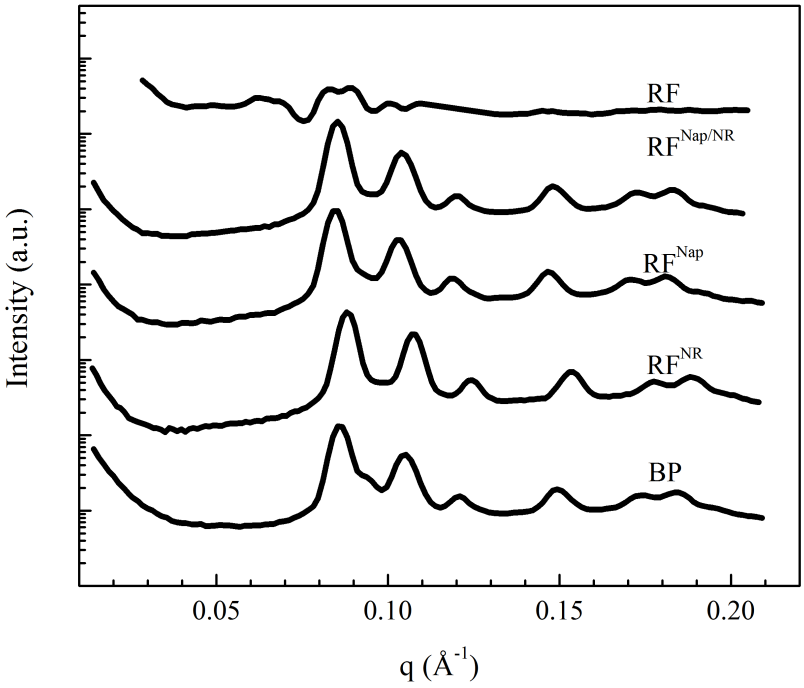

Figure 3.3: SAXS pattern for the cubosomes and the bulk phase (BP) before and after loading with hydrophobic (nile red) and hydrophilic (naproxen) molecules: (BP^{NR}) BP loaded with Nile Red, (BP^{Nap}) BP loaded with Naproxen sodium, ($BP^{Nap/NR}$) BP loaded with Nile Red and Naproxen sodium.

Rylo/F127 mixtures form liquid crystalline mesophases that were characterized using small-angle X-ray scattering (SAXS, Figure 3.3). For the Rylo/F127 bulk phase

(BP,Figure 3.3), we observed SAXS peaks characteristic of a double diamond cubic phase characterized by space group $Pn3m$, with a lattice parameter of 103.2Å).[36,51,52] On homogenizing BP, we obtain a turbid, milky dispersion that we term RF. RF was characterized using cryo-TEM and SAXS. Cubic mesophases of glycerol monooleate scatter X-rays poorly, necessitating long acquisition times Therefore, for low concentration RF dispersions, the SAXS data is noisy. However, the locations of the first two peaks (around 0.08 and 0.11$Å^{-1}$, Figure 3.3) are similar to those for BP and suggest that the $Pn3m$ cubic phase structure is retained in RF. The RF also shows the presence of other peaks (for example, around 0.06$Å^{-1}$), indicating that a small fraction of other mesophases might also be present. We estimate an apparent cubic phase lattice parameter ($\approx$ 107$Å^{-1}$) for the RF dispersion, higher than for BP. We term the lattice parameter as apparent due to uncertainties in determining the peak positions due to poor scattering from RF dispersions, combined with the presence of other phases. Confirmation for the cubic phase internal organization in the RF particles comes from cryo-TEM (Figure 3.4). The RF dispersion comprises polydisperse particles that are smaller than about 200nm (Figure 3.4a). In the cryo-TEM images, RF particles exhibit a faceted shape, characteristic of cubosomes and, show evidence for internal organized microstructure. We also observed the coexistence of vesicles. These are known to form[33] when high speed homogenization is used for cubosome synthesis. In protocols typically reported in the literature, the homogenization step is followed by prolonged heat treatment to eliminate vesicular structures.[53] However, since several drugs are temperature- sensitive, our synthesis protocol does not employ heating. Even without the heat treatment, we observe that the RF sample contains predominantly cubosomes, with only a small fraction of vesicles.

The $Pn3m$ cubic phase is retained even on loading the Rylo/F127 bulk phase with a hydrophilic drug (Naproxen Na, up to a loading of 1% by weight (Figure 3.5a and Figure 3.5b) or, hydrophobic molecule, Nile Red, up to a loading of 0.05% by weight (Figure

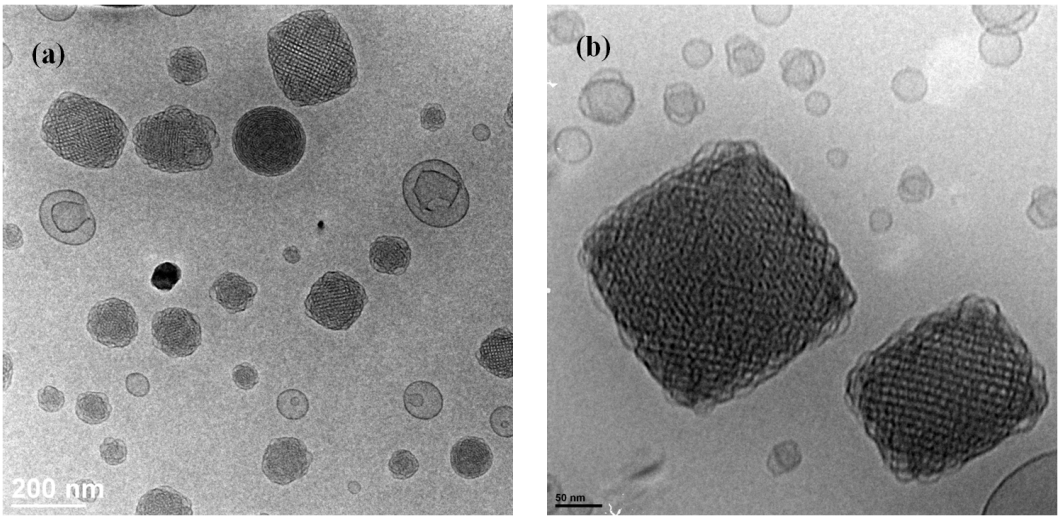

Figure 3.4: Cryo-TEM for (a) cubosomes (RF) and (b) Naproxen and Nile Red ($RF^{Nap/NR}$) loaded samples. The internal structure remains unaltered for both the samples.

3.5a and Figure 3.5b) or with a combination of hydrophilic drug (Naproxen Na) and hydrophobic dye (Nile Red). Incorporation of the hydrophobic dye decreases the lattice parameter to 101.4Å, while loading of hydrophilic Naproxen Na results in an increase to 105.5Å (relative to 103.2Å, observed for BP). Remarkably, there is very little change in the lattice parameter relative to BP on simultaneous loading of Nile Red and Naproxen Na (103.6Å for $BP^{Nap/NR}$, Figure 3.3).

Incorporation of hydrophobic or hydrophilic moieties can change the critical packing parameter (CPP) associated with the lipid[2] resulting in dramatic changes in mesophase organization.[36,54,55] For example, a recent report[56] indicates the formation of "rose" like particles on incorporation of a hydrophobic molecule in a Rylo/water phase. However, for loadings of up to 1% of Naproxen Na, or 0.05% of Nile Red, we observe that the $Pn3m$ phase is retained in the Rylo/water system. Cryo-TEM confirms that homogenization of $BP^{Nap/NR}$ (to form $RF^{Nap/NR}$ dispersions) results in the formation of faceted internal cubic phase dispersed particles, similar to those observed for RF dispersions (Figure 3.4). As in the case of RF, we observe a few vesicle structures and note the formation of

lamellar phases at the outer surface of the $RF^{Nap/NR}$ that we attribute to F127 surface layers, in accord with the literature.

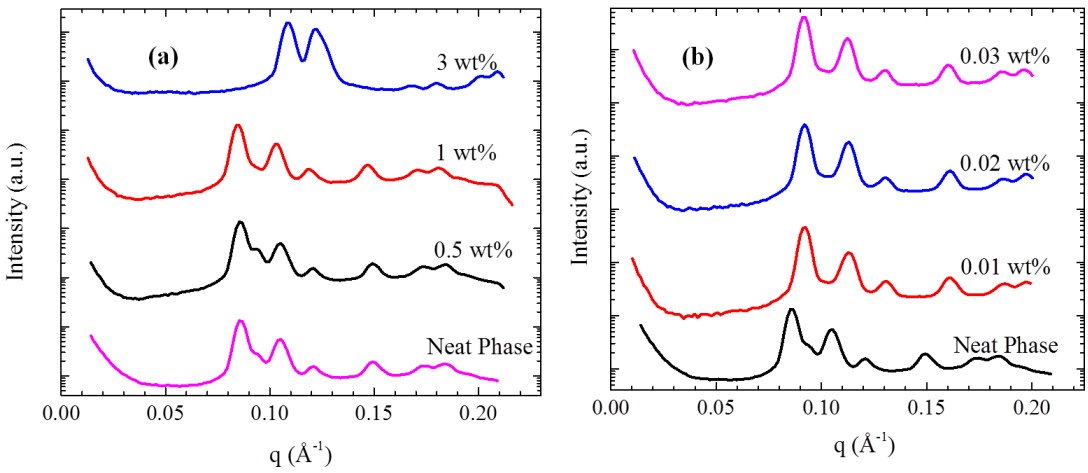

Figure 3.5: Loading capacity for (a) hydrophilic molecule (Naproxen Sodium) and (b) hydrophobic molecule (Nile red) in the bulk $Pn3m$ phase, characterized by SAXS. Cubic phase was maintained up to $1wt\%$ and $0.05wt\%$ of naproxen and Nile Red respectively.

The change in the lattice parameter in the cubic phase can be rationalized by considering how the incorporated moieties are localized in the mesophase.[2] Hydrophilic molecules are localized in the water channels and increase the effective hydrophilic headgroup area of the lipids.[2,19,54] We observe that this is associated with an increased lattice parameter. Conversely, when hydrophobic molecules are loaded in the cubosomes, these molecules are likely to be localized near the lipid tails. This is associated with a decrease in lattice parameter. For the simultaneous loading of hydrophilic and hydrophobic molecules, the lattice parameter remains essentially unchanged. We note that $BP^{Nap/NR}$ is a four-component system and is likely to manifest complex phase behavior. Therefore, the fact that $BP^{Nap/NR}$ exhibits a cubic phase with a similar lattice parameter to BP is fortuitous.

3.3.1 Layer-by-layer assembly using PϵL

Surface functionalization of cubosomes gives many advantages over conventional cubosomes in terms of their stability and their ability to be targeted to specific sites. However, F127 is chemically inert and is not amenable to chemical conjugation, precluding surface functionalization of cubosomes. Therefore, we have electrostatically coupled RF cubosomes with a cationic natural homopolymer, poly-ϵ-lysine (PϵL). RF cubosomes are negatively charged, and exhibit a zeta potential of -24 ± 7mV. The origin of the negative zeta potential for cubosomes has been attributed to the adsorption of hydroxyl ions at the cubosome surface.[57] Commercially available Rylo that was used to prepare cubosomes in our work also contains some free oleic acid, that too might also contribute to the observed zeta potential. PϵL coated cubosomes, termed, RF$^{P\epsilon L}$, exhibit a size (by DLS) of 200 ± 39nm, slightly larger than RF (DLS size of 165 ± 25nm). The ζ potential after coating changes from about -24 ± 7 to $+2 \pm 1$mV, providing evidence for the complexation of PϵL with the cubosome surface . Cryo-TEM of confirms that the PϵL coating does not alter the cubic phase internal structure of the cubosomes.

Batch	**Diameter (nm)**	**Polydispersity**	**ζ Potential (mV)**
RF1	116	0.186	-33.8
RF1$^{P\epsilon L}$	149	0.23	+2
RF2	181	0.132	-20.2
RF2$^{P\epsilon L}$	182	0.23	+3.8

Table 3.1: The diameter and zeta potential of different batches of cubosomes are shown in the table. The notation RF1 and RF2 are two batches of uncoated cubosomes and RF1$^{P\epsilon L}$ and RF2$^{P\epsilon L}$ are those coated with PϵL.

The sizes of the cubosomes are obtained using DLS. The sizes of the cubosomes are tabulated in the Table 3.1. We note that the size of the cubosomes are always below 200nm. The uncoated particles are found to have a negative charge as indicated in the ζ potential measurements. This changes upon coating the cubosomes with PϵL, when the cubosomes exhibit positive values of ζ potential. Further size reductions are possible

only by applying high pressure energy inputs to the system using an ultrasonic bath or a high pressure homogenizer. However, when this is done, we observe the formation of larger number density of vesicles (rather than cubic phase particles) in the system. In the literature, a high temperature annealing step is employed to convert the vesicles into cubic phase particles. Specifically, the samples are kept in the autoclave for 15min at 125°C to transform the vesicles into cubosomes. Unfortunately, in our experiments, where the cubosomes are loaded with hydrophilic drug, we observe a phase separation (and some possible degradation) of the drug on high temperature treatment, and the PϵL surface coating is removed. This constrains us to work with the aforementioned protocol for the preparation of the cubosomes. Since we do not employ homogenization, we obtain a polydisperse sample of cubosome particles.

Recently, layer-by-layer (LbL) coating of cubosomes using electrostatic complexation of alternating layers of polymethacrylic acid and poly-L-lysine has been reported by the group of Driever et al.[46]. In their work, the first layer on the cubosome surface was hydrophobically anchored through a specially synthesized anionic copolymer containing a hydro- phobic anchoring moiety. They reported that this strategy of using a strongly anchored polyanion on the cubosome surface was essential for multilayer formation. They claim that complexation of polycations with hydroxyl ions adsorbed on the cubosome surface could not sustain multilayer formation. Further, LbL on the cubosome surface necessitated separation of free polyanion-polycation complexes using centrifugation. They reported that release of a model hydrophilic compound, fluorescein, was modulated for cubosomes coated with seven polymer layers, with a moderate decrease in the initial burst release, relative to uncoated F127 stabilized cubosomes.

In our work, we deposit only a single layer of PϵL on the cubosome surface. A calculated amount of PϵL is added to the cubosome layer (as detailed in the Experimental section), such that a surface coating of about 0.5mg/m^2 is obtained (comparable

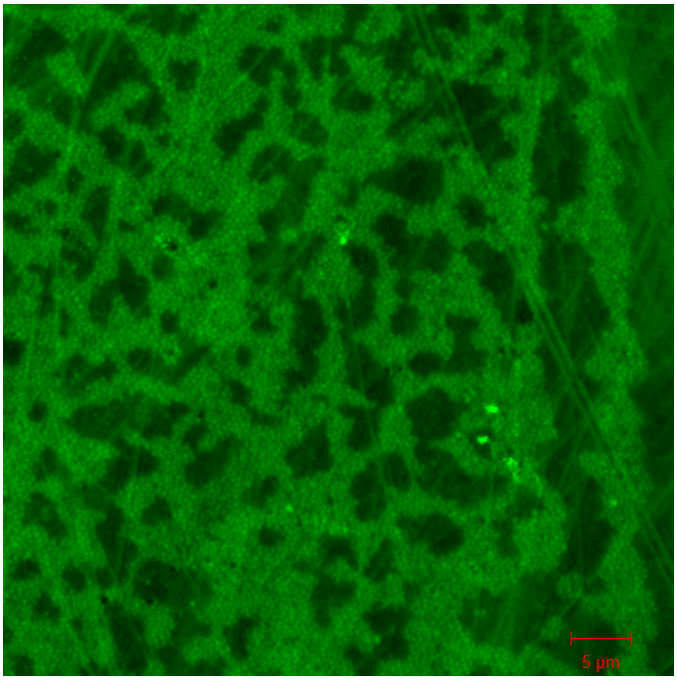

Figure 3.6: Confocal microscope image of the cubosomes dropcasted on a coverslip stained with Pyrene. This clearly shows the formation of cubosomes rather than vesicles.

to literature estimates of the surface coverage obtained by electrostatic polyelectrolyte complexation). Remarkably, work from our group[47] indicates that even this single layer of PϵL is able to retard the initial burst release of hydrophilic Naproxen Na from loaded cubosomes. Further, we observe that the PϵL coated cubosomes thus obtained are stable in solution and do not aggregate over several days. While the zeta potential for PϵL-coated cubosomes is only marginally positive, this compares well with that obtained by Driever et al.[46] for cubosomes coated with a single layer of polycation. Our strategy has the significant advantage that it involves no separation steps.

3.3.2 Stability with BSA

The stability of the cubosomes in complex biological media, such as blood, is crucial for its use in drug delivery systems. Bovine serum albumin is known to disrupt the cubic phase since monoolein binds to specific sites on the protein. Therefore we tested the

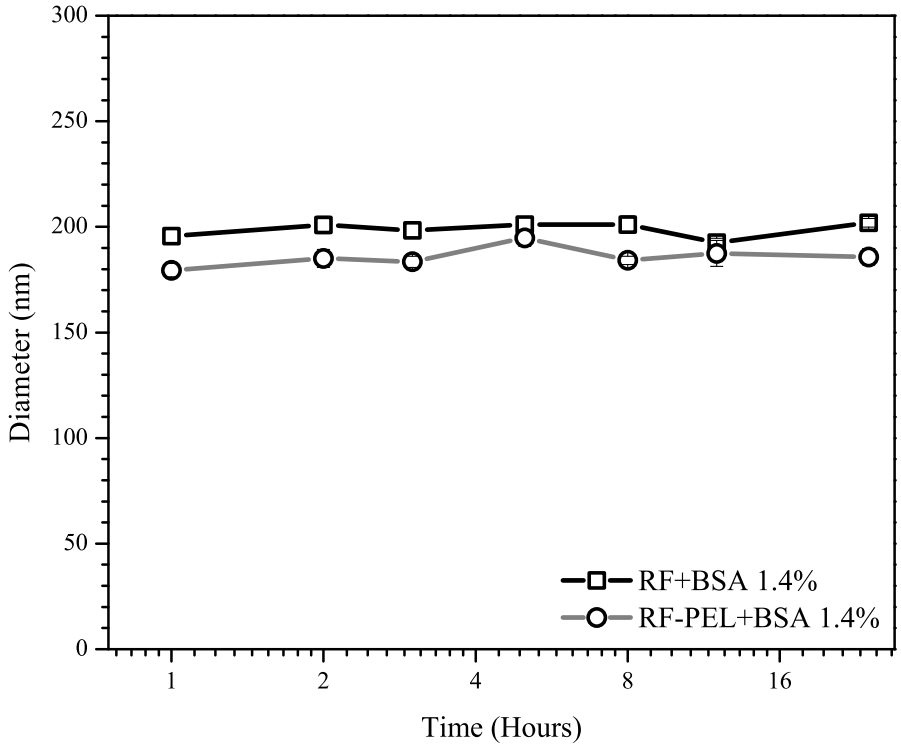

Figure 3.7: The Size changes of RF and $RF^{P\epsilon L}$ over time after incubating in 1.4% BSA buffer.

stability of the cubosomes on incubation with aqueous dispersion of BSA proteins. The stability of the cubosome with the BSA protein is studied using DLS as a function of time (Figure 3.7, 3.8). BSA protein is added to the cubosome solution and DLS is performed at different intervals of time in order to check if the cubosomes remain inact in the BSA dispersion.

Figure 3.7 show that in the presence of 1.4% of BSA, there is no change in the average particle size for both coated and uncoated cubosomes over a period of 24h. In the plasma, there are esters that are known to degrade monoolein. As a result, BSA has been reported to disrupt the cubic phase structure and cubosomes disintegrate in the presence of BSA. However, here we have observed that cubosomes remain stable even in the presence of

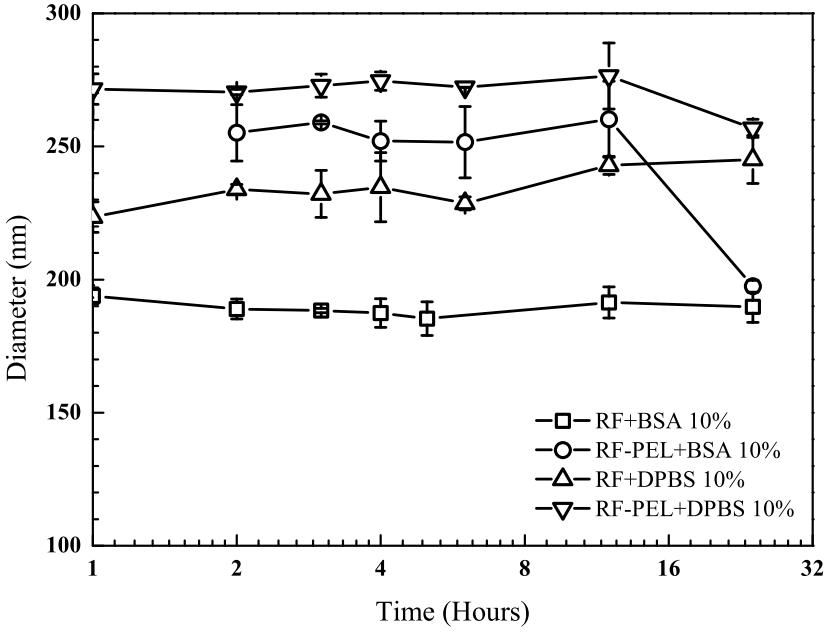

Figure 3.8: The size changes of RF and $RF^{P\epsilon L}$ over time after incubating in 10% BSA buffer and 10% DPBS buffer taken for 24h.

10% BSA (Figure 3.8). It is observed that the cubosomes are stable upto a period of 12h in the presence of BSA. After 24h, a reduction in particle size is observed for both the coated and non-coated cubosomes. This size reduction is in the cubosomes are attributed to the disruption of vesicles formed in the system. Our data reveals that the cubosomes are stable against aggregation and destabilization due to BSA for a time period of 24h (Figure 3.7). Thus both coated and uncoated cubosomes exhibit excellent stability even in the presence of BSA. Thus it appears that cubosomes are stable and do not change size in the presence of BSA or DPBS buffer.

3.3.3 Charge-Based Adsorption

As prepared cubosomes, stabilized by F127, are negatively charged. When the cubosomes are coated with a polycation, the sign of the zeta potential changes and the

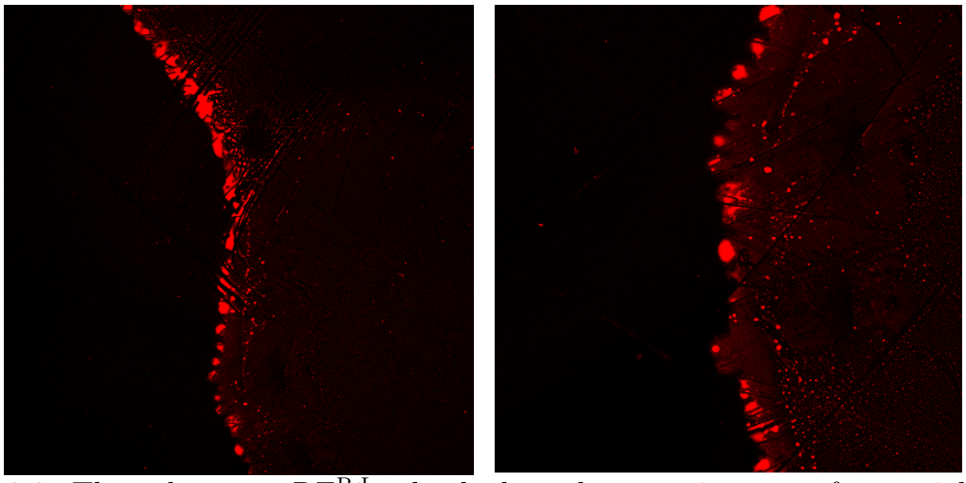

Figure 3.9: The cubosomes RF^{PeL} adsorbed on the opposite part of a partially charged coverslip functionalised by Piranha solution imaged using confocal microscopy. The red colour indicates the area of the coverslip where cubosome is adsorbed. The dark part is the part of the coverslip which is positively charged.

cubosomes are positively charged. We demonstrate that such cubosomes can be spatially localized at specific locations based on the particle zeta potential. This charge based targeting is of advantage in applications in photonic materials and in pharmaceutical formulations where spatial localization based on surface charge can be employed to control material preparation. A coverslip having partial positive spatially separated from regions of negative surface charge is used as a model substrate for these experiments. The partially charged coverslip was dipped in the cubosome solution and the coverslip was investigated after washing. We observe that the cubosomes are adsorbed electrostatically. Here it is observed that when the slide which is having partial positive charge and partial negative charge is dipped in the cubosome solution, the coated cubosomes (positively charged) get coated on the part where there is a negative charge. Since the cubosomes are stained with nile red, the red colour in Figure 3.9 shows indicates the regions into which the stained cubosomes adsorbed. The cubosomes are adsorbed only on those regions which are negatively charged. The positively charged part of the coverslip are unadsorbed by the cubosomes are shown as dark part in Figure 3.9.

3.4 Conclusions

Cubosomes, which are lipid particles of cubic phase $Pn3m$ internal symmetry, are versatile and can be simultaneously loaded with hydrophobic and hydrophilic compounds. Single layer coating on the nanoparticles with a bio-compatible polyelectrolyte poly-ϵ-lysine introduces multi-functionality to the cubosomes. Coated cubosomes form stable dispersion even in the presence of BSA. Both coated and uncoated cubosomes exhibit excellent stability even in the presence of BSA. The cubosomes are found to retain its internal structure even after the simultaneous loading of Naproxen Sodium salt and Nile red dye as observed from the SAXS data. The multi-functional cubosomes are readily absorbed on a substrate and can be spatially localized to regions having opposite charge to that of the cubosome.

References

[1] Evans, D. F.; Wennerstrom, H. *The Colloidal Domain*, 2nd ed.; Wiley-VCH: New York, 1999; pp 1–632.

[2] Israelachvili, J. N. *Intermolecular and Surface Forces*, 3rd ed.; Elsevier Inc.: San Diego, 2011; pp 1–674.

[3] Mezzenga, R.; Meyer, C.; Servais, C.; Romoscanu, A. I.; Sagalowicz, L.; Hayward, R. C. *Langmuir* **2005**, *21*, 3322–3333.

[4] Briggs, J.; Chung, H.; Caffrey, M. *J. Phys. II Fr.* **1996**, *6*, 723–751.

[5] Mitchell, D. J.; Tiddy, G. J. T.; Waring, L.; Bostock, T.; McDonald, M. P.; Sheffield, S. *J. Chem. Soc. Faraday Trans.* **1983**, *79*, 975–1000.

[6] Amar-Yuli, I.; Aserin, A.; Garti, N. *J. Phys. Chem. B* **2008**, *112*, 10171–10180.

[7] Amar-Yuli, I.; Libster, D.; Aserin, A.; Garti, N. *Current Opinion in Colloid and Interface Science* **2009**, *14*, 21–32.

[8] Couvreur, P. *Adv. Drug Deliv. Rev.* **2013**, *65*, 21–23.

[9] Fong, W.-K.; Hanley, T.; Boyd, B. J. *J. Control. Release* **2009**, *135*, 218–26.

[10] Sagalowicz, L.; Leser, M. E.; Watzke, H. J.; Michel, M. *Trends Food Sci. Technol.* **2006**, *17*, 204–214.

[11] Qiu, H.; Caffrey, M. *Biomaterials* **2000**, *21*, 223–234.

[12] Costa-Balogh, F. O.; Sparr, E.; Sousa, J. J. S.; Pais, A. In *Colloids for Nano- and Biotechnology*; Horvolgyi, Z. D., Kiss, E., Eds.; Progress in Colloid and Polymer Science; Springer-Verlag Berlin: Berlin, 2008; Vol. 135; pp 119–129.

[13] Costa-Balogh, F. O.; Sparr, E.; Sousa, J. J. S.; Pais, A. C. *Drug Dev. Ind. Pharm.* **2010**, *36*, 470–481.

[14] Ericsson, B.; Eriksson, P. O.; Lofroth, J. E.; Engstrom, S. *ACS Symp. Ser.* **1991**, *469*, 251–265.

[15] Ganem-quintanar, A.; Quintanar, D.; Buri, P. *Drug Dev. Ind. Pharm.* **2000**, *26*, 809–820.

[16] Guo, C.; Wang, J.; Cao, F.; Lee, R. J.; Zhai, G. *Drug Discov. Today* **2010**, *15*, 1032–40.

[17] Boyd, B. J.; Whittaker, D. V.; Khoo, S.-M.; Davey, G. *Int. J. Pharm.* **2006**, *309*, 218–26.

[18] Tamayo-Esquivel, D.; Ganem-Quintanar, a.; Martínez, a. L.; Navarrete-Rodríguez, M.; Rodríguez-Romo, S.; Quintanar-Guerrero, D. *J. Nanosci. Nanotechnol.* **2006**, *6*, 3134–3138.

[19] Mezzenga, R.; Grigorov, M.; Zhang, Z.; Servais, C.; Sagalowicz, L.; Romoscanu, A. I.; Khanna, V.; Meyer, C. *Langmuir* **2005**, 6165–6169.

[20] Caffrey, M.; Cherezov, V. *Nat. Protoc.* **2009**, *4*, 706–731.

[21] Caffrey, M. *J. Struct. Biol.* **2003**, *142*, 108–132.

[22] Caffrey, M. *Curr. Opin. Struct. Biol.* **2000**, *10*, 486–497.

[23] Ai, X.; Caffrey, M. *Biophys. J.* **2000**, *79*, 394–405.

[24] Cherezov, V.; Clogston, J.; Papiz, M. Z.; Caffrey, M. *J. Mol. Biol.* **2006**, *357*, 1605–18.

[25] Zabara, A.; Amar-yuli, I.; Mezzenga, R. *Langmuir* **2011**,

[26] Leser, B. M. E.; Michel, M.; Watzke, H. J. *Food, Colloids, Biopolym. Mater.*; The Royal Society of Chemistry, 2003; Chapter Food Goe, pp 3–14.

[27] Eastoe, J. In *Colloid Science : Principles, Methods and Applications*, 1st ed.; Cosgrove, T., Ed.; Blackwell Publishing Ltd.: Oxford, 2005; pp 50–76.

[28] Spicer, P. T.; Hayden, K. L.; Chester, W.; Lynch, M. L.; Ofori-boateng, A.; Burns, J. L. *Langmuir* **2001**, *17*, 5748–5756.

[29] Spicer, P. T.; Small, W. B.; Lynch, M. L.; Burns, J. L. *J. Nanoparticle Res.* **2002**, *4*, 297–311.

[30] Spicer, P. T. *Curr. Opin. Colloid Interface Sci.* **2005**, *10*, 274–279.

[31] Spicer, P. T. *Cubosome Formation via Dilution Kinetic Effects and Consumer Product Implications*; 2003; pp 1–14.

[32] Garg, G.; Saraf, S. *Biol. Pharm. Bull.* **2007**, *30*, 350–353, Garg, Gopal Saraf, Shailendra Saraf, Swarnlata.

[33] Barauskas, J.; Johnsson, M.; Joabsson, F.; Tiberg, F. *Langmuir* **2005**, *21*, 2569–2577.

[34] Siekmann, B.; Bunjes, H.; Koch, M. H. J.; Westesen, K. *Int. J. Pharm.* **2002**, *244*, 33–43.

[35] Yang, D.; Armitage, B.; Marder, S. R. *Angew. Chem. Int. Ed. Engl.* **2004**, *43*, 4402–4409.

[36] Yaghmur, A.; Campo, L. D.; Sagalowicz, L. *Langmuir* **2005**, *21*, 569–577.

[37] Mulet, X.; Boyd, B. J.; Drummond, C. J. *J. Colloid Interface Sci.* **2013**, *393*, 1–20.

[38] Yaghmur, A.; Glatter, O. *Adv. Colloid Interface Sci.* **2009**, *147*, 333–342.

[39] Pandey, R.; Zahoor, A.; Sharma, S.; Khuller, G. K. *Tuberculosis* **2003**, *83*, 373–378.

[40] Xie, J.; Lee, S.; Chen, X. *Adv. Drug Delivery Rev.* **2010**, *62*, 1064–1079.

[41] Caruso, F.; Lichtenfeld, H.; Giersig, M.; Mhwald, H. *J. Am. Chem. Soc.* **1998**, *120*, 8523–8524.

[42] Driever, C. D.; Mulet, X.; Johnston, A. P. R.; Waddington, L. J.; Thissen, H.; Caruso, F.; Drummond, C. J. *Soft Matter* **2011**, *7*, 4257.

[43] Bringley, J. F.; Wunder, A.; Howe, A. M.; Wesley, R. D.; Qiao, T. A.; Liebert, N. B.; Kelley, B.; Minter, J.; Antalek, B.; Hewitt, J. M. *Langmuir* **2006**, *22*, 4198–4207.

[44] Sukhorukov, G. B.; Donath, E.; Lichtenfeld, H.; Knippel, E.; Knippel, M.; Budde, A.; Mhwald, H. *Colloids and Surfaces A* **1998**, *137*, 253–266.

[45] Kato, N.; Schuetz, P.; Fery, A.; Caruso, F. *Macromolecules* **2002**, *35*, 9780–9787, doi: 10.1021/ma0209388.

[46] Driever, C. D.; Mulet, X.; Waddington, L. J.; Thissen, H.; Caruso, F.; Drummond, C. J. *Langmuir* **2013**, *29*, 12891–12900.

[47] Deshpande, S.; Venugopal, E.; Ramagiri, S.; Bellare, J. R.; Kumaraswamy, G.; Singh, N. *ACS Applied Materials and Interfaces* **2014**, *6*, 17126–17133, doi: 10.1021/am5047872.

[48] Bellare, J. R.; Davis, H. T.; Scriven, L. E.; Talmon, Y. *J. od Electron Microsc. Tech.* **1988**, *10*, 87–111.

[49] Garti, N.; Amar-Yuli, I.; Spernath, A.; Hoffman, R. E. *Phys. Chem. Chem. Phys.* **2004**, *6*, 2968–2976.

[50] Amar-Yuli, I.; Aserin, A.; Garti, N. *Some Characteristics of Lyotropic Liquid-Crystalline Mesophases*; Self-Organized Surfactant Structures; Wiley-VCH Verlag GmbH & Co. KGaA.

[51] Gustafsson, J.; Ljusberg-wahren, H.; Almgren, M.; Larsson, K. *Langmuir* **1996**, *12*, 1994–1996.

[52] Gustafsson, J.; Ljusberg-Wahren, H.; Almgren, M.; Larsson, K. r. *Langmuir* **1997**, *13*, 6964–6971.

[53] Worle, G.; Siekmann, B.; Koch, M. H. J.; Bunjes, H. *Eur. J. Pharm. Sci.* **2006**, *27*, 44–53.

[54] Kulkarni, C. V.; Wachter, W.; Iglesias-salto, G.; Engelskirchen, S.; Ahualli, S. *Phys. Chem. Chem. Phys.* **2011**, *13*, 3004–3021.

[55] Fong, C.; Le, T.; Drummond, C. J. *Chem. Soc. Rev.* **2012**, *41*, 1297.

[56] Murgia, S.; Bonacchi, S.; Falchi, A. M.; Lampis, S.; Lippolis, V.; Meli, V.; Monduzzi, M.; Prodi, L.; Schmidt, J.; Talmon, Y.; Caltagirone, C. *Langmuir* **2013**, *29*, 6673–6679.

[57] Svensson, O.; Thuresson, K.; Arnebrant, T. *Langmuir* **2008**, *24*, 2573–2579.

Chapter 4

Nanoparticle Size Controls Aggregation in Lamellar Nonionic Surfactant Mesophase

Contents

4.1 Introduction

The interaction of surfactants with nanoparticle surfaces[1] significantly affects dispersion stability. In turn, surfactant organization is influenced by nanoparticle-surfactant interactions. Therefore, an understanding of nanoparticle-surfactant interactions has technological implications for areas as diverse as formulating paints,[1] engineering food[2] and, designing nanomedicines[3] and metamaterials,[4] among others.[5]

There is considerable interest in understanding the structure and assembly of nanoparticle/surfactant systems, especially where the surfactant is organized as a mesophase.[6–18] Nanoparticles that interact with the surfactant matrix can alter the phase boundaries and, induce phase transitions relative to the neat surfactant system.[8–10,17] Several researchers,[11,13–15,18] including our group,[6] have demonstrated that nanoparticles significantly smaller than the characteristic mesophase dimension, are incorporated into the mesophase, while larger particles are excluded from the mesophase and form aggregates. Previously, our group has investigated[6,7] dispersions of silica nanoparticles in the hexagonal (H_1) phase of nonionic surfactants. We demonstrated that silica nanoparticles, varying in size from 8 to 500nm, formed linear aggregates at H_1 domain boundaries.[6] Adsorption of the nonionic surfactant, $C_{12}E_9$, as micellar structures on the nanoparticle surface[7] rendered the nanoparticle aggregation reversible. Thus, the silica nanoparticles readily redispersed on heating above the H_1-isotropic transition temperature and, aggregated into a particulate string phase on cooling into the H_1 phase.

Protein bionanoparticle organization, especially in surfactant cubic mesophases, have been investigated as a route to 'in cubo' crystallization of membrane proteins.[19–23] The structure of biomolecule-lipid assemblies have also been previously explored[24–26] in the context of using self-assembled lipid mesophases as media for the entrapment and solubilization of biomolecules. Guest molecules can influence the structure of a matrix mesophase. For example, it has been demonstrated that loading of proteins induces pat-

terning of the structure of cubosomes.[27] The use of monoglyceride-based inverse hexagonal phases for solubilization of neutracuticals,[28] lipolysis and drug release[29] have also been reported. Self assembled lipid phases can solubilize hydrophobic drugs, and have therefore, been reported to be useful as carriers for drug delivery applications.[30,31] Cubic phase nanoparticles called, 'cubosomes', have been reported as drug carriers for controlled drug delivery of hydrophobic and hydrophilic drugs.[32] Clearly, in all these applications, the effect of the guest molecules and proteins on the stability and phase behaviour of the host liquid crystalline matrix are of particular importance. In this context, several groups have tried to understand the effect of colloidal nanoparticles as model guest entities, on the structure of mesophase matrices.

Specifically, surfactant lamellar systems containing colloidal particles have been investigated in detail previously. Here too, as in the case of our previous work with H_1 mesophases, incorporation of particles within the lamellar phase is governed by the size of the nanoparticles, relative to the bilayer spacing. Bilayer lamellar stacks whose structure is governed by electrostatic head-group interactions typically expel nanoparticles from the mesophase domains, even for nanoparticles smaller than the bilayer spacing. However, lamellar phases, where the bilayer interactions are dominated by Helfrich repulsion, can accommodate nanoparticles whose sizes are smaller than the aqueous channel size.[33] Several groups have demonstrated that nanoparticles can influence the interlayer interactions in the lamellar phase, and typically induce bilayer attraction by suppressing layer undulations.[9,10,17] Terentjev[34] has suggested that nanoparticles incorporated in a lamellar phase form planar aggregates. Larger nanoparticles, with size comparable to the interlamellar spacing, have been shown to be excluded from the lamellar phase to form large aggregates.[13,14] Micron sized colloidal particles, when dispersed in a lamellar surfactant phase, stabilize a network of disclination lines by aggregating at the nodes of this defect network,[16] in exactly the same manner as particles dispersed in the smec-

tic phase of a small molecule mesogen.[35] Thus, a continuum description of the matrix mesophase is sufficient to describe the organization of large particles, when the particle size is significantly larger than the length scale that characterizes the mesophase (viz., mesogen size for small molecule liquid crystals, and bilayer repeat distance, for lyotropic L_α phases).

To the best of our knowledge, no previous study has systematically investigated the effect of nanoparticle size on their dispersion in a lamellar phase. The role of particle size, when nanoparticles interact with bilayers is especially important in the context of novel nanoparticle-based delivery devices. Recent studies have shown that small nanoparticles form pores in bilayer cell walls, while larger particles are coated and encapsulated by the cell walls.[3,36] Here, we investigate the influence of the size of silica nanoparticles when dispersed in a relatively hydrophobic surfactant, $C_{12}E_4$, that forms a lamellar phase at room temperature, over a wide concentration range.

4.2 Experimental Details

Nonionic surfactant tetraethyleneglycol monododecyl ether ($C_{12}E_4$) and silica nanoparticle dispersions were purchased from Sigma-Aldrich and used as received. All samples were prepared using distilled deionized water of resistivity 18.2MΩcm. The silica nanoparticle dispersions (trade names: Ludox FM, SM, LS and TM) have been thoroughly characterized by our group.[6] These particles are roughly spherical with diameters of 7.6 ± 1.9nm, 10.7 ± 1.9nm, 14.8 ± 1.8nm and 25.6 ± 1.6nm for the Ludox FM, SM, LS and TM, respectively, and are, therefore, termed S8, S11, S15 and S26, respectively.

Small angle X-ray scattering (SAXS) was performed on a Bruker Nanostar equipped with a rotating anode and three pinhole collimation. The instrument uses Cu-K_α radiation of wavelength 1.54Å and a sample to detector length of about 105cm. The anode operates at a potential difference of 45kV and 100mA. Samples were loaded in quartz

capillaries with diameter about 2mm and wall thickness of about 10µm. Scattering from glassy carbon was taken as the reference. A Peltier unit having an accuracy of ±0.1°C was used to control the temperature of the sample holder. Data was collected using a HI-STAR gas filled multi-wire detector, calibrated using a silver behenate standard. The 2D data from the detector was circularly averaged to obtain 1D data as a function of q (scattering vector, $q = (4\pi/\lambda)\sin(\theta/2)$). Samples were scanned for long enough to obtain at least 2 million counts and the scattering data was normalized with the transmission coefficient of the sample and the time of acquisition for comparison.

Contrast matching small angle neutron scattering (SANS) experiments were performed at the Dhruva reactor beamline, at the Bhabha Atomic Research Centre, Mumbai. The neutron beam has a wavelength of 5.2Å and a q range of 0.017 to 0.34Å^{-1}. The samples were prepared in mixtures of D_2O and H_2O where the ratio is chosen so as to match the scattering length density of the solvent with one of the components in the system. All the samples were equilibrated for at least 12h prior to measurements. SANS was performed on samples taken in 2mm thick quartz cuvettes. The data was monitored in real time and was corrected for background scattering. The data was converted into absolute intensity (cm^{-1}) using scattering from a reference sample. The data was convoluted with the wavelength spread ($\Delta\lambda/\lambda$) and the beam angular resolution. Here, we report data where the silica particles (scattering length density, $\rho_1 = 3.59 \times 10^{-6}$Å^{-2}) are contrast matched by choosing a water/D_2O ratio 40 : 60. The SANS data reported in this paper were analyzed using SASfit.[37]

A Nikon Eclipse E600 POL was used for optical microscopy. Images were recorded using a conventional digital camera connected to a PC. Samples were loaded on a Linkam CSS450 shear cell, that was used to control the sample temperature. The Linkam shear cell CSS450 is equipped with heaters situated above and below the sample, and computer-controlled liquid nitrogen dewar to provide active cooling. The sample was taken on the

quartz window of the Linkam shear cell and a cover slip was placed on the sample and the stage was heated and cooled at a controlled rate of 5°C/min with a liquid nitrogen pump and controller.

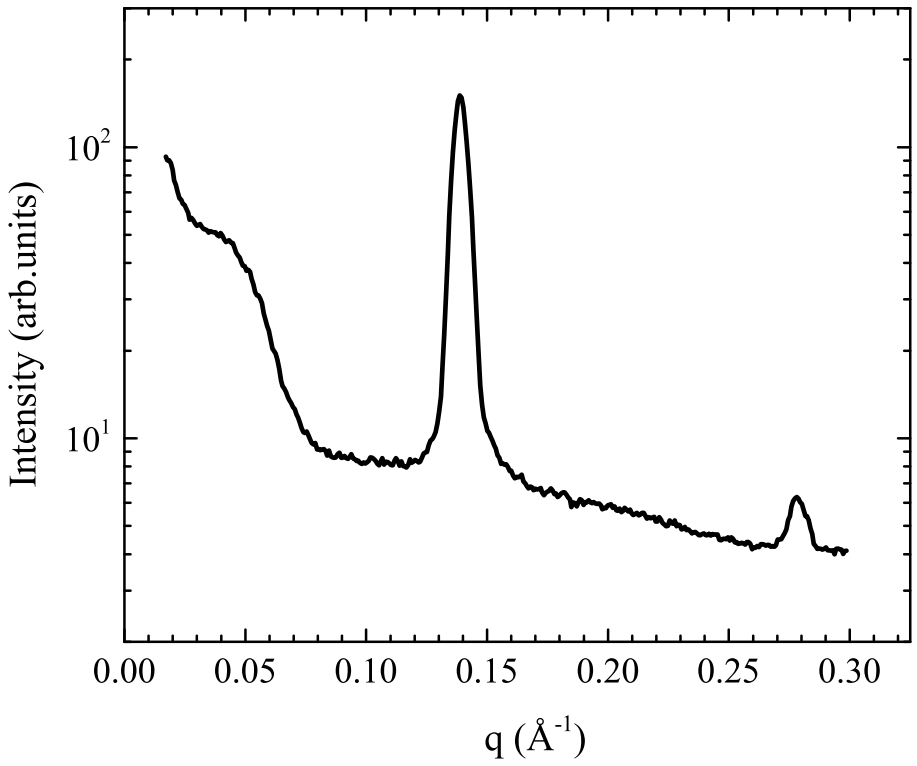

Figure 4.1: SAXS for composites containing 5% of silica particles S11 at 25°C. The second order lamellar peak is visible in the figure.

Freeze fracture SEM (FFSEM) was performed at EMEZ Electron Microscopy Centre, ETH Zurich. The sample is taken in a sealed container and quenched at a rate of 500°C/s. The sample is then stored in liquid nitrogen and microscopy is performed at 5kV and 200kx magnification.

When mixed with water, $C_{12}E_4$ forms a lyotropic lamellar phase over a concentration window of $\approx$ 45% to 85% at room temperature, in accord with the literature.[38] Here, we work with a $C_{12}E_4$-water ratio of 75 : 25 so that we are always well within the concentra-

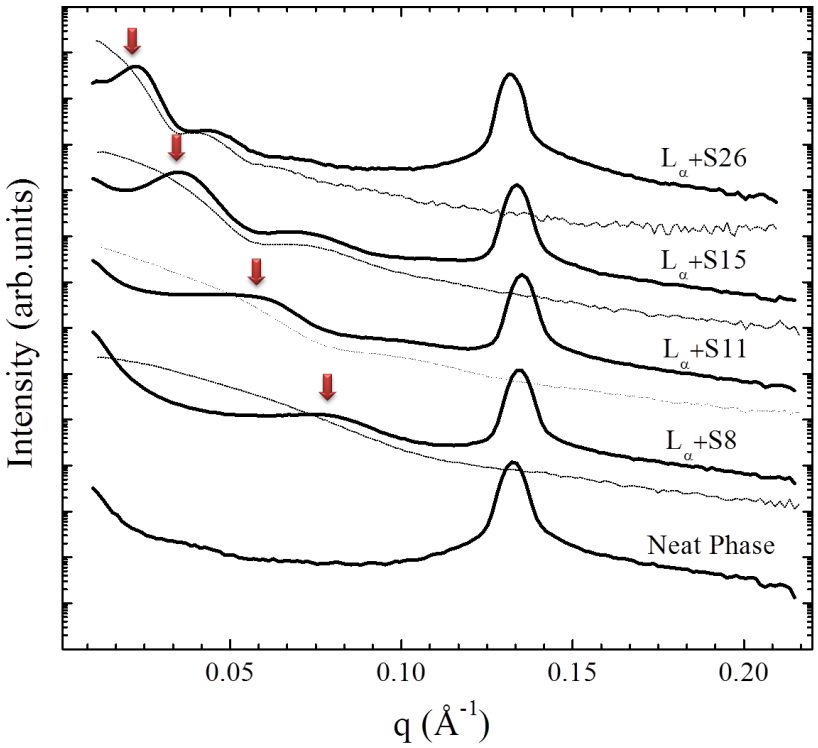

Figure 4.2: SAXS for the neat L_α phase and for composites containing 5% of silica particles S8, S11, S15 and S26 (from bottom to top). The form factor for the particles S8, S11, S15 and S26 are plotted near to the composite form SAXS as dashed lines. Datas are shifted vertically for ease of comparison. The arrows represent the correlation peak corresponding to aggregation of particles in the mesophase.

tion window for the lamellar phase. For this composition, we observe a surfactant fluid phase, L_2, above $T_{ODT} = 53°C$ and a lyotropic lamellar phase, L_α, below T_{ODT}. The L_α phase containing silica particles is prepared by vortex mixing aqueous nanoparticle dispersions with $C_{12}E_4$ (above T_{ODT}), such that the surfactant-water ratio is kept constant at a ratio of 75 : 25. Here we use the following notation: L_α+ x% S15 indicates a sample with surfactant $C_{12}E_4$ and water in the ratio of 75 : 25, prepared using a x% aqueous dispersion of S15. Thus, for example, a sample of L_α+ 5% S15 will contain 3 parts by weight of $C_{12}E_4$, 1 part by weight of water, and 0.05 parts by weight of the S15 particles.

4.3 Results & Discussion

The L_α phase is identified using both SAXS and polarized optical microscopy (POM). Lamellar phases are characterized by structure factor peaks at q values in the ratio of $1:2:3:4$. In the normal configuration of our SAXS instrument, only the first order SAXS peak from the L_α phase can be observed, since the higher order peaks lie at q values higher than the range of our instrument. However, for selected L_α phase/Sx composite samples, we have confirmed the presence of the second order peak by moving the detector closer to the sample to increase the q range as shown in Figure 4.1. When we compare SAXS from the neat lyotropic lamellar phase with that from the L_α+ 5% Sx composites, we observe that there is no significant change in either the position or the width of the lamellar phase peak (Figure 4.2). We observe a first order Bragg peak at a q value of 0.13Å^{-1} corresponding to a bilayer repeat spacing of $d = 2\pi/q \approx 47.5\text{Å}$. Qualitatively similar SAXS is observed for composites with a higher nanoparticle loading (Figure 4.3). In this work, we focus on samples prepared from 5% Sx dispersions. We also note that the textures observed in the optical microscope between crossed polarizers (Figure 4.4) are characteristic of the L_α phase.

The L_α+Sx composites show a SAXS peak at low q, that is clearly absent in the dilute solution form factor of the corresponding particles, $P(q)$ (plotted, for convenience, as a dotted line next to SAXS from the composite, Figure 4.2). This SAXS low q peak appears at $q = 0.022\text{Å}^{-1}$, 0.036Å^{-1}, 0.057Å^{-1}, and 0.0775Å^{-1}, corresponding to length scales of $2\pi/q = 286\text{Å}$, 175Å, 110Å and 81Å for composites containing S26, S15, S11 and S8 particles, respectively. These length scales are comparable to the corresponding nanoparticle dimensions. In composites containing S26 and S15, the interparticle spacing is about 2nm larger than the particle size, while in the S11 and S8 composites, the interparticle spacing approximately equals the particle size. Therefore, we attribute the low q SAXS peaks to particle-particle correlations from regions of high particle concen-

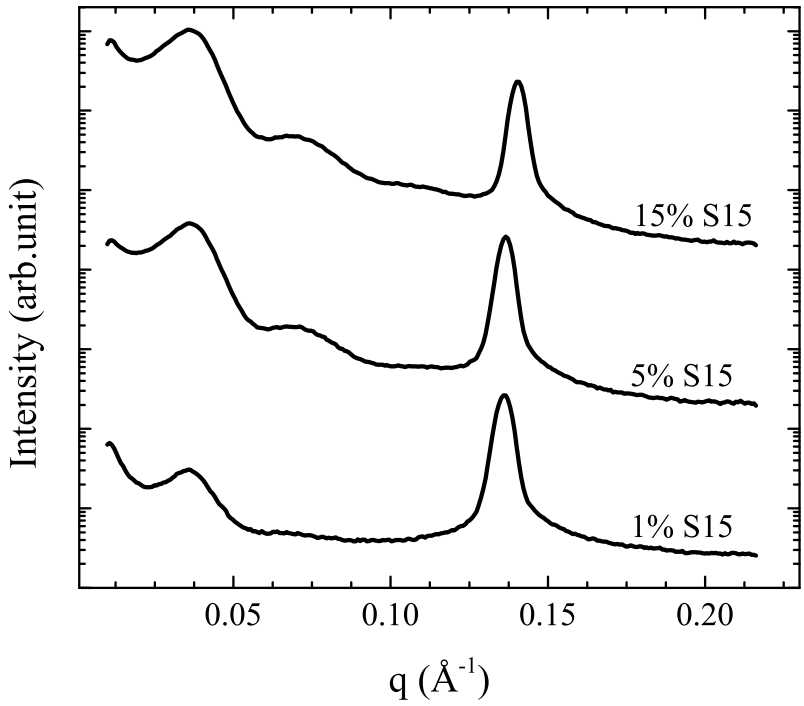

Figure 4.3: SAXS for the composites containing silica particles S15 (from bottom to top) at different concentrations starting from 1% to 15%.

tration in the composites. These particle–particle correlations are absent in the dilute aqueous dispersions of the nanoparticles. In previous work from our group[6,8] on silica nanoparticle/nonionic surfactant hexagonal phase (H_1) composites, we had observed similar particle–particle correlation peaks in the SAXS, corresponding to the nanoparticle size. There, we had demonstrated that the SAXS correlation peak arose from aggregation of nanoparticles at the boundaries of the hexagonal phase domains. Similarly, we believe that, in the case of the L_α+Sx composites too, the low q SAXS correlation peak arises from aggregation of the nanoparticles in the composites. Our interpretation of the low q SAXS peak is consistent with previous electron microscopy studies on similar systems.[14] Freeze fracture SEM of L_α+ 5% S15 reveals large irregular aggregates of the silica nanoparticles (Figure 4.5), essentially identical to data reported earlier.[14]

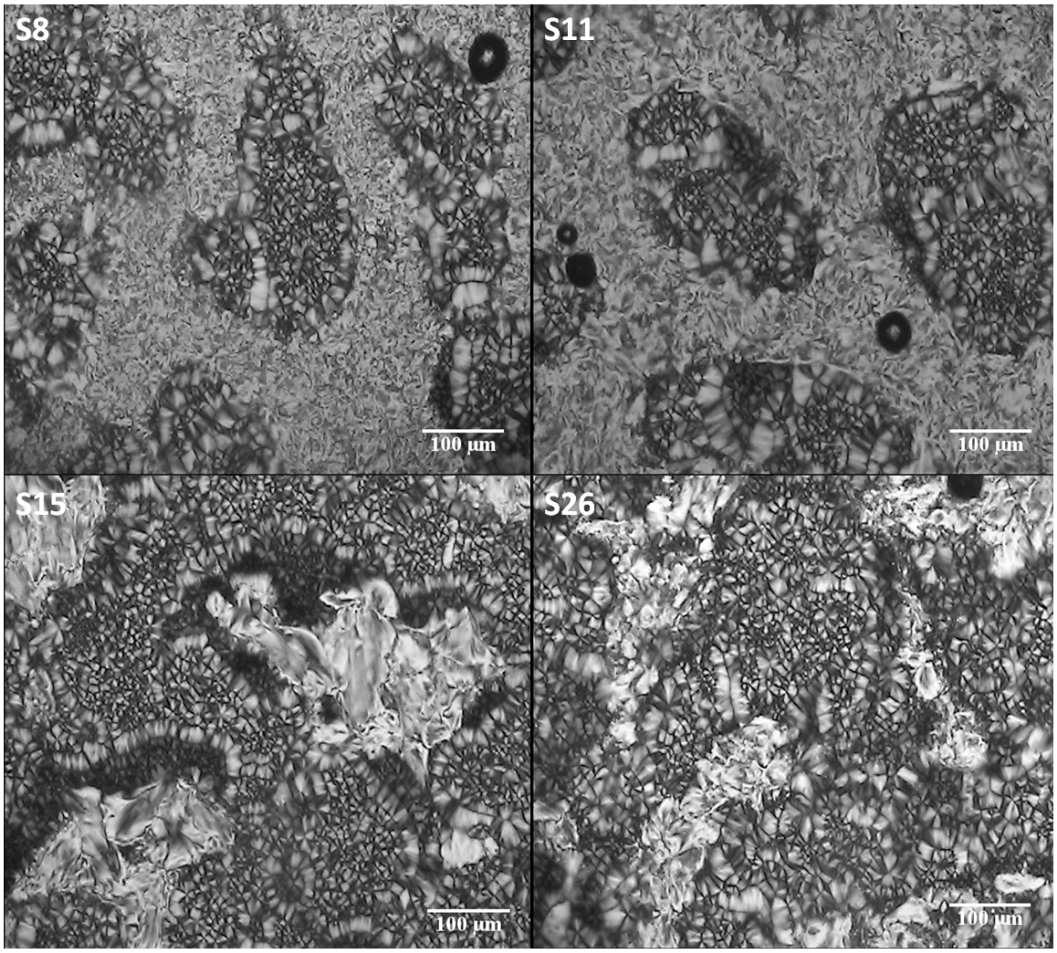

Figure 4.4: Polarized Optical microscopy image of the L_α+5% Sx phase between the crossed polarizers where x refers to 8, 11, 15 and 26 nm particles. The scale bar in the image represent 100µm

On heating above $T_{ODT} \approx 53°C$, the L_α phase transitions into a disordered surfactant liquid, indicated by the disappearance of the L_α structure factor peak at $q = 0.035Å^{-1}$ (Figure 4.6) and, of the POM textures characteristic of the L_α phase. The disordered phase is characterized by a broad peak around $0.127Å^{-1}$ in SAXS, and appears dark between crossed polarizers. Addition of silica nanoparticles to the $C_{12}E_4$/water system does not affect the lamellar phase T_{ODT}. For L_α+ 5% S15, the disappearance of the L_α structure factor peak above T_{ODT} correlates with the disappearance of the particle-particle correlation peak at low q (Figure 4.6a). Above T_{ODT}, the shape of the low q

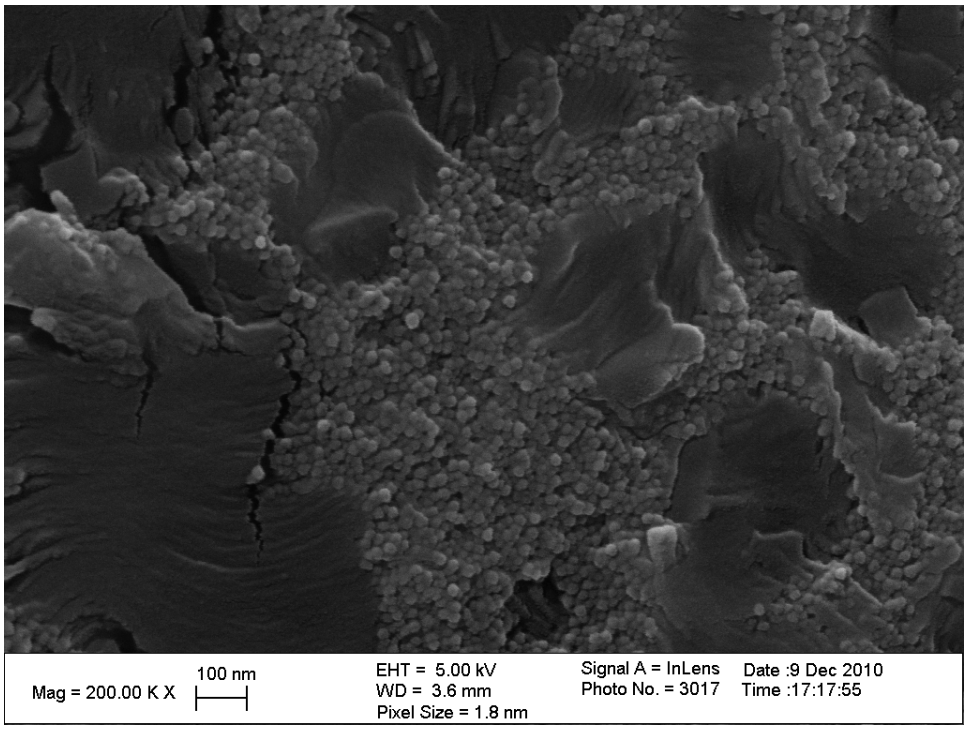

Figure 4.5: Freeze fracture SEM of L_α+ 5% S15 composites.

scattering from the S15 composite is similar to the dilute solution form factor, $P(q)$, of the S15 dispersion, indicating that the S15 particles are well dispersed on heating into the disordered surfactant phase. This change in the particle aggregation is reversible, and the particle correlation and L_α structure factor SAXS peaks reappear, on cooling below T_{ODT}. Similar behavior is also observed for L_α+5% S26. This reversible aggregation of the silica nanoparticles in the ordered L_α phase, and disaggregation in the disordered phase is similar to the behavior in the H_1/silica nanoparticle composites reported earlier by our group.[6]

On heating the L_α composites containing S8 and S11 particles above T_{ODT}, the low q peak arising from the particle-particle correlations does not disappear, unlike in the case of composites containing S15 particles (Compare Figure 4.6b with 4.6a; Figure 4.6c). Clearly, neither the position nor the intensity of this low q peak change with temperature for L_α+5% S11 (Figure 4.6b). Even on heating the $C_{12}E_4$/water/S11 composite up to

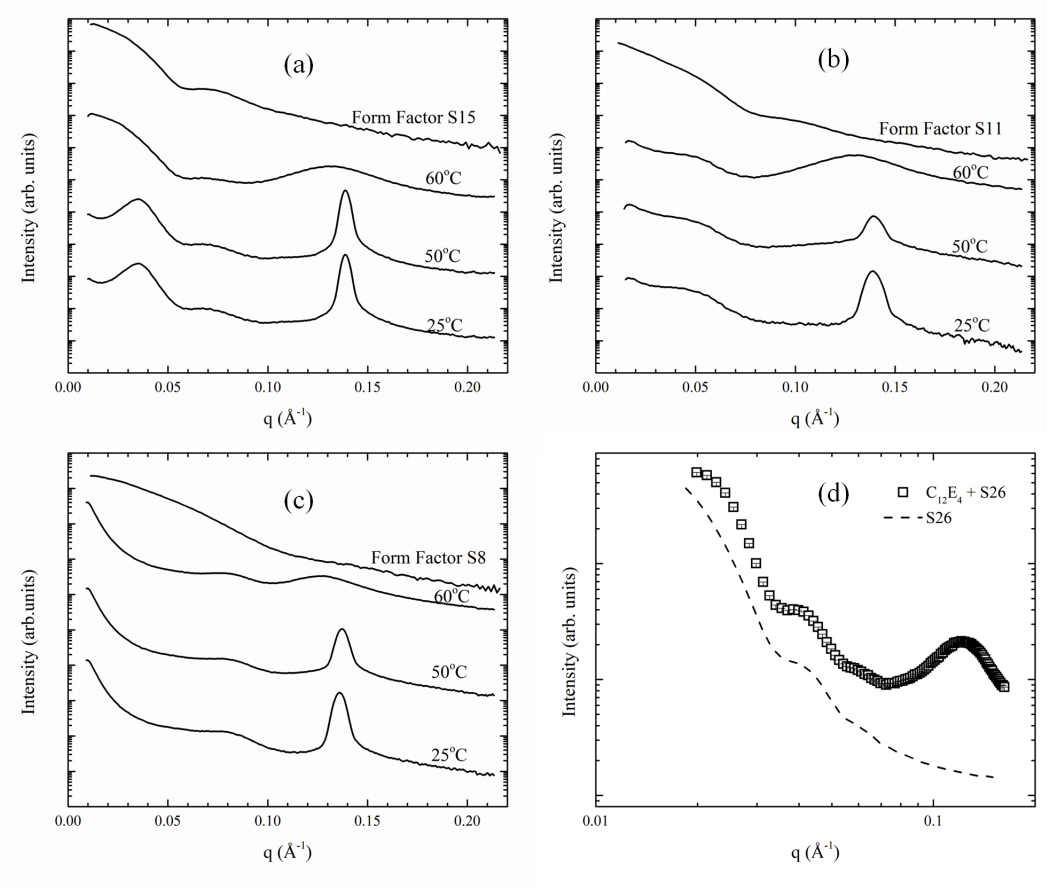

Figure 4.6: SAXS for the L_α phase with both S15 and S11 particles as a function of temperature and their optical micrographs. (a) SAXS for L_α + S15 particles at different temperatures (b) L_α + S11 particles (c) L_α + S8 particles (d) The SAXS data for mixing $C_{12}E_4$ and S26 at 60°C, well above the T_{ODT}.

80°C, the particle-particle aggregation peak persists, with no change in peak position or intensity (Figure 4.7). This clearly shows that there in no change in aggregation behaviour above and below T_{ODT}. Thus, our data suggest that S8 and S11 particles are irreversibly aggregated in the $C_{12}E_4$/water system, while S15 and S26 particles aggregate only below T_{ODT}, but are well dispersed above T_{ODT}.

To investigate the influence of the L_α phase on aggregation of the S8 and S11 particles, we performed the following experiment. $C_{12}E_4$ was mixed with aqueous 5% nanoparticle dispersions, of either S11 and S15, at 60°C ($> T_{ODT}$). These composite systems were examined using SAXS, *without* ever cooling the sample below T_{ODT}. The broad peak

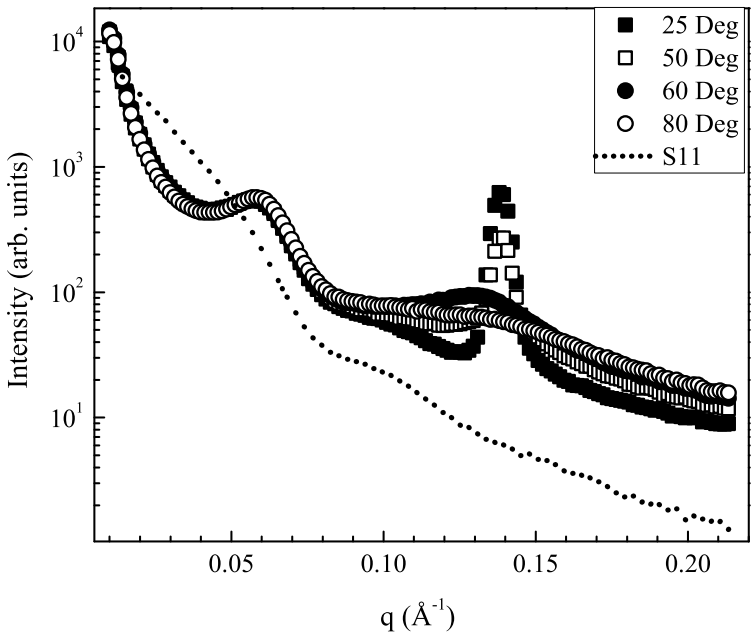

Figure 4.7: The particle–particle correlation peak low-q for the L_α phase containing 15% S11 particles at different temperatures remains unaltered both in intensity and position even after heating it well above the T_{ODT}.

from the disordered surfactant liquid centered around 0.127Å^{-1} is observed for both composites. At lower q, where the scattering comes predominantly from the particles, we observe that the scattering from the S15 composite is remarkably similar to the form factor of dilute S15 dispersions (plotted as a dotted line, for ease of comparison, Figure 4.8). In contrast, the low q scattering from the S11 composites is very different from the dilute solution form factor of the S11 dispersions (Figure 4.8, form factor of the S11 dispersions shown as a dotted line). We clearly observe a particle-particle correlation peak at $q = 0.057$Å^{-1} for the S11 composites. At lower q (< 0.057Å^{-1}), the scattering intensity shows a sharp upturn, indicating large scattering structures, that we believe, represent aggregates of several S11 particles. Thus, our data indicate that S15 and S26 (Figure 4.6a and 4.6d) silica nanoparticles aggregate only in the L_α phase, viz. below T_{ODT} and are well dispersed at higher temperatures; while S11 and S8 (Figure 4.6b and

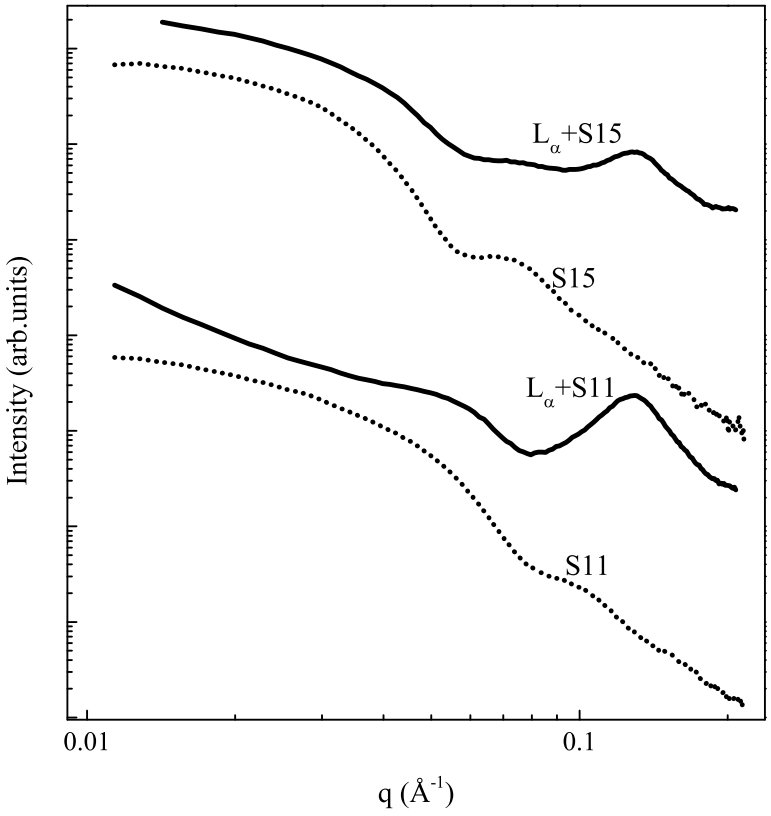

Figure 4.8: SAXS data for the L_α phase containing 5% of silica particles S15 and S11 when mixed at higher temperature 60°C. The figure clearly shows that the particles are aggregated for L_α+S11 even at higher temperature and the particles are dispersed in the case of L_α+S15. The dotted lines represent the form factor for the particles S11 and S15 which are plotted adjacent to it.

Figure 4.6c) silica nanoparticles aggregate on mixing with the 75/25 $C_{12}E_4$/water system. The S11 and S8 nanoparticles stay aggregated, both in the L_α phase, and above T_{ODT}.

We can obtain insight into the large length scale aggregate structures formed in the S8 and S11 composites, by examining the upturn in scattered intensity at low q, below the particle-particle correlation peak. We plot an apparent structure factor, $S_A(q) = \frac{I-I_S}{I_P}$, by subtracting the scattering from the surfactant liquid phase, I_S, from that from the $C_{12}E_4$/water/Sx composite at temperatures above T_{ODT}, I, and scaling by the scattering from a dilute Sx particle dispersion, I_P (Figure 4.9). Therefore, $S_A(q)$ is indicative of

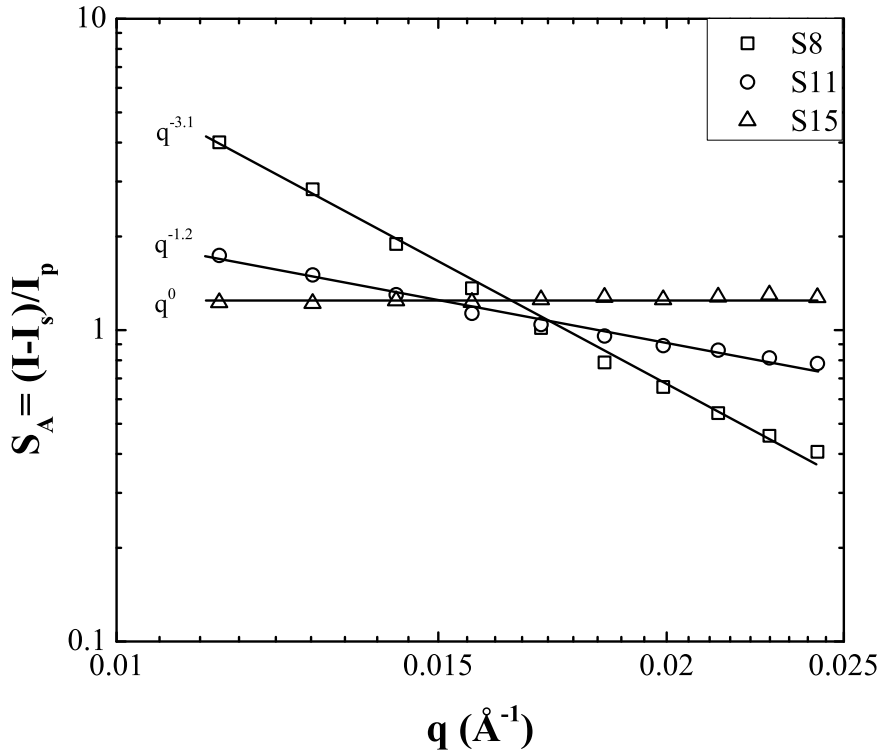

Figure 4.9: The apparent structure factor (defined in the text) for $C_{12}E_4$/water containing silica particles S8, S11 and S15. $S_A(q)$ scales as $q^{-3.1}$ for S8, $q^{-1.2}$ for S11 and q^0 for S15 particles.

the structure of the nanoparticle aggregates. For the S15 composite, the shape of the scattered intensity is similar to the particle form factor. Thus, $S_A(q) \approx 1$, independent of q (Figure 4.9), indicating that the particles are not aggregated. For the S8 and S11 composites, $S_A(q)$ increases strongly at low q. Over a limited q range from 0.01 to 0.02Å^{-1}, $S_A(q)$ scales as $q^{-3.1}$ and as $q^{-1.2}$ for the S8 and S11 composites, respectively.

Our results indicate that small silica nanoparticles, S8 and S11, aggregate irrversibly in a 75 : 25 $C_{12}E_4$/water system, while larger nanoparticles, S15 and S26, aggregate reversibly in the L_α phase and are dispersed above T_{ODT}. To understand this, we refer to the pioneering work of Levitz,[39,40] who described the adsorption of nonionic surfactants on hydrophilic silica surfaces. They demonstrated that micellization and adsorption are related, and showed that nonionic surfactants that had a high temperature micellar

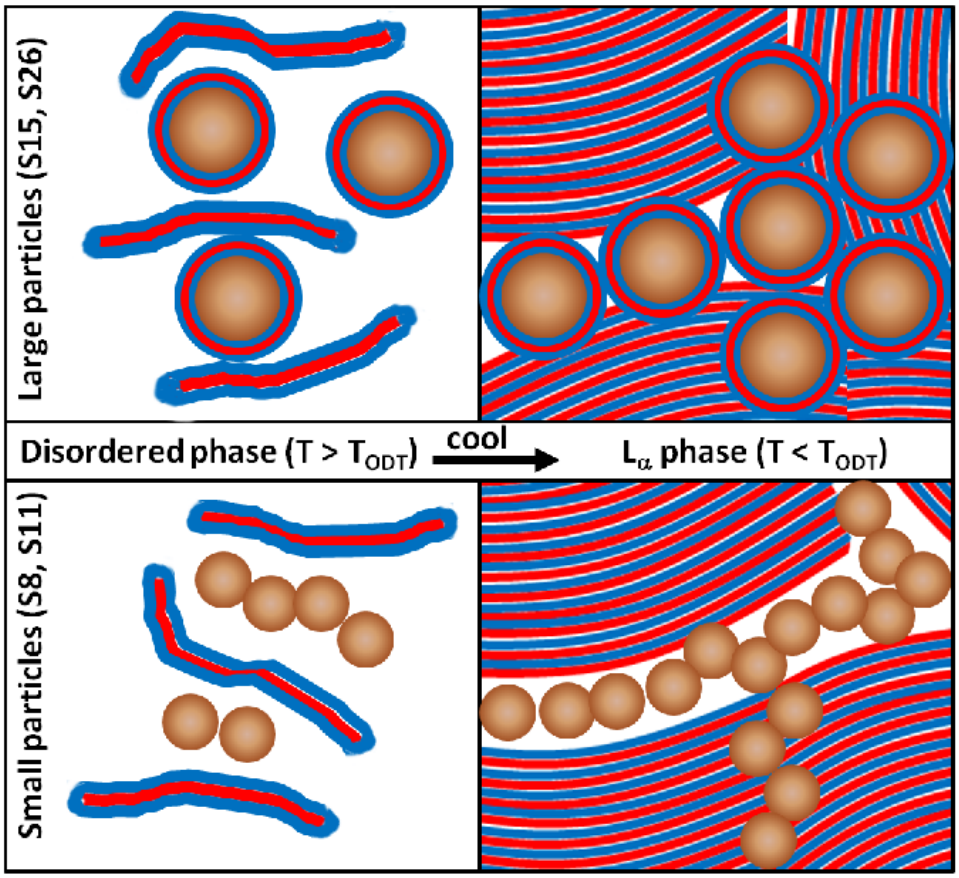

Figure 4.10: Schematic cartoon representing the difference in the aggregation behavior of the S11 and S15 particles when mixed with surfactant. The particles S15 are coated with bilayers around and are aggregated reversibly. The case for S11 is different since the bilayers are not coating on individual S11 particles. Thus they are irreversibly aggregated.

(L_1) phase, adsorbed as micellar aggregates on silica surfaces. In accord with this, our group and others, have observed that nonionics with large hydrophilic segments, such as Triton X-100[41] and $C_{12}E_9$,[7] form micellar structures (rather than bilayers) on the surface of silica nanoparticles. In previous work, we had demonstrated that the adsorption of such micellar structures of $C_{12}E_9$ rendered particle aggregation reversible, for silica nanoparticles with sizes from 8 to 500nm.[6] The key point to note here is that the $C_{12}E_9$ surfactant adsorbs as small micellar structures onto the silica, and is, therefore, able to adsorb onto even the highly curved surface of the S8 particles.

Levitz et. al. also demonstrated that nonionic surfactants with short hydrophilic

segments, such as the $C_{12}E_4$ used in this work, aggregate to form large structures on a silica surface, as well as large micellar aggregates in solution.[39,40] Recent work[42,43] has demonstrated that relatively hydrophobic surfactants with short hydrophilic segments, such as $C_{12}E_5$, adsorb as bilayers on flat silica surfaces,[44] but form small micellar aggregates when adsorbing onto 16nm silica nanoparticles. We note that while $C_{12}E_5$ has a high temperature micellar (L_1) phase, the surfactant used in our work, $C_{12}E_4$, forms a surfactant liquid (L_2) phase above T_{ODT}. On heating the 75 : 25 $C_{12}E_4$/water system investigated here above T_{ODT}, the layers comprising the L_α phase unbind[45] to form a surfactant liquid (L_2) phase. We contend that, in our work, large $C_{12}E_4$ structures that have a bilayer-like local structure, interact with the silica nanoparticle surface.

The reversible aggregation of the S15 and S26 particles in our $C_{12}E_4$/water experiments, suggest that these particles are stabilized by adsorbed surfactant bilayers. Based on the aforementioned literature,[39,40,42–44] it is plausible that the relatively hydrophobic $C_{12}E_4$ surfactant (that forms large solution structures and does not have a high temperature micellar phase), is unable to adsorb as small micellar structures on the nanoparticle surface, and instead adsorbs in the form of bilayers. For the smaller particles, S8 and S11, the high curvature precludes adsorption as bilayers. Therefore, the particles, left bare in the surfactant liquid, aggregate irreversibly (Figure 4.10). For a bilayer to wrap a nanoparticle, it has to bend around it. The bending energy per unit area of a membrane has been given by Helfrich[46] as:

$$E = \frac{1}{2}k_c\left(\frac{1}{R_1}+\frac{1}{R_2}\right)^2 + \overline{k}_c\left(\frac{1}{R_1R_2}\right) \tag{4.1}$$

where R_1 and R_2 are the principal radii of curvature (R_1, R_2 = nanoparticle radius, R); $k_c = 3.2k_BT$ is the bending modulus[47] and $\overline{k}_c$ is the saddle splay modulus. Thus, the bending energy scales as R^{-2}, so that the energy penalty for bilayer bending around S11 is about 4 times that for the S15. Thus, we speculate that $C_{12}E_4$ can form bilayers around

silica nanoparticles with a size of at least 15nm, but is unable to wrap around particles smaller than 11nm. Consistent with this claim, we note that in our L_α/nanoparticle composites, the interparticle spacing is about 2 nm larger than the particle size for the S15 and S26 composites, and is approximately equal to the particle size for the smaller (S8 and S11) particles.

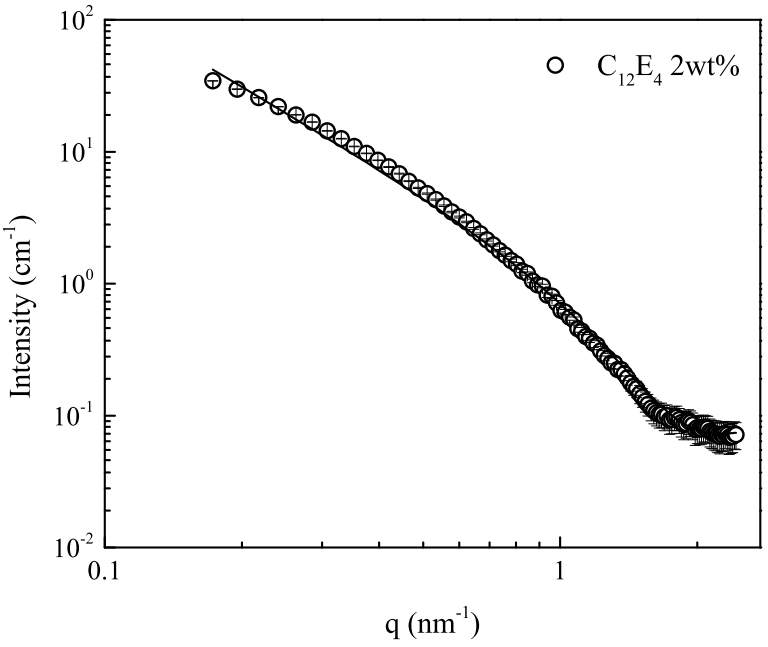

Figure 4.11: The SANS data for the $C_{12}E_4$ 2% in D_2O. The symbol represent the data point and the solid line represent the fit for the data.

Contrast matched SANS experiments provide direct evidence for the structure formed by the $C_{12}E_4$ surfactant when it interacts with the silica nanoparticles. Based on our hypothesis, we anticipate that S15 and S26 particles (but not the S8 and S11) are wrapped by surfactant bilayers. Therefore, if we adjust the water/D_2O ratio such that the silica is contrast matched with the solvent, we expect to see evidence for shell-like structures in the SANS data from the S15 and S26 composites, but not for the S8 and S11. Interpretation of silica contrast-matched SANS data from surfactant structures, at the high surfactant

concentrations where the L_α phase forms, is complicated as we have to account for the structure factor from interference between the surfactant structures. If, as we anticipate, there are surfactant shells as well as other large surfactant aggregate structures, we will need to invoke partial structure factors for interference between these structures. We have demonstrated earlier[7] that it is not possible to independently determine all these partial structure factors, even with contrast variation SANS experiments. Therefore, to simplify the analysis, we work at low concentrations of silica nanoparticles and surfactant. Specifically, we work at a concentration of 2% of the silica nanoparticles and 2% of the $C_{12}E_4$ surfactant in a 40/60 water/D_2O mixture, where the silica is contrast matched. As the silica is contrast matched, we observe SAN scattering from the hydrophobic C_{12} chains of the surfactant aggregates.

SANS from 2% solutions of the $C_{12}E_4$ surfactant in D_2O could not be fitted by models for spherical micelles. We observe that the $C_{12}E_4$ solution is not clear, suggesting that large length-scale surfactant aggregates are formed, in accord with previous literature.[39,40] We fit the SANS data assuming that the surfactant aggregates form flat cylinders and observe that the thickness value (= 2.8nm) obtained from this fit accords well with our expectations for the hydrophobic region of a $C_{12}E_4$ bilayer (Figure 4.11). As the surfactant concentrations are low, the SANS is fitted with the form factor for flat cylinders. We note that it is also possible to fit this data to a bilayer with a Gaussian density variation – however, the results obtained for the bilayer thickness are comparable to the more parsimonius flat cylinder model. Further, since the SANS data is plotted in absolute units, fitting to the flat cylinder model (cylinder diameter = 150nm, thickness of hydrophobic region = 2.8nm) allows us to calculate the total amount of surfactant in solution. This calculated quantity of surfactant closely matches with the experimental amount, supporting our choice of fitting model.

A qualitative difference is observed when we compare SANS from 2% $C_{12}E_4$ + 2%

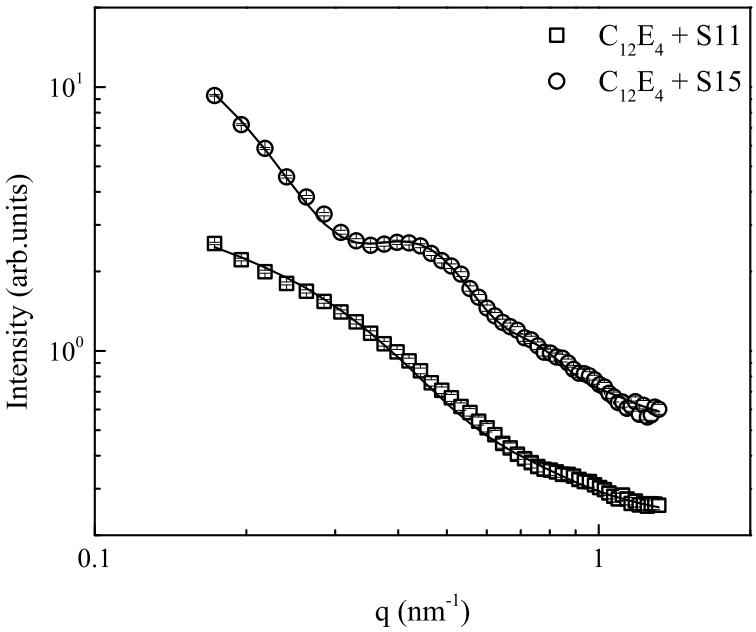

Figure 4.12: SANS data for the 2% $C_{12}E_4$+ 2% S11 and 2% $C_{12}E_4$+ 2% S15 with the silica contrast matched. There is a clear difference between the sample containing S11 and S15 particles as shown. The $C_{12}E_4$ forms a bilayer shell on the surface of the S15 particles.

S11, and 2% $C_{12}E_4$ + 2% S15 samples (Figure 4.12). As the solvent is contrast matched to the silica, SANS from the these samples, arises from the hydrophobic regions of the surfactant aggregates (since we assume that the hydrophilic parts are well solvated). Therefore, it is immediately obvious that there is a qualitative difference between the surfactant aggregate structures formed in the presence of the S11 and the S15 nanoparticles. Specifically, we observe a dip in the scattered intensity (near 0.3nm^{-1}): this feature is suggestive of the formation of shell-like structures. We now discuss the analysis of the SANS data from the samples in detail. As the surfactant concentrations used in these experiments are small, we assume that the scattering comes from dilute dispersions of surfactant aggregates and do not consider partial structure factors.

For the 2% $C_{12}E_4$ + 2% S11 sample, we observe that, as with the surfactant solution,

the SANS data cannot be fitted to models for spherical micelles. Fitting the SANS data from 2% $C_{12}E_4$ + 2% S11 to flat cylinders alone yields a poor fit a low q, indicating the presence of smaller scattering structures. Therefore, we fit this data to a combination of the form factor for flat cylinders, with the form factor for smaller oblate ellipsoidal structures. We observe that we are able to obtain a good fit to the data with flat cylinders (150nm diameter, 2.8nm thickness) and oblate ellipsoids (major axial radius of 8nm and minor axial radius of 1.44nm) at a number density of $5.13\times10^{13}/\text{cm}^3$ and $2.06\times10^{16}/\text{cm}^3$, respectively. Again, we note the thickness of the flat cylinder, and the thickness in the thin direction of the oblate ellipsoid (the minor axis diameter) are roughly consistent with the size expected for the hydrophobic region of $C_{12}E_4$ surfactant bilayers. Our data suggests that the surfactant aggregates are unable to coat the S11 particles. However, in the presence of the S11 particles, some of the micellar aggregates fragment to form smaller structures than the large disk like aggregates formed by the $C_{12}E_4$ in D_2O.

We observe qualitatively different SANS data for the 2% $C_{12}E_4$ + 2% S15 sample. We fit this data to a model comprising of surfactant shells and oblate ellipsoids. We are able to fit the data to shells with an inner radius of 8nm, and a thickness of about 2.9nm, and oblate ellipsoids (major axial radius of 4.7nm and a minor axial radius of 1.41nm) at number densities of $1.54\times10^{15}/\text{cm}^3$ and $1.15\times10^{17}/\text{cm}^3$, respectively. We note that the inner radius of the shell obtained from the fit is slightly larger than the radius of the S15 silica nanoparticle, and accounts for the size of the nanoparticle and the adsorbed hydrophilic part of the $C_{12}E_4$ surfactant. The thickness of the shell and the minor radius of the ellipsoid match with the size of the hydrophobic regions of the surfactant bilayer, and accord well with the values obtained for the fits to SANS data from the aforementioned samples. We note, in passing, that we have also performed SANS experiments where the water/D_2O concentration was adjusted to match the scattering length density of the surfactant. We obtain the size of the silica particles from such

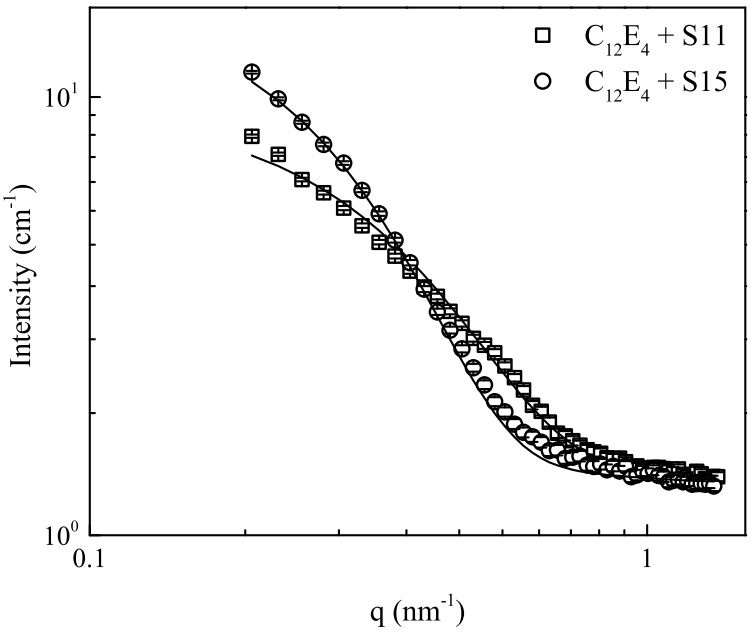

Figure 4.13: The SANS data for the $C_{12}E_4$ + S11 and $C_{12}E_4$ + S15 with solvent contrast matched with the surfactant.

experiments (Figure 4.13), that matches the form factor data from SAXS and is in accord with the value of the inner radius of the shell.

Therefore, our SANS data shows that, as hypothesized, the particle-surfactant interaction is dependent on particle size, and we see qualitatively different behavior for the S11 and S15 particles. The surfactants form large aggregates in aqueous solution, that we can model as flat cylindrical objects comprised of surfactant bilayers. These bilayers appear to interact with the silica particles. For the small (S11) particles, the bilayers are unable to coat the particles. Rather, some of them break up to form smaller aggregates (that we model as oblate ellipsoids). For the S15 particles, the bilayers coat the particles and can be modeled as shells in SANS, where the silica is contrast matched.

We also note that our interpretation is consistent with recent experimental work[3,36,48] that shows that the coating of nanoparticles by lipid membranes depends on their size.

Larger particles are readily coated, while smaller particles form pores in the membrane rather than getting coated,[3,36] in accordance with theoretical predictions[48] for membrane-nanoparticle interactions. We also note that our results are consistent with literature reports[14] that the stability of nanoparticle dispersions against aggregation depends on the extent of surface coverage by surfactant structures.

When the bilayer coated S15 and S26 particles are cooled from the L_2 phase into the L_α phase, they are expelled from the lamellar phase due to the elastic energy penalty for their inclusion in the mesophase (Figure 4.10). Therefore, they aggregate, as is evidenced by the particle correlation peak in SAXS at low q. However, on heating above T_{ODT}, they redisperse and the particle correlation peak disappears. S8 and S11 particles cannot be coated by the $C_{12}E_4$ bilayers. When these small nanoparticles are dispersed in the $C_{12}E_4$/water L_2 phase, they form large aggregate structures, that are observed as an upturn in the SAXS scattering at low q (Figure 4.9). The power law dependence of the apparent structure factor, $S_A(q) \sim q^{-n}$, suggests a fractal structure for these aggregates. However, given the limited range of q over which we observe the power law in $S_A(q)$, we are unable to comment unambiguously on the structure of the aggregates for the S8 and S11 nanoparticles. Finally, we comment briefly on the interparticle attraction that drives aggregation of S8 and S11. Preliminary evidence from our experiments suggest that the surface stabilizers for the commercial silica nanoparticles used in this work are solubilized by the $C_{12}E_4$/water system. Data to demonstrate this will be presented separately. Thus, bilayer coating of the S15 and S26 particles render them stable against irreversible aggregation. However, the bare S8 and S11 particles are destabilized and rapidly aggregate in the planar aqueous channels between the fluctuating $C_{12}E_4$ bilayers in the L_2 phase.

4.4 Conclusions

When silica nanoparticles are dispersed in a 75 : 25 $C_{12}E_4$/water system, we observe particle size dependent aggregation phenomena. Nanoparticles larger than about 15nm in size are excluded from the lamellar phase, and form large aggregates. This aggregation behavior is reversible and the nanoparticles redisperse above the lamellar phase T_{ODT}. However, particles smaller than about 11nm in size aggregate irreversibly, and stay aggregated both above and below the T_{ODT}. We believe that this is a consequence of the nanoparticle size dependence of nanoparticle/$C_{12}E_4$ bilayer interactions. We use contrast matched SANS experiments to demonstrate that an adsorbed surfactant bilayer forms on nanoparticles larger than about 15nm but not on 11nm particles or smaller, and argue that the the bending penalty for bilayers does not allow coating of particles smaller than about 11nm. Therefore, particles smaller than 11nm aggregate irreversibly, and larger (bilayer coated) particles aggregate only when they are excluded from the L_α phase, but are dispersed above T_{ODT}. While we report data only for $C_{12}E_4$/water/silica nanoparticle systems, we believe that our results might be more generally applicable to the interactions of relatively hydrophobic surfactants with attractive nanoparticles. If so, these results will have important implications for researchers who are investigating the structuring of nanoparticle assemblies in mesophases,[49] as well as for those who design nanoparticle based drug delivery systems that interact with bilayer cell walls.

References

[1] Hiemenz, P.; Rajagopalan, R. *Principles of Colloid and Surface Chemistry*; CRC, 1997; Vol. 14.

[2] Mezzenga, R.; Schürtenberger, P.; Burbidge, A.; Michel, M. *Nat. Mater.* **2005**, *4*, 729–740.

[3] Zhu, Z.-W.; Wang, Y.; Zhang, X.; Sun, C.-F.; Li, M.-G.; Yan, J.-W.; Mao, B.-W. *Langmuir* **2012**, *28*, 14739–14746.

[4] Gardner, D.; Evans, J.; Smalyukh, I. *Mol. Cryst. Liq. Cryst.* **2011**, *545*, 3–21.

[5] Horta, B. A. C.; de Vries, A. H.; Hünenberger, P. H. *J. Chem. Theory Comput.* **2010**, *6*, 2488–2500.

[6] Sharma, K. P.; Kumaraswamy, G.; Ly, I.; Mondain-Monval, O. *J. Phys. Chem. B* **2009**, *113*, 3423–3430.

[7] Sharma, K.; Aswal, V.; Kumaraswamy, G. *J. Phys. Chem. B* **2010**, *114*, 10986–10994.

[8] Venugopal, E.; Bhat, S. K.; Vallooran, J. J.; Mezzenga, R. *Langmuir* **2011**, *27*, 9792–9800.

[9] Imai, M.; Suganuma, Y.; Nakaya, K.; Komura, S. *J. Phys.: Condens. Matter* **2005**, *17*, S2929–S2935.

[10] Suganuma, Y.; Imai, M.; Nakaya, K. *J. Appl. Crystallogr.* **2007**, *40*, s303–s306.

[11] Fabre, P.; Casagrande, C.; Veyssie, M. *Phys. Rev. Lett.* **1990**, *64*, 539 – 542.

[12] Quilliet, C.; Fabre, P.; Cabuil, V. *J. Phys. Chem.* **1993**, *97*, 287–289.

[13] Ponsinet, V.; Fabre, P. *J. Phys. II France* **1996**, *6*, 955 – 960.

[14] Alexeev, V.; Ilekti, P.; Persello, J.; Lambard, J.; Gulik, T.; Cabane, B. *Langmuir* **1996**, *12*, 2392–2401.

[15] Raghunathan, V.; Richetti, P.; Roux, D.; Nallet, F.; Sood, A. *Mol. Cryst. Liq. Cryst.* **1996**, *288*, 181–187.

[16] Basappa, G.; Suneel,; Kumaran, V.; Nott, P.; Ramaswamy, S.; Naik, V.; Rout, D. *Eur. Phys. J. B* **1999**, *12*, 269–276.

[17] Salamat, G.; Kaler, E. W. *Langmuir* **1999**, *15*, 5414–5421.

[18] Bouchama, F.; Thathagar, M.; Rothenberg, G.; Turkenburg, D.; Eiser, E. *Langmuir* **2004**, *20*, 477–483.

[19] Caffrey, M. *Curr. Opin. Struct. Bio.* **2000**, *10*, 486–497.

[20] Cherezov, V.; Clogston, J.; Misquitta, Y.; Abdel-Gawad, W.; Caffrey, M. *Biophys. J.* **2002**, *83*, 3393–3407.

[21] Caffrey, M. *J. Struct. Bio.* **2003**, *142*, 108–132.

[22] Misquitta, L. V.; Misquitta, Y.; Cherezov, V.; Slattery, O.; Mohan, J. M.; Hart, D.; Zhalnina, M.; Cramer, W. A.; Caffrey, M. *Structure* **2004**, *12*, 2113–2124.

[23] Cherezov, V.; Clogston, J.; Papiz, M. Z.; Caffrey, M. *J. Mol. Bio.* **2006**, *357*, 1605–1618.

[24] Angelova, A.; Ollivon, M.; Campitelli, A.; Bourgaux, C. *Langmuir* **2003**, *19*, 6928–6935.

[25] Angelov, B.; Angelova, A.; Mutafchieva, R.; Lesieur, S.; Vainio, U.; Garamus, V. M.; Jensen, G. V.; Pedersen, J. S. *Phys. Chem. Chem. Phys.* **2011**, *13*, 3073–3081.

[26] Angelova, A.; Angelov, B.; Garamus, V. M.; Couvreur, P.; Lesieur, S. *J. Phys. Chem. Lett.* **2012**, *3*, 445–457.

[27] Angelov, B.; Angelova, A.; Papahadjopoulos-Sternberg, B.; Lesieur, S.; Sadoc, J.-F.; Ollivon, M.; Couvreur, P. *J. Am. Chem. Soc.* **2006**, *128*, 5813–5817.

[28] Amar-Yuli, I.; Aserin, A.; Garti, N. *J. Phys. Chem. B* **2008**, *112*, 10171–10180.

[29] Garti, N.; Hoshen, G.; Aserin, A. *Colloids Surf. B* **2012**, *94*, 36–43.

[30] Ganem-Quintanar, A.; Quintanar-Guerrero, D.; Buri, P. *Drug Dev. Ind. Pharm.* **2000**, *26*, 809–820.

[31] Sagalowicz, L.; Leser, M.; Watzke, H.; Michel, M. *Trend. Food Sci. Tech.* **2006**, *17*, 204–214.

[32] Guo, C.; Wang, J.; Cao, F.; Lee, R. J.; Zhai, G. *Drug Disc. Today* **2010**, *15*, 1032–1040.

[33] Ramos, L.; Fabre, P.; Dubois, E. *J. Phys. Chem.* **1996**, *100*, 4533–4537.

[34] Terentjev, E. M. *Sov. Phys. - Crystallogr.* **1986**, *33*, 637 – 640.

[35] Zapotocky, M.; Ramos, L.; Poulin, P.; Lubensky, T. C.; Weitz, D. A. *Science* **1999**, *283*, 209–212.

[36] Roiter, Y.; Ornatska, M.; Rammohan, A.; Balakrishnan, J.; Heine, D.; Minko, S. *Nano Lett.* **2008**, *8*, 941–944.

[37] Kohlbrecher, J. SASfit version 2013-04-13 by Laboratory for Neutron Scattering. 2013.

[38] Mitchell, D.; Tiddy, G.; Waring, L.; Bostock, T.; McDonald, M. *J. Chem. Soc., Faraday Trans. 1* **1983**, *79*, 975–1000.

[39] Levitz, P.; Van Damme, H.; Keravis, D. *J. Phys. Chem.* **1984**, *88*, 2228–2235.

[40] Levitz, P.; Van Damme, H. *J. Phys. Chem.* **1986**, *90*, 1302–1310.

[41] Oberdisse, J. *Phys. Chem. Chem. Phys.* **2004**, *6*, 1557–1561.

[42] Lugo, D.; Oberdisse, J.; Karg, M.; Schweins, R.; Findenegg, G. *Soft Matter* **2009**, *5*, 2928–2936.

[43] Bharti, B.; Meissner, J.; Gasser, U.; Findenegg, G. H. *Soft Matter* **2012**, *8*, 6573–6581.

[44] Tiberg, F. *J. Chem. Soc., Faraday Trans.* **1996**, *92*, 531–538.

[45] Lipowsky, R.; Leibler, S. *Phys. Rev. Lett.* **1986**, *56*, 2541–2544.

[46] Helfrich, W. *Z. Naturforsch* **1973**, *28c*, 693–703.

[47] Kurtisovski, E.; Taulier, N.; Ober, R.; Waks, M.; Urbach, W. *Phys. Rev. Lett.* **2007**, *98*, 258103.

[48] Lipowsky, R.; Döbereiner, H.-G. *Eur. Phys. Lett.* **1998**, *43*, 219.

[49] Gaikwad, A.; Verschuren, P.; van der Loop, T.; Rothenberg, G.; Eiser, E. *Soft matter* **2009**, *5*, 1994–1999.

Chapter 5

Structure and dynamics of concentrated polyelectrolyte solutions in presence of nonionic surfactants

Contents

5.1 Introduction

Surfactant-polyelectrolyte complexes are commonly encountered in pharmaceutical formulations, personal care products, in waste water treatment, and in molecular biology.[1–7] Specifically, such complexes are of use in formulations for extended delivery of hydrophobic actives or flavor/perfume compounds. The delivery of a specific compound to a target surface depend on several parameters that determine the affinity of the compound or carrier complex to the surface. Polyelectrolytes can be polyanionic or polycationic and adsorb onto oppositely charged surfaces.[8] The adsorption of polyelectrolytes onto different surfaces has been extensively investigated.[8–11] In applications such as hair care, fabric care, etc. functionality is obtained by depositing oppositely charged polyelectrolyte/surfactant complex on a solid surface.[1,2,6] In oral care applications, hydrophobic polyelectrolytes such as alternating copolymer of maleic acid and vinyl alkyl ethers (that are available under the trade name of Gantrez) are strongly adsorbed on the oral mucosa. Such polymers are also known to possess anti-gingivitis properties[12,13] and have hydrophobic domains that are sufficiently large to accommodate flavour compounds and hydrophobic materials.[14–19] It is of interest to develop novel delivery systems to deliver antibacterials, active compounds, etc. in oral care applications based on complexes of Gantrez with surfactants. In oral care applications, hydrophobic actives and flavor compounds are often sub-optimally used since they are rinsed away during use.[2] Therefore, effective targeted delivery of such hydrophobic compounds remains challenging. The development of carrier complexes that can target oral cavities and deliver hydrophobic cargo molecules for an extended period of time is,[20] therefore, of great practical importance.

Such formulations need to meet several criteria, including structural stability in aqueous media with variation of pH and ionic strength. Association of a polyelectrolyte with surfactant is known to alter solution rheology and result in polymer conformational transitions.[3,21–30] For example, complexes maleic acid based alternating copolymers with

cationic surfactants are prone to precipitation, depending on the ratio of surfactant to polymer. Other formulations have kinetically stable structures. Thus, a detailed knowledge of the structure and stability of polymer-surfactant complexes is desirable for design of formulations. While the structure of polyelectrolyte/nonionic surfactant mixtures have been reported by several groups,[1,2,6,24,28,31–35] these studies are restricted to low concentration formulations.

In this chapter, we present the behavior of polyelectrolyte/nonionic surfactant system at variable concentrations. We use a wide variety of experimental probes of structure, including cryo-TEM, static and dynamic light scattering of visible laser light and small angle X-ray scattering to provide insights into the structure of the polyelectrolyte/surfactant complexes used. Based on our data, we propose a model for the system.

5.2 Experimental Details

5.2.1 Materials

An alternating copolymer of (PMAVME) maleic acid (MA) and vinyl methyl ether (VME), was donated by ISP Technologies (UK) Limited, and is used as received. We refer to this polymer as PMAVME. PMAVME has a molceular weight of $M_w = 1200$kg/mol, based on the information provided by the manufacturer. Non-ionic surfactant nonaethylene glycol monododecyl ether ($C_{12}E_9$) is purchased from Sigma-Aldrich and is used as received. Distilled de-ionized water with a resistivity of 18.2MΩcm was used for all experiments.

5.2.2 Sample Preparation

To prepare solutions of PMAVME in water, polymer of required weight is dispersed in deionized water and gently stirred for 24h. Surfactant $C_{12}E_9$ is added to this poly-

mer solution and is mixed by vortexing. The mixture is placed in an ultrasonication bath for 3h to yield a solution of the PMAVME–$C_{12}E_9$ complex in water. We use the PMAVME:$C_{12}E_9$ ratios of 10 : 1 to 1 : 1 and most of this work focuses on complexes of 1 : 1 PMAVME:$C_{12}E_9$. Samples are identified using the following notation. 5% PMAVME means that the solution contains 5 parts (by weight) of PMAVME and 95 parts of water. 5% PMAVME:$C_{12}E_9$ means the sample contains 5 parts (by weight) of PMAVME polymer, 5 part of surfactant $C_{12}E_9$ and 90 parts of water in solution.

5.2.3 Methods

Turbidity

Turbidity was measured using a home-built setup using a 5mW He-Ne laser (Melles Griot) and a silicon photodiode detector (Thor Labs). Turbidity measurements were performed on samples taken in a square cuvette with a 9mm path length.

Cryo-TEM

The cryo-TEM experiments were performed at Technion (Israel Institute of Technology, Israel) in collaboration with the group of Prof. Yeshayahu Talmon. Samples were prepared in a Controlled Environment Vitrification System (CEVS). A drop of solution was placed on a TEM grid covered by a holey carbon film. The drop was then blotted with a filter paper to form a thin liquid film on the grid, and the grid was immediately plunged into liquid ethane at its freezing temperature. The images shown here are obtained using dilute concentrations ($< 0.625\%$).

Viscometry

Dynamic viscosity measurements were performed using an Ostwald viscometer with water as the reference liquid. All viscosity measurements were performed at 20°C. Par-

ticular care was taken to avoid formation of bubbles.

Light Scattering

Light scattering experiments were done on a goniometer based multi angle 3D-Dynamic Light Scattering instrument from LS Instruments, Switzerland. A He-Ne laser with a wavelength of 632.8nm is used as the source and two Avalanche Photodiodes are used as detectors with a digital correlator controlled by a LabView interface. Sample is taken in a cylindrical cuvette of uniform wall thickness 1mm (Fisher Scientific) that is kept in a vat of HPLC grade toluene for refractive index matching. The cuvettes were cleaned using HPLC grade methanol filtered through 0.22µm Millipore filter and were subsequently dried in a dust free chamber. The temperature of the bath is kept constant to within ± 0.1°C using a water circulator and all samples were prepared in a dust free environment. All the samples used were prepared with deionized water filtered using a 0.22µm filter.

Dynamic light scattering (DLS) experiments were performed in auto-correlation mode from 60° to 120° with an interval of 15°. The magnitude of the scattering vector q is related to the angle by

$$q = \left(\frac{4\pi n}{\lambda}\right) \sin\left(\frac{\theta}{2}\right) \tag{5.1}$$

where n being the refractive index of the medium, λ being the wavelength of the laser used, and θ being the scattering angle. Data was acquired for 180s at each angle to determine the autocorrelation function.

Toluene is used as reference and water as background in static light scattering (SLS) from 15° to 135° with an interval of 5° between each angles. The obtained data is averaged over 10 runs and is converted to absolute intensity by scaling with excess Rayleigh ratio of toluene after background subtraction.

CONTIN Algorithm

The measured autocorrelation function $g^{(2)}(\tau)-1$ is related to the field correlation function by the Siegert relation:[36]

$$g^{(2)}(\tau) = 1 + B|g^{(1)}(\tau)|^2 \tag{5.2}$$

where B is an instrumental constant. When τ is polydisperse, the field autocorrelation function is an integration over the relaxation time distribution $f(\tau)$ as

$$g^{(1)}(\tau) = \int_0^\infty f(\tau_1)\exp(-\tau/\tau_1)d\tau_1 \tag{5.3}$$

where τ_1 is related to the diffusion constant D by

$$\frac{1}{\tau_1} = D\left[\frac{4\pi n}{\lambda}\sin\left(\frac{\theta}{2}\right)\right]^2 \tag{5.4}$$

where λ is the wavelength of the laser, n is the refractive index, and θ is the scattering angle.

Equation 5.3 is represented in discrete form as

$$g^{(1)}(\tau_i) = \sum_{j=1}^{N}\exp(-\tau_i/\tau_j)f(\tau_j) \tag{5.5}$$

In matrix form,

$$g_i^{(1)} = H_{ij}f_j \tag{5.6}$$

where H_{ij} is the transfer matrix defined as

$$H_{ij} = \exp(-\tau_i/\tau_j)$$

Equation 5.6 is solved using non-negative least squares (NNLS) algorithm. But, this method is very sensitive to the noise in the input data. This is addressed by using Tikhonov regularization method where, an identity matrix L and a regularization parameter α are introduced as follows.

$$\min(||H.f - g^{(1)}||^2 + \alpha||L.g^{(1)}||^2) \tag{5.7}$$

This equation is solved by a numerical method to get $f(\tau)$. The regularization parameter α plays an important role in the resolution of the relaxation time spectra $f(\tau)$. For very low value of α, the spectra is bound-free and for very high α values, the distribution is very broad and no fitting. Thus, the value of α has to be chosen carefully in order to get sensible results. So it is a good practice to run the program for multiple values of α and choose the result accordingly.

Small Angle X-ray Scattering (SAXS)

SAXS experiments were done on a Bruker Nanostar with a rotating anode source and three pinhole collimation. The instrument uses Cu K_α radiation of wavelength 1.54Å and has a sample to detector length of approximately 105cm. The anode is operated at potential difference of 45kV and current of 100mA. The PMAVME complexes are aqueous dispersions and are loaded in a quartz capillary of 2mm thickness and 10µm wall thickness. Scattering from a glassy carbon film was taken as the reference. A Peltier unit is used for temperature control of the sample holder. Data is collected using a HISTAR gas filled multi-wire detector and the 2D data is circularly averaged to reduce to 1D. Samples were scanned for sufficiently long to get at least 2 million counts and the data is presented after normalizing with the transmission coefficient of the sample and the scan time.

5.3 Results

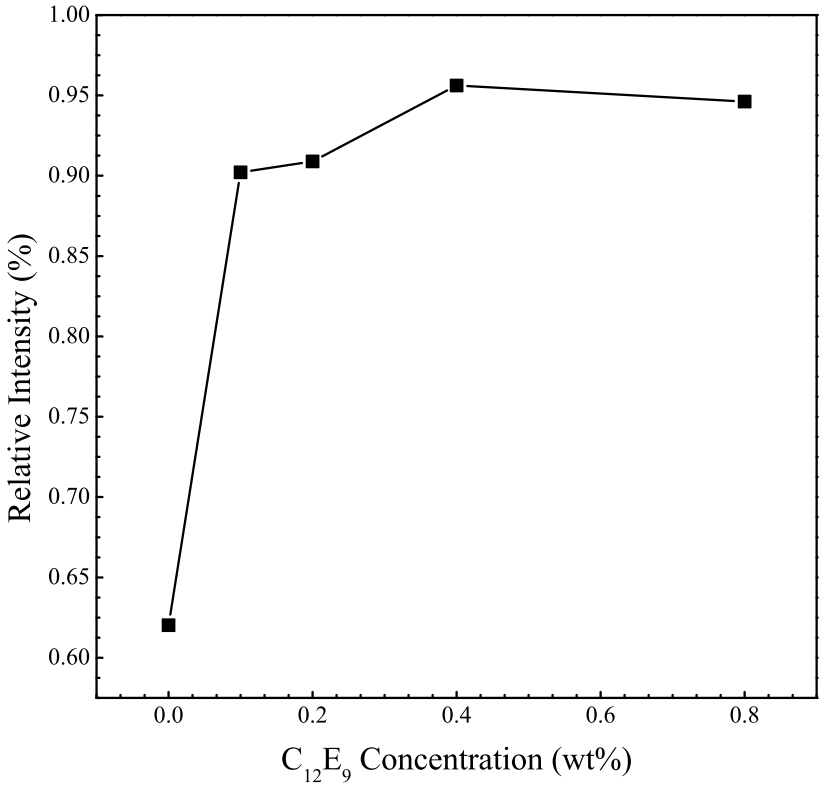

Figure 5.1: Turbidity of the neat PMAVME solution is plotted as relative intensity of transmission and surfactant concentration. Here the PMAVME concentration is 1% in total solution.

Aqueous solutions of PMAVME are turbid even at concentrations as low as 1%(w/v) and the intensity of light (HeNe laser light $\lambda = 632.8$nm) transmitted through a 9mm sample path length is 60%. The solution becomes substantially less turbid on addition of nonionic surfactant $C_{12}E_9$ (Figure 5.1). On addition of 0.1% $C_{12}E_9$, the intensity transmitted through the sample increases to 85% (Figure 5.1). With further addition of surfactant, the transmitted intensity increases and saturates at $\approx 95\%$ above a surfactant

concentration of 0.4%. In the rest of this work, we investigate aqueous samples containing 1 : 1 PMAVME : $C_{12}E_9$.

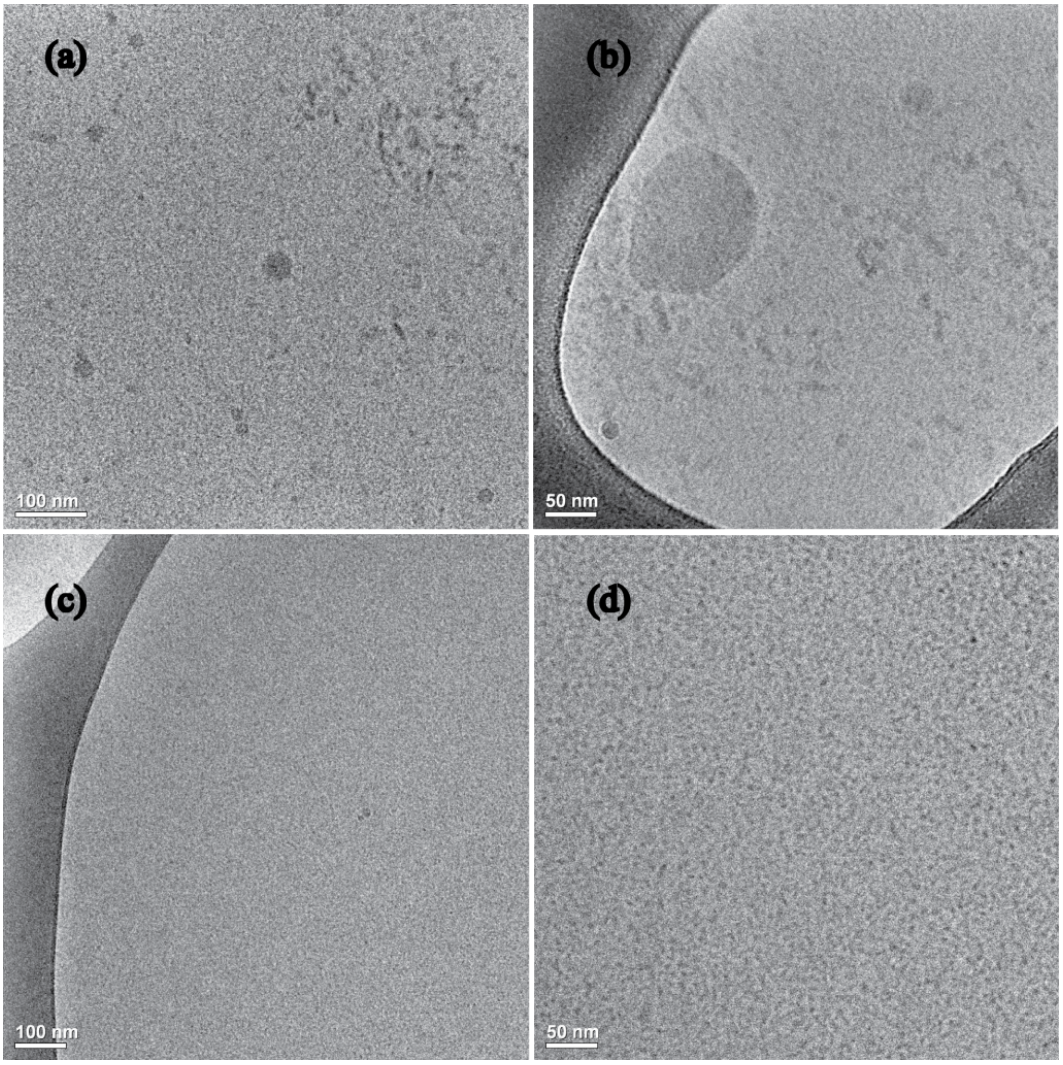

Figure 5.2: Cryo-TEM image of the dilute neat PMAVME solution(a & b) and dilute PMAVME:$C_{12}E_9$ solution (c & d).

Cryo-TEM was performed on highly dilute dispersions of PMAVME and the 1 : 1 PMAVME : $C_{12}E_9$ complex. We observe large ∼O(100nm) aggregate structures in the PMAVME dispersions (Figure 5.2a & 5.2b). We note that the observation of large aggregates is consistent with the strong scattering observed in the turbid 1% PMAVME dispersions. In contrast, the 1 : 1 PMAVME : $C_{12}E_9$ samples show smaller scale struc-

tures, characterized by a size ∼O(10nm) (Figure 5.2c & 5.2d). Thus, complexation of the PMAVME with $C_{12}E_9$ surfactant breaks up the large aggregates of the relatively hydrophobic polymer and results in the formation of smaller ∼O(10nm) structures. We note that the intensity of light scattered by a dispersion, I, scales very strongly with the size of the scatterer, r ($I \sim r^6$). Therefore, the reduction in the size of the aggregate structure on complexation of $C_{12}E_9$ with PMAVME is consistent with the decrease in turbidity observed on addition of the $C_{12}E_9$ surfactant to aqueous PMAVME dispersions.

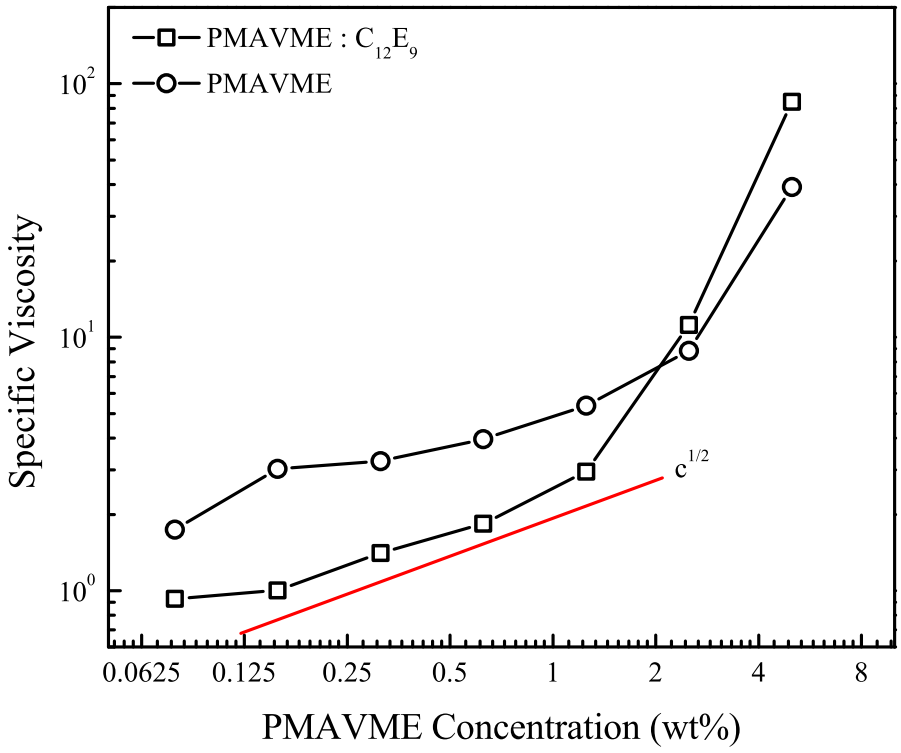

Figure 5.3: Relative viscosity of PMAVME dispersion and PMAVME:$C_{12}E_9$ dispersion as a function of PMAVME concentration.

We now examine the specific viscosity of dispersions of the PMAVME and the 1 : 1 PMAVME:$C_{12}E_9$ complex (Figure 5.3). We observe that the addition of the surfactant reduces the viscosity of the PMAVME solution by a factor of 2, for concentrations up to

1.25% (Figure 5.3). Thus, an aqueous dispersion containing 1.25% PMAVME and 1.25% $C_{12}E_9$, for example, has a two-fold lower viscosity relative to a dispersion containing 1.25% PMAVME alone. At these lower concentrations, the specific viscosity of the PMAVME and 1 : 1 complex dispersions approximately scales with $c^{\frac{1}{2}}$. For concentrations above 1.25%, the specific viscosity of the PMAVME:$C_{12}E_9$ complex increases rapidly, when compared with PMAVME dispersions. The specific viscosity of the complex is marginally higher than the PMAVME dispersion for a concentration of 2.5%, and significantly higher at a concentration of 5%. Thus, there appears to be a qualitative change in the behaviour of the aqueous dispersion of the PMAVME:$C_{12}E_9$ complex near a concentration of 2.5%.

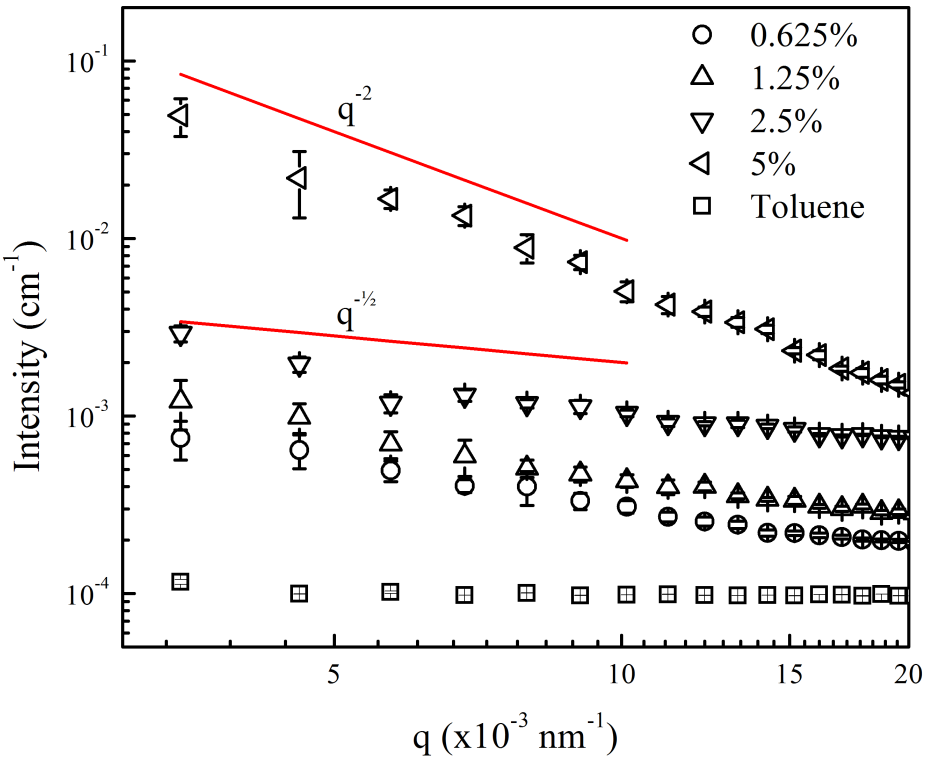

Figure 5.4: SLS data of the PMAVME:$C_{12}E_9$ solution is plotted for different concentrations. The reference plot using toluene is also given for comparison.

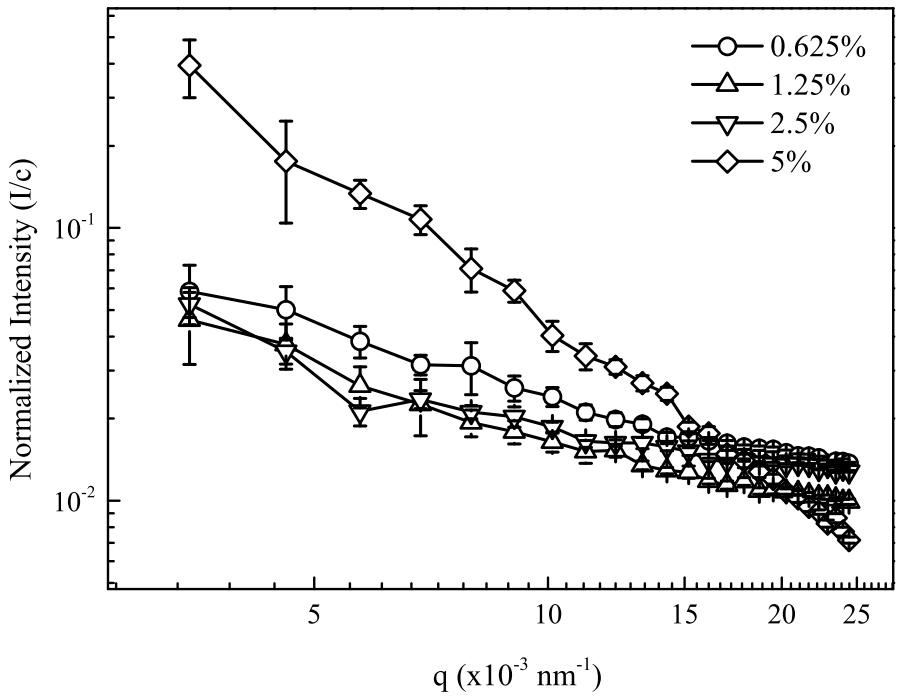

Figure 5.5: The SLS data is scaled with sample concentration.

We use static and dynamic scattering measurements using visible laser light radiation and small angle X-ray scattering to probe the structure of the PMAVME:$C_{12}E_9$ complex, as a function of concentration. We start by presenting data from static light scattering experiments. Data is presented in absolute intensity units for aqueous dispersions of the complex at concentrations from 0.625% to 5% (Figure 5.4). We observe that the scattered intensity varies as $q^{-0.5}$ for concentrations up to 2.5%. The intensity data collapses on scaling with sample concentration, for concentrations up to 2.5% (Figure 5.5). However, there is a qualitative difference in the scattered intensity for the 5% sample (Figure 5.4), where a q^{-2} scaling is observed.

Next, we present time autocorrelation functions $g^2(\tau)-1$ of the 1 : 1 PMAVME–$C_{12}E_9$ complexes obtained from dynamic light scattering experiments at 90° (Figure 5.6). As the correlation function appears to show a two-stage decay, we first attempted to fit these

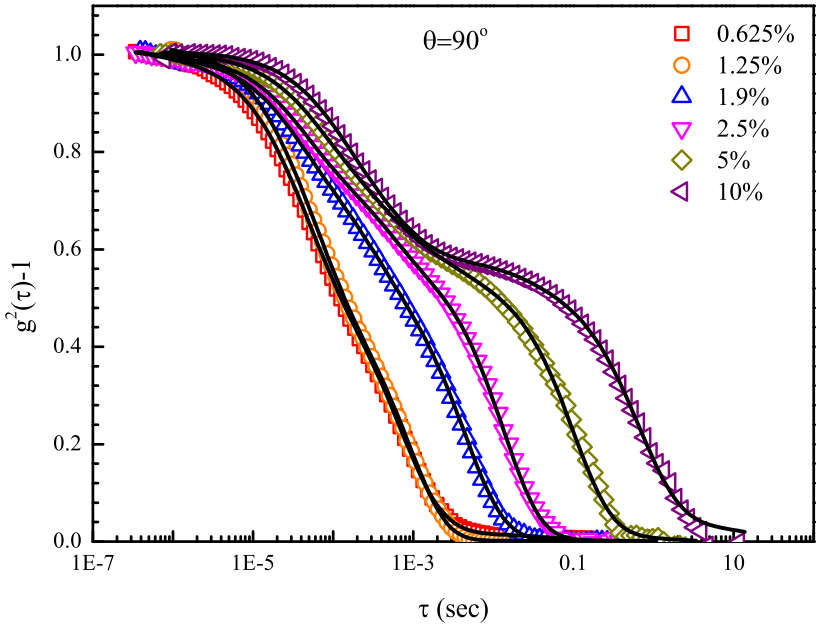

Figure 5.6: Autocorrelation functions of PMAVME–$C_{12}E_9$ solutions obtained from DLS at 90° angle. The black line is the fit obtained by the CONTIN analysis.

to a combination of stretched exponentials. Thus we fitted $g^2(\tau) - 1$ to an expression of the form

$$g^2(\tau) - 1 = b\left[a\exp\left(-\left(\frac{\tau}{\tau_f}\right)^{\beta_f}\right) + (1-a)\exp\left(-\left(\frac{\tau}{\tau_s}\right)^{\beta_s}\right)\right]^2 \tag{5.8}$$

where a, b are constants, τ_f, τ_s are relaxation times and β_f, β_s are stretching parameters. The premultiplication factor b is used to get rid of any instrumental decorrelation at very low τ values. The fit parameters for the data are given in the Table 5.1. We observe that there is no systematic trend with concentration for either the contribution of the fast relaxation mode, a, or for the stretch parameters. Thus, fitting the data with a phenomenological model does not yield physically meaningful parameters for interpretation.

Therefore, we employed the CONTIN algorithm to analyze the correlation functions from DLS. The algorithm we have used is based on the work of S. Provencher emulated

Conc (wt%)	a	b	τ_f	τ_s	β_f	β_s
0.625	0.32	0.96	3.2E-5	4.17E-4	0.855	0.75
1.25	0.26	0.97	4.35E-5	9.16E-4	0.852	0.76
1.9	0.19	0.998	9.12E-5	0.0046	0.68	0.74
2.5	0.15	0.995	9.33E-5	0.020	0.665	0.67
5	0.22	1.015	2.74E-4	0.097	0.62	0.797
10	0.19	1.009	3.00E-4	1.41	0.70	0.69

Table 5.1: Table showing the fit parameters of the correlations functions with double stretched exponential function.

into MATLAB by Dr. Iari-Gabriel Marino and that we have modified for use with the data formats from our instrument. The analysis program requires manual selection of a regularization parameter. We vary the regularization parameter from small to large values and select an appropriate value for each data set by manually inspecting the distributions and the fit to the data.

At concentrations of 0.625% and 1.25%, the autocorrelation functions are fitted with a bimodal distribution of relaxation times, with a fast mode τ_f centered around 5×10^{-4}s and a slower mode τ_s centered at 2×10^{-3}s (Figure 5.7). With increase in concentration, the time scale τ_s, associated with the slow mode shifts to significantly higher values. τ_s increases by three orders of magnitude, from O(10^{-3}s) for 0.625% PMAVME–$C_{12}E_9$, to O(1s) for a concentration of 10%. Further, a good fit to the data is no longer possible with a bimodal distribution of relaxation times. For concentrations of 1.9% and 2.5%, we observe two fast modes (τ_{f1} and τ_{f2}), in addition to the slow mode. At higher concentrations (5% and 10%), the fast modes are characterized by a very wide distribution that we represent using three fast modes. At all concentrations, the amplitude of the fast modes is much lower than the slow mode. This becomes more pronounced with increase in concentration. However, the position of the fastest mode τ_{f1} varies only modestly with concentration when compared to the slow mode.

For concentrations of up to 2.5%, where the fastest mode is characterized by prominent well defined peaks, we examine the dependence of $1/\tau_{f1}$ with q^2 (Figure 5.8). We

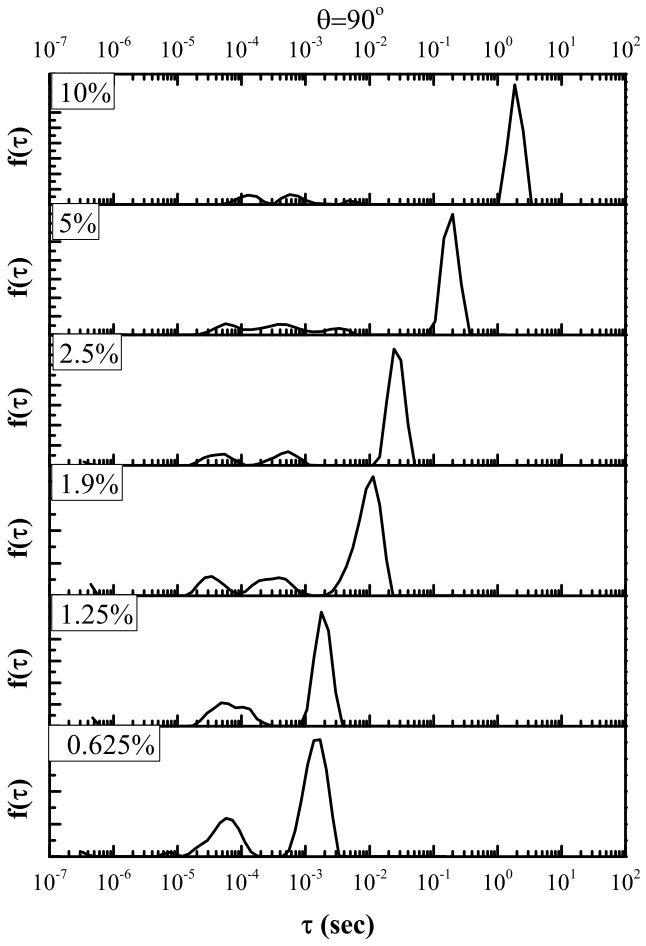

Figure 5.7: Relaxation time spectrum obtained from CONTIN analysis of DLS correlation functions taken at 90° angle.

also examine the dependence of $1/\tau_s$ with q^2. (Figure 5.9). Both $1/\tau_{f1}$ and $1/\tau_s$ scale with q^2.

We employ SAXS to determine the microstructure of PMAVME and 1 : 1 complex dispersions (Figure 5.10). There is a qualitative change in the SAXS pattern when PMAVME complexes with $C_{12}E_9$ surfactant (Figure 5.10a). Specifically, one observes the emergence of a SAXS peak at high q (above 0.1Å^{-1}) for the PMAVME:$C_{12}E_9$ complex that is not present for the PMAVME dispersion (data for 5% dispersions in Figure 5.10a). Qualitatively similar data is observed for SAXS from PMAVME:$C_{12}E_9$ complexes at lower

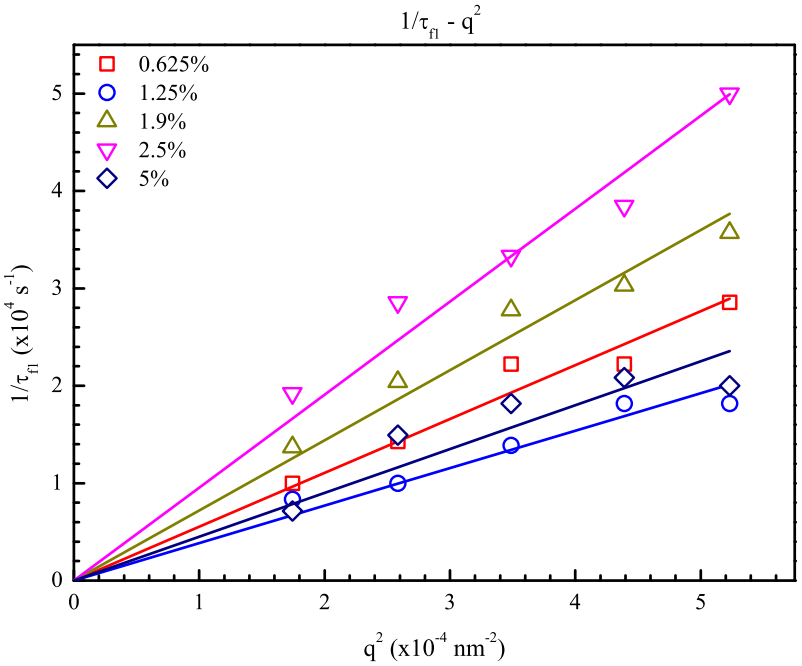

Figure 5.8: The dependence of fast relaxation time with q^2 is plotted as ($1/\tau_{f1}$ v/s q^2). Here τ_{f1} obtained from CONTIN analysis is taken.

concentrations (Figure 5.10b). We fit the SAXS data in Figure 5.10b to a power law at low q, a Lorentzian for the broad peak at intermediate q and a Gaussian for the high q peak. Parameters from the fit are tabulated in Table 5.2. We observe that there is only a modest concentration-dependent variation in the power law exponent at low q ($p \approx 2.5 - 2.6$). For concentrations 1.25% and 2.5%, there is no significant change in the positions and amplitudes of the Lorentzian and Gaussian peaks and a modest decrease

Conc. (wt%)	Power Law	Lorentz			Gaussian		
	p	X_c	w	A	X_c	w	A
1.25	2.49	0.032	0.0398	0.0013	0.11	0.14	0.10
2.5	2.60	0.032	0.0373	0.0013	0.11	0.13	0.10
5	2.61	0.029	0.025	0.0014	0.11	0.08	0.10

Table 5.2: Table showing the fit values of the SAXS data with the power law, Lorentz function and Gaussian peak. The parameter p is the power law exponent, X_c is the centroid of the distribution and A is the amplitude of the distribution.

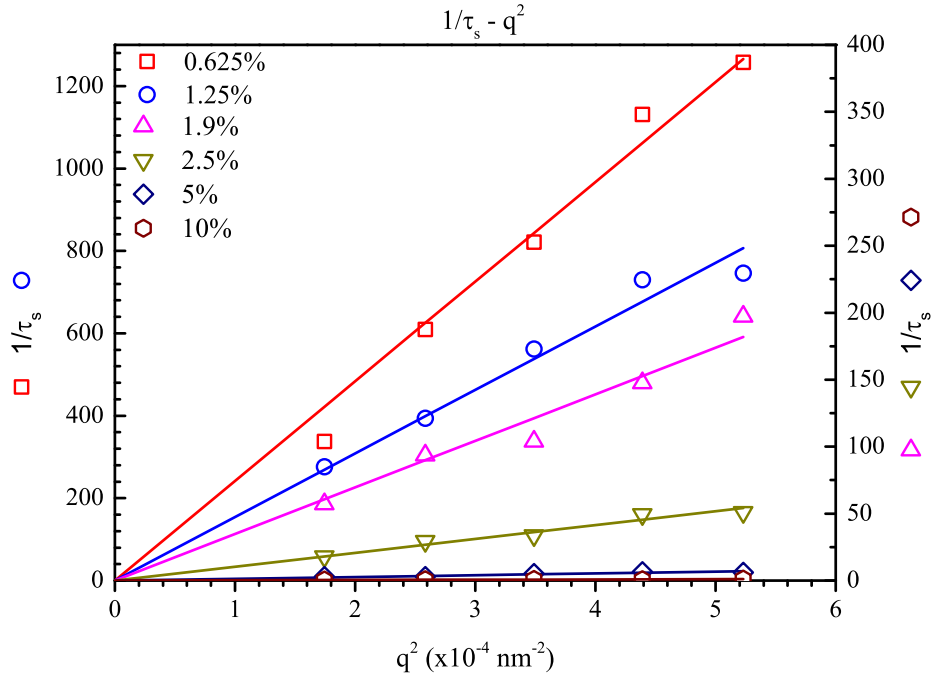

Figure 5.9: The dependence of slow relaxation time with q^2 is plotted as ($1/\tau_s$ v/s q^2). Here τ_s obtained from CONTIN analysis is taken.

in peak widths. However, for the 5% dispersion of the complex, the Lorentzian peak shifts to lower q and there is a significant decrease in the widths of the Lorentzian and Gaussian peaks.

5.4 Discussion

Our results suggest the following model for the concentration dependent solution structure of the 1 : 1 PMAVME:$C_{12}E_9$ complex. PMAVME is hydrophobic and, while it disperses in water, it does not form a molecular solution. Rather, it forms large aggregates, as can be observed in the cryo-TEM. These aggregates are comprised of hydrophobic domains with a correlation length of ∼O(10nm)(from the SAXS correlation peak for PMAVME). Complexation with nonionic surfactant $C_{12}E_9$ results in the formation of

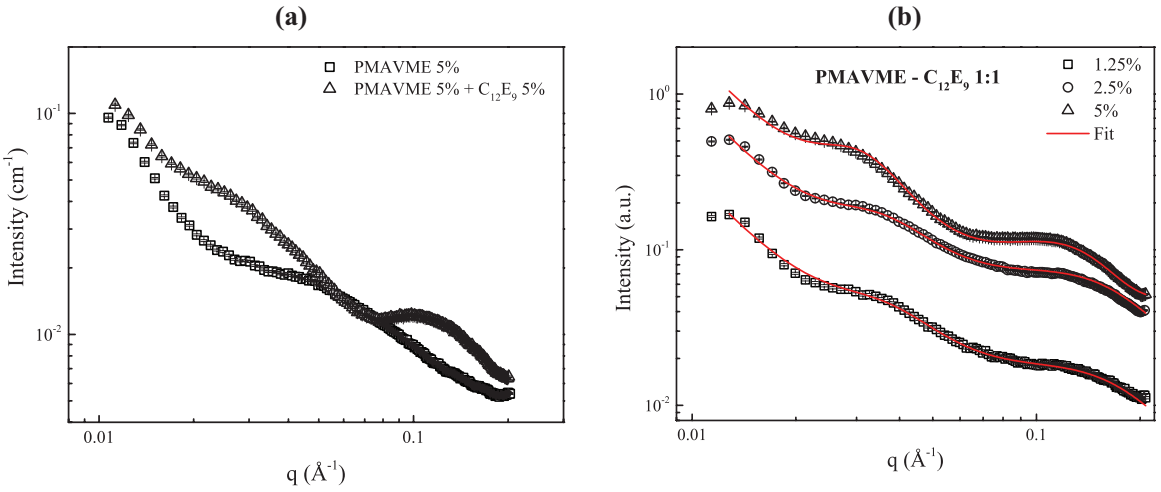

Figure 5.10: Comparison of the SAXS plots for (a) the 5% neat PMAVME solution (PMAVME 5%) and PMAVME–$C_{12}E_9$ 5% solution and (b) PMAVME-$C_{12}E_9$ solutions for different concentrations.

micellar structures that are significantly smaller and that scatter less than the PMAVME aggregates. Thus, there is a decrease in the turbidity of the dispersion when PMAVME complexes with $C_{12}E_9$. Surfactant micelles are known to associate with the hydrophobic backbone of maleic acid-vinyl alkyl ether copolymers.[22–24,31] This association screens the hydrophobic backbone from water and allows PMAVME chains to expand in solution.

Cryo-TEM of the complexes indicates the formation of structures characterized by a length scale of ∼O(10nm). We note that the SAXS is characterized by two peaks at $q = 0.032\text{Å}^{-1}$ and 0.11Å^{-1} (Table 5.2), that correspond to correlation lengths of ($= 2\pi/q$) 20nm and 6nm respectively. We also note that we can extract a concentration-dependent diffusion constant from the slope of the $\tau_f^{-1} - q^2$ data from the DLS. The diffusion constant decreases with increasing concentration. Extrapolation to zero concentration yields a diffusivity of $4.16 \times 10^{-11}\text{m}^2/\text{s}$. This corresponds to translational diffusion of an entity with a length scale of 6.2nm ($k_BT/6\pi\eta D$). Thus, real space cryo-TEM imaging, SAXS and DLS data indicate that complexation of the PMAVME with $C_{12}E_9$ results in the formation of ∼O(10nm) micellar structures. Breakup of hydrophobic PMAVME aggregates due to complexation and micelle formation is associated with a reduction in

the specific viscosity of the dispersion.

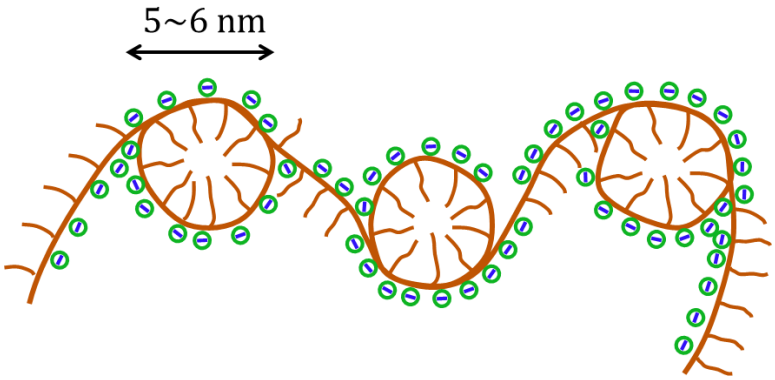

Figure 5.11: Schematic cartoon representing the microstructure of the complex. Here, the micelles are adsorbed on the polymer backbone.

The organization of these micellar complexes at larger length scales result in an increase in SAXS intensity at low q (Figure 5.10b). For concentrations up to 2.5%, the intensity of visible laser light scattered by dispersions of the complex show only a weak q dependence ($I \sim q^{-0.5}$, Figure 5.4). Thus, it appears that the micellar structures are homogeneously distributed in the sample, at length scales larger than 100nm. We do not understand the origin of the $q^{-0.5}$ dependence of the scattered intensity. With increase in concentration of the complex, there is an increase in the specific viscosity ($\sim c^{0.5}$) of the dispersion, reminiscent of Fuoss' law for semidilute unentangled polyelectrolyte solutions with no added salt. For concentrations above 2.5%, there is a much more rapid increase in the specific viscosity. At these concentrations, the DLS fast relaxation can no longer be modelled as a monomodal distribution. Further, at a concentration of 5%, there is a qualitative change in the q-dependence of scattered visible laser light ($I \sim q^{-2}$). While the scattered visible laser light intensity at lower concentrations collapses when scaled with the dispersion concentration, we note that 5% data does not. Rather, it shows a higher forward scattering and a lower scattering at high q, suggesting the formation of large structures, compared to the wavelength of scattered light. We believe that the change in behaviour with concentration correlates with the onset of a liquid–liquid phase

separation at concentrations between 2.5% and 5%. The q-dependent scattered visible light can be fitted using an Ornstein-Zernicke form as follows:

$$I(q) \sim \frac{1}{a_1 + a_2 q^2} \tag{5.9}$$

From this, we obtain a length scale that characterizes the density fluctuations as $\xi = \sqrt{a_2/a_1} = 744\text{nm}$ (Figure 5.12). This is consistent with the strong scattering in the forward direction observed for the 5% sample.

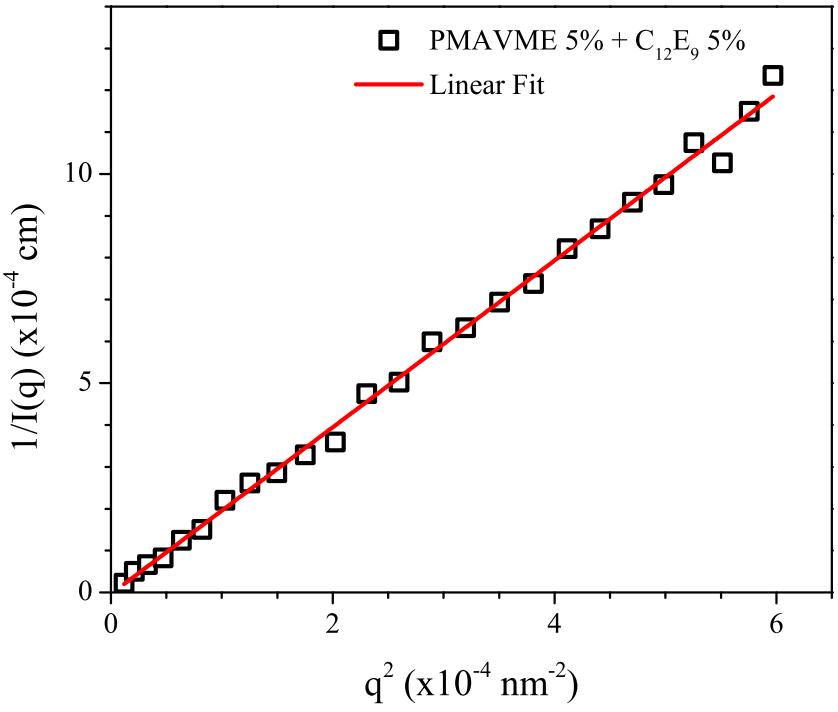

Figure 5.12: Ornstein-Zernike plot for 5% PMAVME–$C_{12}E_9$ dispersion.

We now examine the concentration-dependent DLS data from the dispersions of the complex. At low concentrations, up to 1.25%, the DLS data is fitted well using a bimodal distribution of relaxation times. The fast relaxation time does not vary strongly with concentration (Figure 5.13) and, we have shown, that it corresponds to a length scale of

6.2nm. Therefore, we associate this with the diffusion of the micellar aggregate formed due to surfactant complexation along the PMAVME chain. The slow mode is associated with cooperative diffusion of the complexes. We note that, at these concentrations, the specific viscosity $\sim c^{0.5}$ and has a value near 1. Thus, we anticipate that the dispersion is in the semidilute unentangled state. It is possible that the slow mode is associated with concentration fluctuations in the semidilute state. With increase in concentration, we observe that a monomodal fast relaxation is insufficient to fit the DLS data. The CONTIN analysis suggests that two fast modes and a slow mode are necessary to fit the 1.9% and 2.5% data and that three fast modes are required at higher concentrations. The specific viscosity also increases rapidly above a concentration of 2.5%. We believe that these modes correlate with the onset of a liquid–liquid phase separation, such that, at 5%, the static light scattering clearly indicates the formation of large concentration fluctuations, characterized by a length scale of 744nm. At all concentrations, the slow mode represent the dominant relaxation. The time scale corresponding to the slow mode increases dramatically and increases by over three orders of magnitude from 0.625% to 10%. At low concentrations, we associate the slow mode with semidiute concentration fluctuations. However, at concentrations of 5% and 10%, it is possible that the slow mode corresponds to relaxation processes at the length scale of the phase-separated domains. We note that the slow mode becomes increasingly dominant as the mode of relaxation with increase in concentration.

In contrast to the DLS, there is no significant change in the peak positions from SAXS as concentration increases from 1.25% to 2.5% to 5%. There is an increase in the scattered intensity with concentration but no qualitative change in the shape of scattered intensity. This suggests that the local structure of the complex, with ∼O(10nm) micellar structures formed by association of the surfactants with PMAVME backbone does not change with concentration. Even at concentration of 5%, where there is liquid–liquid phase separation,

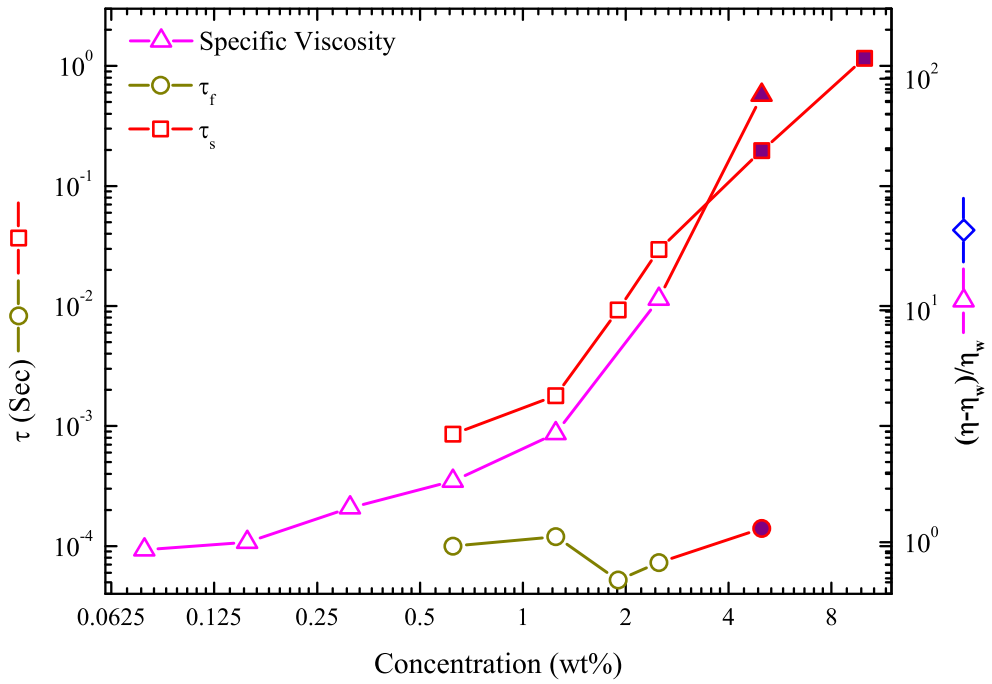

Figure 5.13: Viscosity and relaxation times as a function of concentration. The purple colour points show the region of phase separation.

it appears that the local structure of the micellar aggregates is preserved.

5.5 Conclusions

We use specific viscosity measurements, static and dynamic visible laser light scattering and SAXS to explore the concentration-dependent change in structure of dispersions containing a hydrophobic polyelectrolyte, PMAVME, and nonionic surfactant $C_{12}E_9$. The PMAVME aggregates in water to form a turbid dispersion, but clears up on addition of the nonionic surfactant. The surfactant associates with the PMAVME to form a complex that gives a relatively clear dispersion. The complex forms a semidilute, unentangled dispersion at concentrations below 2.5%. Association of the surfactant with the PMAVME

gives rise to ∼O(10nm) surfactant micellar structures along the backbone. The diffusion constant associated with these structures decreases with concentration, suggesting an attractive inter-aggregate interaction. This attractive interaction drives a liquid–liquid phase separation at concentrations above 5%.

References

[1] Svensson, A. V.; Huang, L.; Johnson, E. S.; Nylander, T.; Piculell, L. *ACS Appl. Mater. Interfaces* **2009**, *1*, 2431–42.

[2] Svensson, A. V.; Johnson, E. S.; Nylander, T.; Piculell, L. *ACS Appl. Mater. Interfaces* **2010**, *2*, 143–156.

[3] dos Santos, S.; Gustavsson, C.; Gudmundsson, C.; Linse, P.; Piculell, L. *Langmuir* **2011**, *27*, 592–603.

[4] Bai, G.; Catita, A. M.; Nichifor, M.; Bastos, M. *J. Phys. Chem. B* **2007**, *111*, 11453–11462.

[5] Basilio, N.; Gómez, B.; Garcia-Rio, L.; Francisco, V. *Chem. - A Eur. J.* **2013**, *19*, 4570–6.

[6] Clauzel, M.; Johnson, E. S.; Nylander, T.; Panandiker, R. K.; Sivik, M. R.; Piculell, L. *ACS Appl. Mater. Interfaces* **2011**, *3*, 2451–62.

[7] Philippova, O.; Hourdet, D.; Audebert, R.; R.Khokhlov, A. *Macromolecules* **1996**, *29*, 2822–2830.

[8] Sukhorukov, G. G. B.; Donath, E.; Lichtenfeld, H.; Knippel, E.; Knippel, M.; Budde, A.; Möhwald, H. *Colloids Surfaces A* **1998**, *137*, 253–266.

[9] Muthukumar, M. *J. Chem. Phys.* **1987**, *86*, 7230.

[10] Rühe, J. et al. *Adv. Polym. Sci.* **2004**, *165*, 189–198.

[11] Angelescu, D. G.; Nylander, T.; Piculell, L.; Linse, P.; Lindman, B.; Tropsch, J.; Detering, J. *Langmuir* **2011**, *27*, 9961–71.

[12] Blinkhorn, A.; Bartold, P.; Cullinan, M.; Madden, T.; Marshall, R.; Raphael, S.; Seymour, G. *British dental journal* **2009**, *207*, 117–125.

[13] Cummins, D. *Journal of clinical periodontology* **1991**, *18*, 455–461.

[14] Binana-Limbele, W.; Zana, R. *Macromolecules* **1987**, *20*, 1331–1335.

[15] Binana-Limbele, W.; Zana, R. *Macromolecules* **1990**, *23*, 2731–2739.

[16] Benrraou, M.; Zana, R.; Varoqui, R.; Pefferkorn, E. *J. Phys. Chem.* **1992**, *96*, 1468–1475.

[17] Anthony, O.; Zana, R.; Anthony, O. *Macromolecules* **1994**, *27*, 3885–3891.

[18] Zdanowicz, V. S.; Strauss, U. P. *Macromolecules* **1993**, *26*, 4770–4773.

[19] Dobrynin, A. V.; Rubinstein, M. *Macromolecules* **2001**, *34*, 1964–1972.

[20] Kumaraswamy, G.; Venugopal, E. Surfactant-copolymer complexes useful for sustained drug release. Application US20150174251 A1, 2014.

[21] English, R. J.; Laurer, J. H.; Spontak, R. J.; Khan, S. a. *Ind. Eng. Chem. Res.* **2002**, *41*, 6425–6435.

[22] Deo, P.; Jockusch, S.; Ottaviani, M. F.; Moscatelli, A.; Turro, N. J.; Somasundaran, P. *Langmuir* **2003**, 10747–10752.

[23] Deo, P.; Deo, N.; Somasundaran, P. *Langmuir* **2005**, 9998–10003.

[24] Deo, P.; Somasundaram, P. *Langmuir* **2005**, *21*, 3950–3956.

[25] Deo, P.; Deo, N.; Somasundaran, P. *Langmuir* **2007**, 5906–5913.

[26] Santos, O.; Johnson, E. S.; Nylander, T.; Panandiker, R. K.; Sivik, M. R.; Piculell, L. *Langmuir* **2010**, *26*, 9357–9367.

[27] Bromberg, L.; Temchenko, M.; Colby, R. H. *Langmuir* **2000**, *16*, 2609–2614.

[28] Guillemet, F.; Piculell, L. *J. Phys. Chem.* **1995**, *99*, 9201–9209.

[29] Jain, N.; Trabelsi, S.; Guillot, S.; McLoughlin, D.; Langevin, D.; Letellier, P.; Turmine, M. *Langmuir* **2004**, *20*, 8496–8503.

[30] Mohr, A.; Nylander, T.; Piculell, L.; Lindman, B.; Boyko, V.; Bartels, F. W.; Liu, Y.; Kurkal-Siebert, V. *ACS Appl. Mater. Interfaces* **2012**, *4*, 1500–11.

[31] Magny, B.; Iliopoulos, I.; Zana, R.; Audebert, R. *Langmuir* **1994**, *10*, 3180–3187.

[32] Iliopoulos, I. *Curr. Opin. Colloid Interface Sci.* **1998**, *3*, 493–498.

[33] Hansson, P. *Langmuir* **2001**, *17*, 4167–4180.

[34] Piculell, L.; Guillemet, F.; Thuresson, K.; Shubin, V.; Ericsson, O. *Adv. Colloid Interface Sci.* **1996**, *63*, 1–21.

[35] Li, Y. J.; Xia, J. L.; Dubin, P. L. *Macromolelcules* **1994**, *27*, 7049–7055.

[36] Berne, B. J.; Pecora, R. *Dynamic light scattering: with applications to chemistry, biology, and physics*; Courier Corporation, 2000.

Chapter 6

Conclusion and Future Work

Contents

The thesis focuses the structure of assemblies of nonionic surfactants with colloids and polyelectrolytes. We have explored the following model systems: (a) The effect of colloids on the liquid crystalline mesophase formed by the monoglyceride-water system. (b) Preparation of multifunctional polyelectrolyte-coated submicron sized cubic phase particles from the monoglyceride-water system. (c) Influence of nanoparticle size on their incorporation within a nonionic surfactant lamellar phase. (d) The structure and dynamics of polyelectrolyte-nonionic surfactant complexes in aqueous solution. The main results are summarized below.

At high concentration, colloidal silica nanoparticles are found to macrophase separate in the bicontinuous cubic phases of $Ia3d$ and $Pn3m$ symmetries, as indicated by the monotonous decrease in the lattice parameter with nanoparticle concentration. The decrease in the lattice parameter is interpreted as arising from the formation of hydrophilic nanoparticle clusters, that macrophase separate and dehydrate the mesophase by associating with the bound water in the bicontinuous water channels. Qualitatively different behaviour was observed in the case of nanoparticle loaded hexagonal and lamellar phases. Here, the lattice parameter increased up to a critical threshold concentration of nanoparticles, after which it decreased sharply upon nanoparticle addition. The order disorder transition temperature of the lamellar phase increases with nanoparticle addition and then rapidly decreases above a threshold concentration. We demonstrate that once the nanoparticles macrophase separate, water migrates from the lamellar layers to the nanoparticle clusters, thus dehydrating the lamellar mesophase. Our experimental results suggest a specific interaction mechanism of the nanoparticles with the membrane in the low concentration regime. Our findings provide evidence for the complex phase behavior of lyotropic mesophase/nanoparticle systems and provide insights into the role of mesophase symmetry on the partitioning and phase separation of the guest colloidal species.

Cubosomes, which are cubic phase lipid particles with $Pn3m$ symmetry, can be simultaneously loaded with hydrophobic and hydrophilic compounds. Cubosomes are found to retain their internal structure even after the simultaneous loading of Naproxen Sodium salt and Nile Red dye. We demonstrate that a single layer coating of a bio-compatible polyelectrolyte, poly-ϵ-lysine, imparts multi-functionality to the cubosomes. Coated cubosomes form dispersions that are stable in the presence of BSA. The multi-functional cubosomes are readily absorbed on a substrate and can be spatially localized to regions bearing opposite charge to that of the cubosome.

We observe particle size dependent aggregation phenomena with doping of silica nanoparticles in a $C_{12}E_4$/water lamellar mesophase. Nanoparticles larger than about 15nm in size are excluded from the lamellar phase, and form large aggregates. This aggregation behavior is reversible and the nanoparticles redisperse above the lamellar phase T_{ODT}. However, particles smaller than about 11nm in size aggregate irreversibly, and stay aggregated both above and below the T_{ODT}. We demonstrate that this is a consequence of the nanoparticle size dependence of nanoparticle/$C_{12}E_4$ bilayer interactions. Contrast matched SANS experiments proved that an adsorbed surfactant bilayer forms on nanoparticles larger than about 15nm but not on 11nm particles or smaller, and argue that the the bending penalty for bilayers does not allow coating of particles smaller than about 11nm. Therefore, particles smaller than 11nm aggregate irreversibly, and larger (bilayer coated) particles aggregate only when they are excluded from the L_α phase, but are dispersed above T_{ODT}. While we report data only for $C_{12}E_4$/water/silica nanoparticle systems, we believe that our results might be more generally applicable to the interactions of relatively hydrophobic surfactants with attractive nanoparticles. If so, these results will have important implications for researchers who are investigating the structuring of nanoparticle assemblies in mesophases, as well as for those who design nanoparticle based drug delivery systems that interact with bilayer cell walls.

The structure of hydrophobic polyelectrolyte copolymer in solution changes upon the introduction of nonionic surfactant. Hydrophobic polyelectrolyte aggregates break up due to the formation of micellar complexes with the surfactant. We report the structure of the complexes at multiple length scales. The complexes also demonstrate a hierarchy of relaxations, including a fast relaxation associated with diffusion of the micellar structures and slow relaxations that correspond to semidiute concentration fluctuations at low concentrations and to spatially persistent large length scale fluctuations at higher concentrations. We demonstrate that the complexes undergo a liquid–liquid phase separation at high concentrations.

The thesis presented an overview of multi-component systems consisting of surfactant, colloids and polymers which are commonly used in food, personal care and pharmaceutical applications. The main objective of this thesis was the effect of guest components on the phase behaviour of the ternary systems. We have demonstrated that ternary systems can be tuned to introduce desirable properties simply by addition of suitable guest components. These findings have implications in industrial formulations where one need not want to use complex chemical modifications.

Future Work

Our work suggest few open questions, a few of which are summarized here.

Effect of colloidal surface properties on self-assembly

The phase separation of guest colloidal particles in the surfactant mesophase opens up questions regarding the influence on particle surface properties on the structure formation in the mesophase. Our work and most of the literature focuses on commercially available hydrophilic silica nanoparticles. The surface of these silica particles can be modified

by electrostatic adsorption of polyelectrolytes. A detailed investigation of the effect of the surface properties on the phase behaviour of colloids has relevance for industrial applications in food and cosmetic industry, where the stability of colloidal formulations in the presence of surfactants is important.

Effect of shear on surfactant-colloid structures

It is known that oily streak networks formed by the cholesteric liquid crystals are stabilized by dispersions of micron sized colloidal particles doped in the system.[1] Similarly, oily streak defect networks have been shownBasappa et al.[2] to be stabilized against oscillatory shear by micron sized particulate inclusions. Thus, inclusion of nanoparticles have implications for the rheology of surfactant mesophases. Though reports on the shear rheology of lyotropic lamellar phase exist, a little is known about the effect of guest nanoparticle inclusions on the lyotropic lamellar phase under the application of oscillatory shear.

Targeting and delivery of hydrophobic compounds

Hydrophobically modified polyelectrolytes are known to form a pearl-necklace structure in poor solvents. Pearl structure in these aggregates are used as pockets for loading flavoured hydrophobic compounds in many health care applications.[3] One of the issue found in this formulation is the stainability of the flavour compound in presence of charged surfactants which are used in the health care products. We have proposed a refined mechanism recently where a better stability is observed.[4] A detailed investigation on the structure and dynamics of this formulation is highly desirable both as application and fundamental point of view.

References

[1] Zapotocky, M.; Ramos, L.; Poulin, P.; Lubensky, T. C.; Weitz, D. A. *Science* **1999**, *283*, 209–212.

[2] Basappa, G.; Kumaran, V.; Nott, P. R.; Ramaswamy, S.; Naik, V. M.; Rout, D. *Eur. Phys. J. E* **1999**, *12*, 269–276.

[3] Nabi, N.; Gaffar, A. Antibacterial Antiplaque Oral Composition. 1990.

[4] Kumaraswamy, G.; Venugopal, E. Surfactant-copolymer complexes useful for sustained drug release. 2014.

This page is intentionally left blank

List of Research Credentials, Awards and Conferences

Publications and Patents

1. **E. Venugopal**, S. K. Bhat, J. J. Vallooran, and R. Mezzenga, "Phase Behavior of LipidBased Lyotropic Liquid Crystals in Presence of Colloidal Nanoparticles", ***Langmuir***, vol. 27, pp. 9792–9800, 2011.

2. S. S. Patil, **E. Venugopal**, S. Bhat, K. R. Mahadik, and A. R. Paradkar, "Probing influence of mesophasic transformation on performance of self-emulsifying system: effect of ion", ***Mol. Pharm.***, vol. 9, no. 2, pp. 318-24, Feb. 2012.

3. S. S. Patil, **E. Venugopal**, S. Bhat, K. R. Mahadik, and A. R. Paradkar, "Microstructural elucidation of self-emulsifying system: effect of chemical structure", ***Pharm. Res.***, vol. 29, no. 8, pp. 2180-8, Aug. 2012.

4. **E. Venugopal**, V. K. Aswal, and G. Kumaraswamy, "Nanoparticle Size Controls Aggregation in Lamellar Nonionic Surfactant Mesophase", ***Langmuir***, vol. 29, no. 31, pp. 9643-9650, 2013.

5. S. Deshpande, **E. Venugopal**, S. Ramagiri, J. R. Bellare, G. Kumaraswamy, and N. Singh, "Enhancing Cubosome Functionality by Coating with a Single Layer of Poly-ϵ-lysine," ***Appl. Mater. Interfaces***, vol. 6, no. September, pp. 17126–17133, 2014.

6. G. Kumaraswamy and **E. Venugopal**, "Surfactant-copolymer complexes useful for sustained drug release", **Patent** US20150174251 A1, 2014.

7. S. S. Patil, **E. Venugopal**, S. Bhat, K. R. Mahadik, and A. R. Paradkar,"Mapping ion-induced mesophasic transformation in lyotropic in situ gelling system and its

correlation with pharmaceutical performance", ***Pharm. Res.***,vol. 30, pp. 1906–1914, 2013

8. **E. Venugopal**, Judith, Ishi Talmon, S. K. Bhat and G. Kumaraswamy,"Structure and Dynamics of Concentrated Polyelectrolyte Solutions in Presence of Nonionic Surfactants", (Manuscript in preparation for ***Macromolecules***)

Awards

1. Awarded prestigious **Indo-Swiss Joint Research Programme 2010** for 4 months by the Swiss embassy (India) to visit and work at ETH Zürich, Zürich, Switzerland.

2. Awarded **Junior Research Fellowship (JRF)** by Council of Scientific and Industrial Research (CSIR) for pursuing Ph.D.

Conferences

1. Attended the conference "CochinNANO" organized by CUSAT Cochin, India from 17^{th} June 2008 to 20^{th} June 2008.

2. Attended "Conference on Neutron Scattering and Mesoscopic Systems" from 12^{th}October 2009 to 14^{th} October 2009 at Goa University.

3. Attended the conference on "Nanotechnology and Advanced Function Materials" organized by NCL Pune, India from 9^{th} July 2009 to 11^{th} July 2009.

4. Attended the School and Symposium on "Rheology of Complex Fluids" organized in IIT Madras, India from 4^{th} January 2010 to 9^{th} January 2010. Work presented in the form a poster.